Contract No. DTFACT-15-D-00007
Delivery Order 005 NAPTF Support
Deliverable 4.9.2.4
Construction Cycle 8 Phase II Overlay Testing Report

July 2018

Submitted on July 12, 2018

Prepared by Carlos Cary, Ph.D., Mesbah Ahmed, Ph.D. and Hao Yin, Ph.D. P.E.
Gemini Technologies, Inc.

Submitted by General Dynamics Information Technology

GENERAL DYNAMICS
Information Technology

TABLE OF CONTENTS

LIST OF FIGURES

LIST OF TABLES

LIST OF ACRONYMS

AC	Advisory Circular
ACN-PCN	Aircraft Classification Number–Pavement Classification Number
CC4	Construction Cycle 4
CC8	Construction Cycle 8
DAQ	Data Acquisition Unit
ECS	Eddy Current Sensors
EG	Strain Gages
FAA	Federal Aviation Administration
ICAO	International Civil Aviation Organization
IPRF	Innovative Pavement Research Foundation
NAPTF	National Airport Pavement Test Facility
NAPTV	National Airport Pavement Test Vehicle
PCI	Pavement Condition Index
POT	Potentiometers
PSPA	Portable Seismic Properties Analyzer
SCI	Structural Condition Index
SOP	Standard Operating Procedure
SPU	Signal Processing Unit

1. INTRODUCTION

1.1 RESEARCH NEED

A research initiative aimed at improving the existing unbonded rigid overlay design methodology was launched in 2001 as a joint effort between the Innovative Pavement Research Foundation (IPRF) and the Federal Aviation Administration (FAA). During the first stage of this IPRF-FAA initiative, an experimental plan for a series of full-scale traffic test at the National Airport Test Facility (NAPTF) was developed by Khazanovich (*1*). Quality Engineering Solutions (QES) was contracted by the IPRF to execute the first two tests of the series during Construction Cycle 4 (CC4), between 2005 and 2010 (*2,3*). Among other design parameters, particular focus was given to the effect that the underlying pavement condition has on the overlay life. For the first CC4 full-scale overlay test called "Baseline Experiment," the underlying pavement consisted of intact slabs whereas for the second overlay test, called "Structural Condition Index (SCI) Validation," the overlay was built over the distressed underlying "baseline pavement." Upon completion of CC4, the combined full-scale traffic datasets produced valuable information on overlay performance for underlying SCI ranges of 20 to 50, and 80 to 100.

1.2 OBJECTIVE

Because the CC4 unbonded rigid overlay tests included only relatively new and highly deteriorated underlying conditions, complementary full-scale traffic test was deemed necessary as part of Construction Cycle 8 (CC8). A target SCI of 80 was considered to represent the condition of a pavement that would be a realistic candidate for overlay. This specified SCI target intends to fill in significant gaps in the performance data from the previous CC4 experiment.

1.3 BACKGROUND

Rigid concrete overlays have been successfully used in the past few decades for the rehabilitation of airfield pavements. Unbonded rigid overlays are a good rehabilitation alternative even when the underlying pavement is moderately to significantly damaged. Placement of an overlay does not require removal of the existing pavement which makes of it a more cost-effective alternative than full reconstruction. Even when damaged, the contribution of the existing pavement to the overall load-carrying capacity is taken into account for the overlay design (*4*). Unbonded rigid overlays can restore the structural capacity and correct the ride quality of existing pavements and therefore extend the pavement life.

The original overlay design method developed by the U.S. Army Corp of Engineers, which was purely empirical in nature, was used for many decades. In the late 80s, Rollings proposed a mechanistically based design procedure (*5*). As a modification to the Pavement Condition Index (PCI), Rollings introduced the Structural Condition Index (SCI) which considers only those distress types associated to pavement fatigue damage. Rollings formulated the progressive change in effective stiffness of underlying pavements, in terms of the deterioration captured by changes in the SCI. Since then, the SCI method for describing the pavement performance

became a fundamental component in the subsequent development of overlay design procedures. The mechanistic approach proposed by Rollings served as foundation for the development of the current FAA advanced design procedure for new rigid pavements and rigid overlays of existing concrete pavements (*6*).

Under the sponsorship of the IPRF, research initiatives aimed at improving currently available design methodologies for concrete overlays were undertaken. Recognizing that the performance correlations in past FAA design methods were based on accelerated traffic tests conducted in the 1940s and 1950s, a need for updated modeling data that capture the demands and characteristics of modern concrete pavements was identified. The development of an experimental plan by Khazanovich for full-scale testing at the FAA NAPTF was the first effort of the IPRF research initiative (*1*). Khazanovich recommended a first round of testing at the NAPTF considering only unbonded overlays and focusing on the effect of the following factors: underlying pavement conditions, joint mismatching, joint design, subgrade type, gear geometry and traffic wander.

In 2005 the IPRF contracted QES to execute the experimental plan developed by Khazanovich. QES conducted the first two unbonded overlay experiments at the NAPTF: a) the Baseline Experiment and b) the SCI Validation Experiment. The first experiment consisted of three structural cross-sections built over a medium strength subgrade. The underlying slabs were intact (i.e.; SCI=100), with different joint matching conditions aimed at evaluating the effect of underlying discontinuities on the overlay performance. The intact condition of the base pavement offered an opportunity to assess the relative deterioration in the underlying slabs (*3*).

The damaged underlying slabs from the Baseline Experiment were later used as the base pavement for the SCI Validation Experiment. Upon the removal of baseline overlay, additional cracking was induced to the underlying slabs using the National Airport Pavement Test Vehicle (NAPTV). For two thirds of the underlying slabs, the resulting SCI values fell within a range of 20 to 50. In the remaining third, SCI values in the low 80s were obtained. Although a wide range of underlying SCI conditions were covered by the two IPRF experiments, a gap in SCI between 50 and 80 yet remained to be filled. The present report documents the findings of the latest overlay experiment that was conducted at the NAPTF considering intermediate range of underlying conditions.

2. DESIGN AND CONSTRUCTION OF THE TEST SECTION

2.1 DESCRIPTION OF TEST SECTION

The CC8 Overlay Test pavement consisted of two phases. Phase I, referred to as the Overload Test, involved the construction and instrumentation of an aggregate base and a Portland cement concrete (PCC) pavement. The Overload Test experiment was aimed at evaluating ICAO overload criteria for airfield rigid pavements. Phase II, referred to as the Unbonded Overlay Test, entailed the construction of an asphalt interlayer and a PCC overlay on top the post-Phase I test damaged pavement. The concept of conducting the two full-scale experiments in series provided a realistic way to introduce load-induced damage to the underlying pavement for the

second experiment. The CC8 Unbonded Overlay Test pavement was therefore designed to utilize the remaining distressed underlay slabs to examine the effects of intermediate damaged underlay condition (SCI 50-80) on the overlay performance.

2.2 CONSTRUCTION

The CC8 Overlay Test Pavement was 60 feet long and 60 feet wide between Stations 3+30 and 3+90 as illustrated in Figure 1. Figure 2 shows that the pavement was composed of two 9-inch thick unbonded P-501 concrete layers placed on 11-inch P-154 granular subbase that was supported on a clay subgrade with a CBR value of 7 to 8. A 1.4-inch thick asphalt layer was placed between the overlay and underlay as a bond breaker. Past NAPTF studies have shown that a stiff base for a concrete surface layer can increase curling severity, and intensify the resulting corner stresses. A 12-foot joint spacing was selected because it would be long enough to be consistent with field applications, but short enough to minimize cracking due to warping, especially with the thin slabs. For both Phase I and II Overlay Test pavements, the transverse joints were undowelled. All longitudinal joints were doweled, and all dowels were 3/4 inches in diameter.

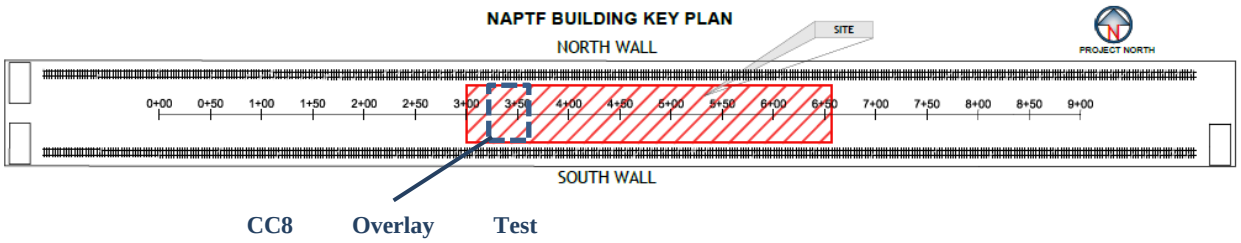

Figure 1. Overall Location Map of CC8 Overlay Test Pavement

The layout of Phase I Test pavement is shown in Figure 3. The north and south side had two lanes of five 12-foot by 12-foot slabs. The middle lane consisted of five 6-foot by 12-foot slabs that were used as transition slabs. The second phase concrete overlay, built over the damaged concrete slabs after completion of CC8 Phase I Overload Test, had a different slab configuration. Figure 4 shows the plan view of Phase II Test pavement, indicating that each test item (north and south) consisted of ten slabs distributed in two 12-foot wide lanes, with a 12-foot transition lane between test items. Therefore, transverse joints were matched, and longitudinal joints were staggered. Similar to the underlay, the transverse joints in the overlay were undowelled whereas longitudinal joints were doweled, and all dowels were 3/4 in. in diameter.

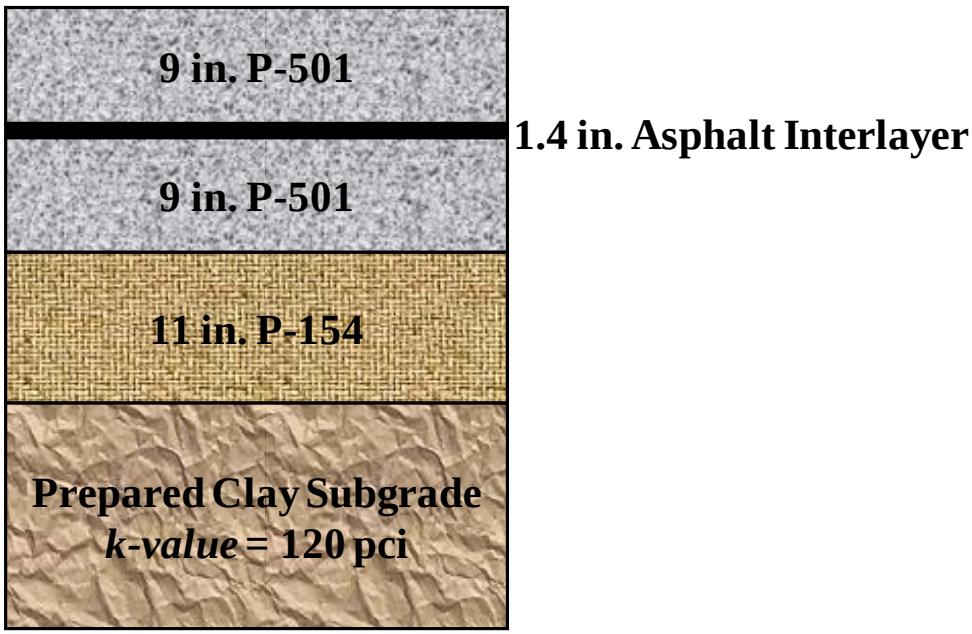

Figure 2. Pavement Cross-Section

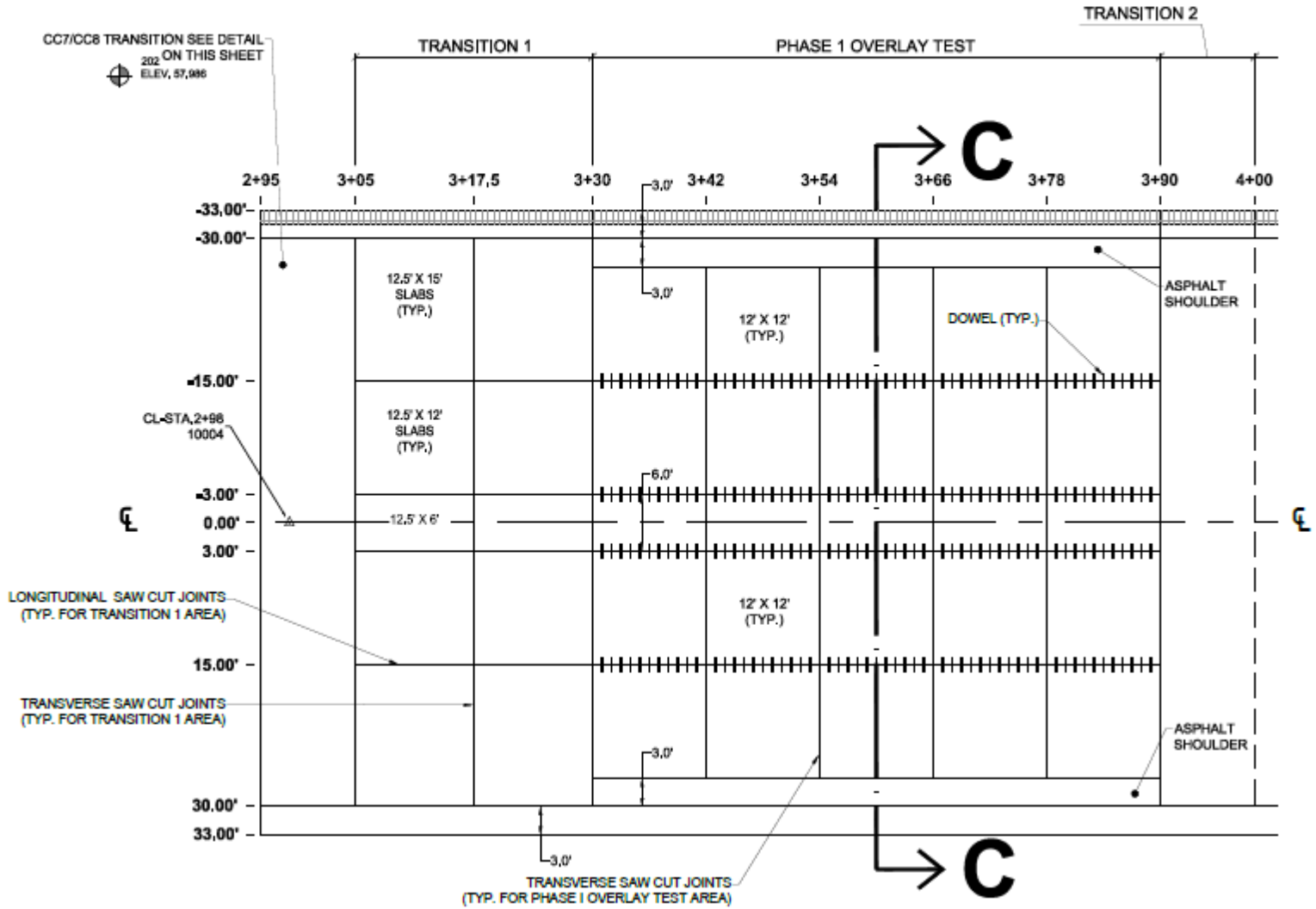

Figure 3. General Layout of CC8 Phase I - Underlay

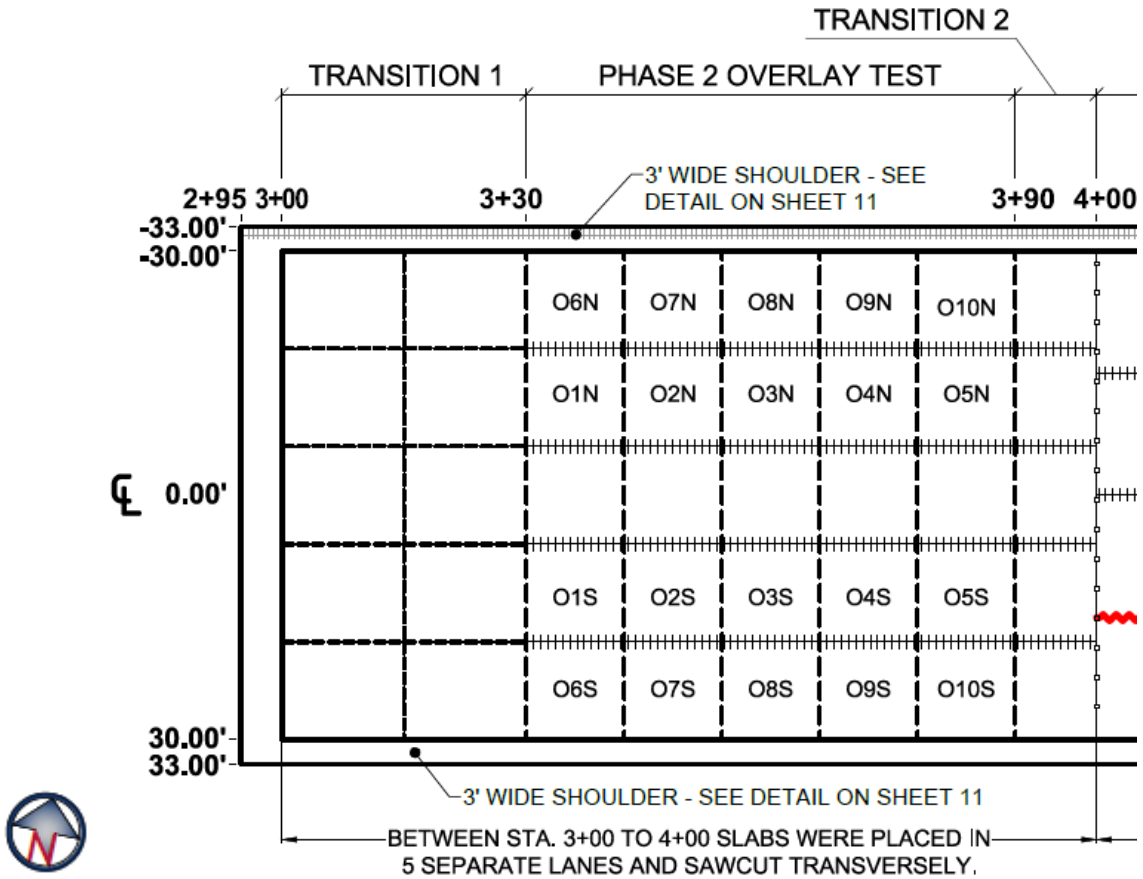

Figure 4. General Layout of CC8 Phase II - Overlay

2.2.1 SUBGRADE PREPARATION

The subgrade target California Bearing Ratio (CBR) value range was 7-8 with a tolerance of -0.5 to +0.5. Upon completion of Construction Cycle 6 pavement demolition, the subgrade was tested to see if additional removal of existing Dupont clay was necessary. The procedure used to achieve the required results included trimming to final grade, tilling to a minimum depth of 8 inches, monitoring and adjusting the moisture content until the target CBR value was achieved. The final CBR subgrade values are 7.2 and 7.4 for the north and south side, respectively. While the plate load test results for the subgrade exhibited some variation, the average k value was 110 pci on the north side, and 131 pci on the south side.

2.2.2 SUBBASE CONSTRUCTION

A P-154 granular subbase course was placed on the prepared subgrade. Moisture, gradation, and density testing were conducted on the basis of 50 square yard sublots, to control the granular material placement. The gradation samples showed the materials were within the P-154 specification limits. The average density was 97%, and the average moisture content was 7.6%. The plate load tests were performed on the top of subbase and the average k value was 216 pci on the north side, and 272 pci on the south side.

2.2.3 CONCRETE PAVING

The design target strength for the mix was 650 psi flexural strength for both the underlay and overlay. During concrete paving, beam samples were collected from the fresh concrete in the truck. For the underlay, the mean flexural strength of laboratory cured beam samples as per ASTM C78 at ages of 7 and 28 days were 487 psi and 592 psi, respectively. On average, the strength gain was 22% from 7 to 28 days. The mean flexural strength of field cured beam samples at an age of 172 days was found to be 624 psi. For the overlay, the mean flexural strength of laboratory cured beam samples at ages of 7 and 28 days were 472 psi and 557 psi, respectively. On average, the strength gain was 18% from 7 to 28 days.

The mean flexural strength of field cured beam samples at an age of 271 days was found to be 700 psi. The use of the portable seismic pavement analyzer (PSPA) provides a means of rapidly and non-destructively measuring pavement properties via ultrasonic surface waves. PSPA was used to measure the in-situ modulus of the P-501 underlay after construction. At each slab center, multiple PSPA measurements were collected at different orientations. The 28-day in-situ modulus was found to be quite consistent from one slab to another with a mean value of 4310 ksi. The average COV was 4.7 percent. The PSPA data verified the uniformity and construction quality of the underlay.

For both the underlay and overlay, the steel dowels used were 3/4 in. in diameter and 18 in. in length. They were placed at mid-depth of the concrete slabs and spaced at 12 in. in the longitudinal joints.

The surface of the concrete was given a float finish after the screed had passed the given location. Water soaked burlap strips were then placed over the surfaces of the slabs at the end of each paving day. The burlap was in turn covered with plastic sheets to retain the moisture for

curing the concrete over a 28-day period. The saw cut of transverse joints at D/3 took place approximately 24 hours after each placement. The process consisted of removing the burlap and plastic sheets, surveying the joint locations, marking the joints with string and paint, and then sawing the joints.

2.3 INSTRUMENTATION

Prior to the placement of concrete for both the underlay and overlay, instrumentation was installed in the different pavement layers at the most convenient time according to the construction schedule. The selection of gages was based on reliability, accuracy, and ease of handling at the construction site. In the underlay, the vertical movement relative to the top surface of the P-154 layer was monitored in eight slabs by potentiometers (POT) installed at the corner. To install POTs, a steel bar was first driven into the subbase to serve as a stationary reference point. Each POT was then attached to the steel bar, and a rebar chair was used to secure the height of the POT at its mid-position as the slab was constructed to make sure that both up and down movement from the as-built position could be recorded. Because the use of POTs in the underlay did not produce satisfactory data, the Eddy Current Sensor (ECS) was used in the overlay as alternative to measure the vertical movement relative to the top surface of the asphalt interlayer in eight slab corners.

In both the underlay and overlay concrete layer, two pairs of embedded strain gages (EGs) were installed in eight slabs to measure strain responses near the top and bottom of the slab. These gages were located along the longitudinal and transverse joint in the trafficked area. Embedded strain gages were installed prior to paving. Rebar chairs were used to make certain the gage center was set at the proper height, 1 in. above the bottom and 1 in. below the surface.

Thermocouple trees were installed in both the north and south side of the pavement in one slab to monitor temperature gradients. Each tree consists of three thermocouples to measure temperature at the bottom, middle, and top of the slab. The same thermocouple configuration was used in both the underlay and overlay. In addition, moisture sensors were installed at two locations to monitor changes moisture content. These sensors were driven into the subgrade at 6 inches below the surface during the subgrade preparation. Details on the specific location of the instrumentation are provided in both the plan and profile view shown in Figure 5 and Figure 6, respectively. The instrument key for both figures is included in Figure 6. The convention used to name the sensors provides information in the following order: sensor type, test item, test name, construction phase, and sequential ID. For instance; EG-N-O-II-9 stands for a Strain Gage (EG) installed in the North Test Item (N) of the Overlay Test (O), CC8 Construction Phase II (II), and sequential ID nine (9).

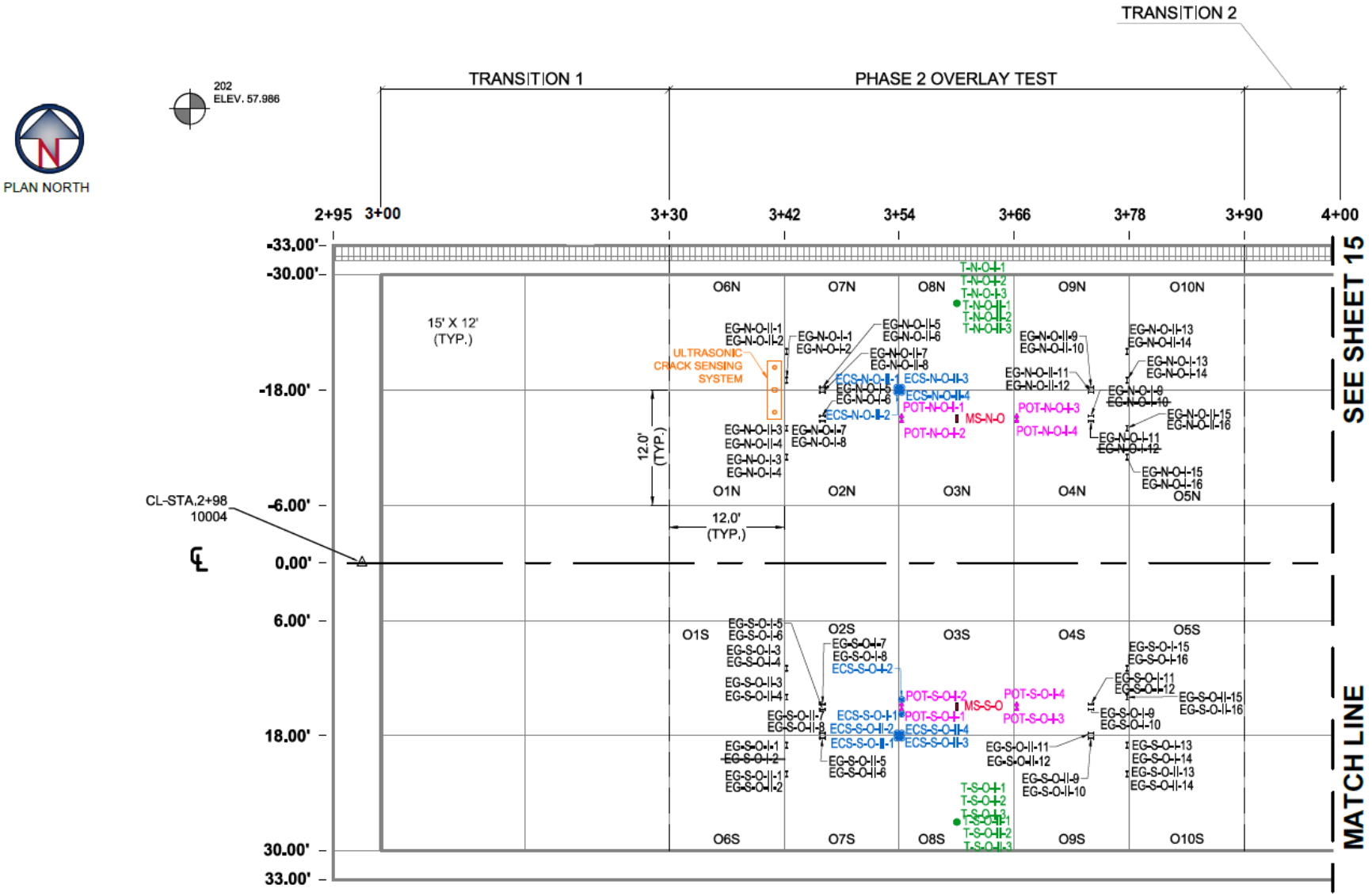

Figure 5. Instrumentation Layout, Plan View

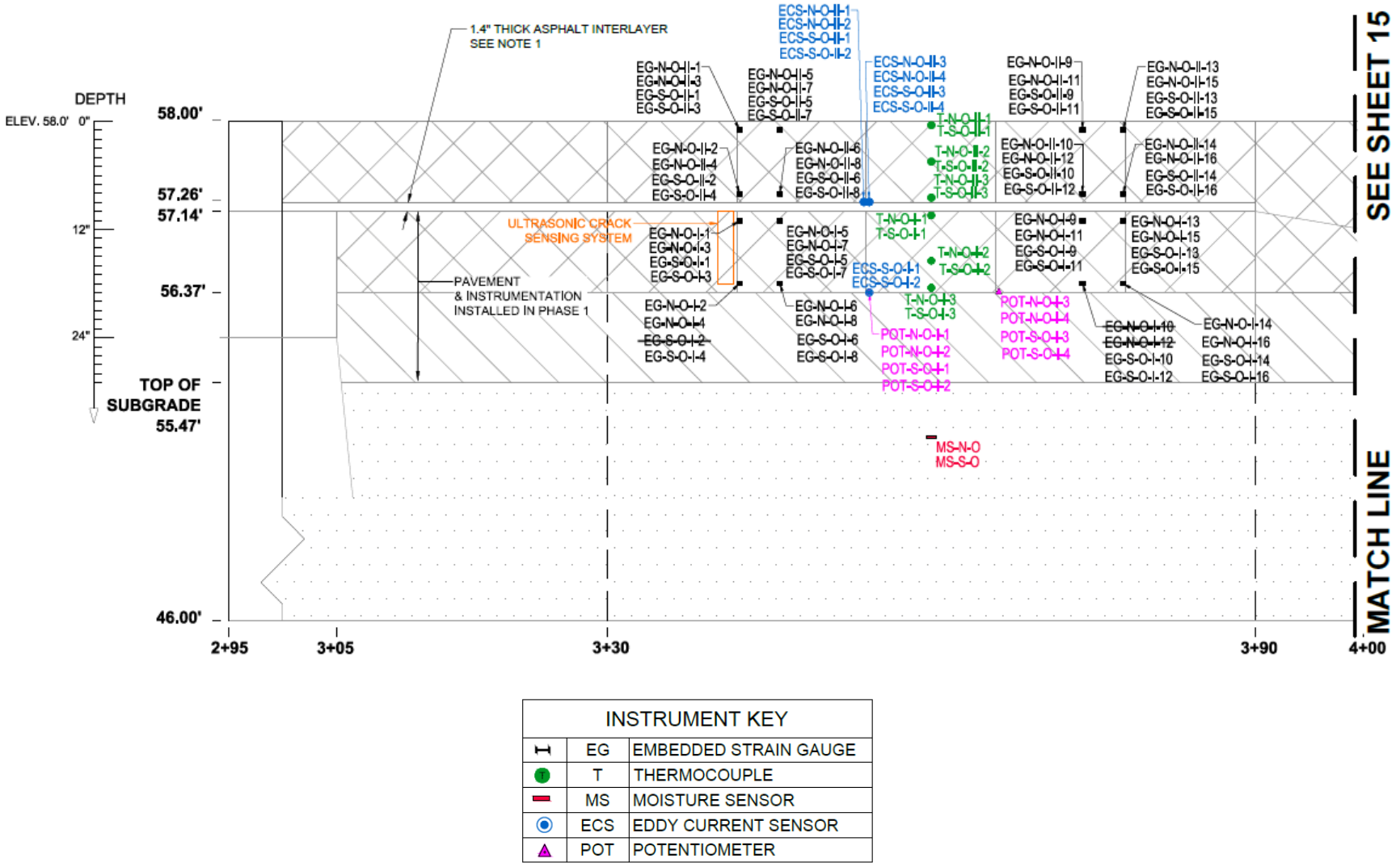

Figure 6. Instrumentation Layout, Profile View

3. DESCRIPTION OF TESTING METHODS AND EQUIPMENT

3.1 TESTING EQUIPMENT

The National Airport Pavement Test Vehicle (NAPTV) can be programmed for a controlled aircraft wander simulation and can operate in manual or fully automatic modes. In this study, the vehicle speed was limited to 2.5 mph. The test vehicle is comprised of two carriages that can accommodate up to five load modules each at a spacing of 57 inches. Each load module has two wheels at a spacing of 54 inches. This allows for configurations of up to 20 wheels with loads up to 75,000 pounds per wheel. In this study, a 6-wheel gear (3D) and a 4-wheel gear (2D) were used on the north and south carriage, respectively (Figure 7). The NAPTV simulates realistic aircraft wander by varying the lateral position of the carriages to simulate a normal distribution of aircraft traffic during traffic testing. The wander pattern used for this study consisted of 66 vehicle passes, arranged in 9 Tracks (or wander positions).

3.2 TEST DESCRIPTION

3.2.1 ESTIMATION OF INITIAL WHEEL LOAD

The north test item was loaded with the 3D gear configuration, and the south test item was loaded with the 2D gear. These gear configurations are consistent with the previous CC4 overlay experiment and are illustrated in Figure 7.

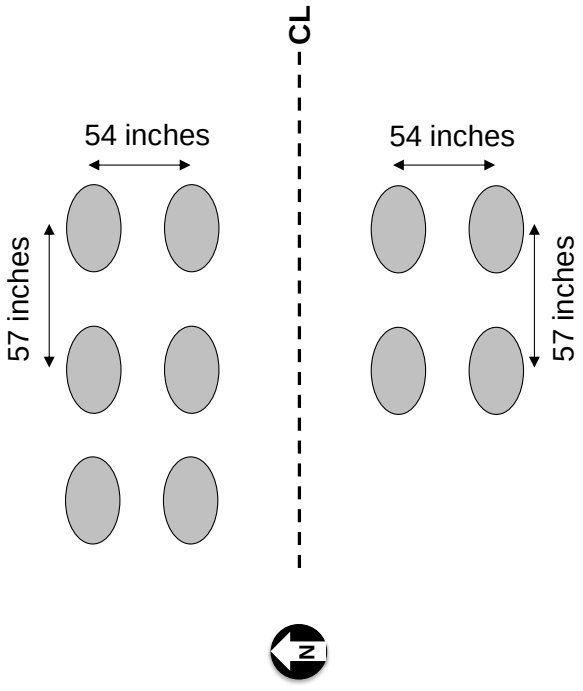

Figure 7. 3D and 2D Gear Configurations

The initial wheel load had to be carefully selected to avoid the necessity for load increases during traffic, which would complicate the analysis by introducing mixed traffic. A tire pressure of 220 psi was assumed for estimation of the wheel load. As shown in Figure 8, FAARFIELD (v. 1.42) runs were conducted using the flexural strength (R) of field cured beams: 710 psi for the overlay, and 640 psi for the underlay. The output of the analysis was passes to failure for a range of possible wheel loads.

A summary of FAARFIELD predictions at different wheel load levels is given in Tables 1 and 2 for the north and south test item, respectively. These stresses and calculated failure passes are plotted in Figure 9. When compared on the basis of the same wheel load, the 3D always resulted in slightly higher interior stresses while almost the same value of stress at the slab edge and interior was observed for the case of 2D. Given that the FAARFIELD design model makes use of conservative assumptions (fully unbonded slab-base interface, infinite subgrade depth) that may not be reflected in the built structure, Figure 9 suggests 40,000 pounds as the initial wheel load for both north and south test items for a target number of passes to failure of 5000. This initial wheel load corresponds to an approximate stress-ratio of 0.7 with respect to the 270-day field cured flexural strength.

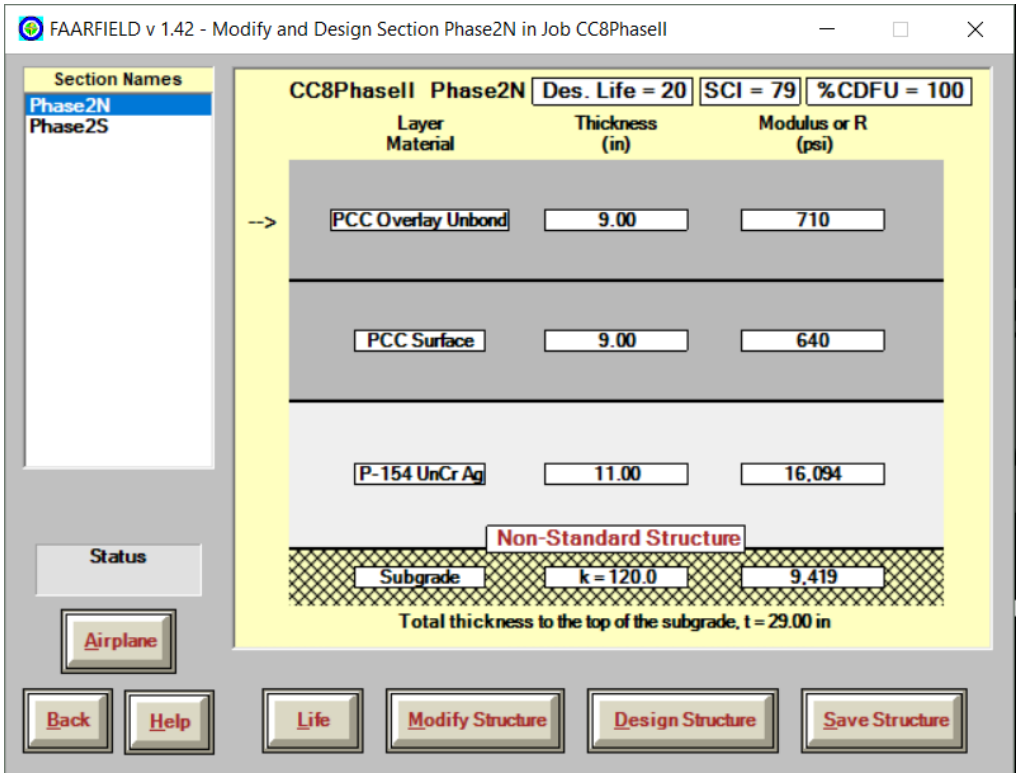

(a) North Test Item

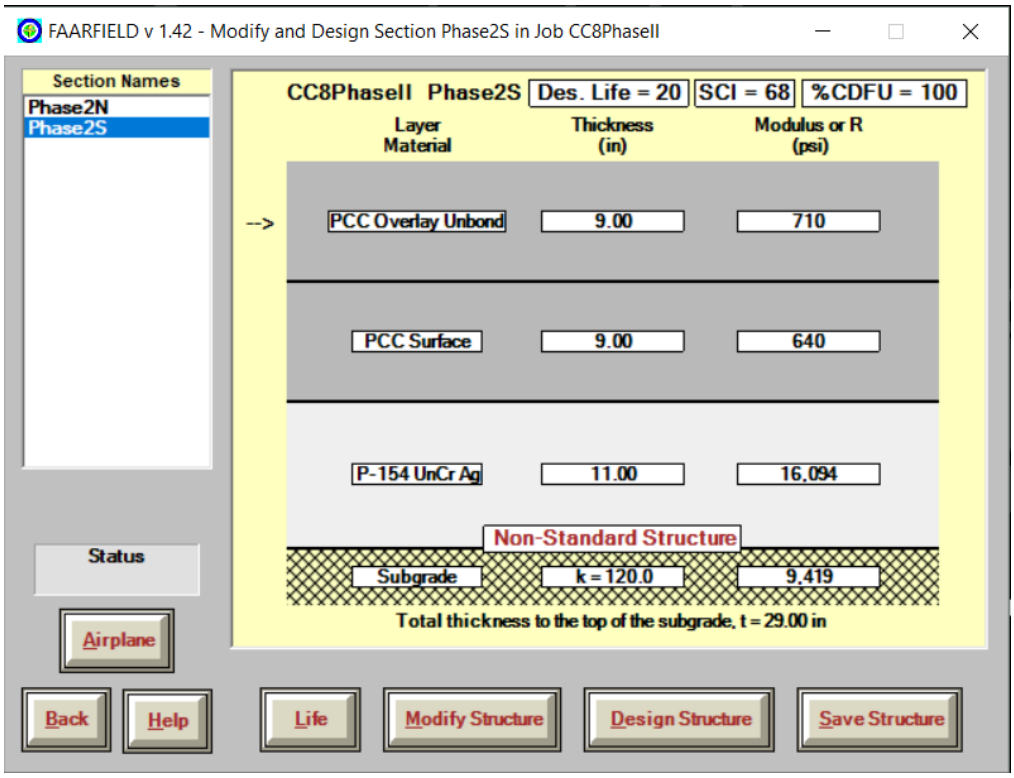

(b) South Test Item

Figure 8. FAARFIELD 1.42.0003 Comparative Life Computations

Table 1. FAARFIELD Predictions for the North Test Item (3D)

Wheel Load, lb.	Maximum Horizontal Stress, psi		Failure Passes
	Edge	Interior	
35000	433	432	54545
37500	454	457	14724
40000	475	483	4453
42500	496	507	1366
45000	516	532	477
47500	537	556	195
50000	557	580	93
52500	577	603	47
55000	597	627	25

Table 2. FAARFIELD Predictions for the South Test Item (2D)

Wheel Load, lb.	Maximum Horizontal Stress, psi		Failure Passes
	Edge	Interior	
35000	441	420	58537
37500	462	445	19835
40000	483	469	7339
42500	504	492	2978
45000	525	515	1304
47500	546	538	610
50000	566	561	303
52500	587	583	120
55000	607	605	64

(a) North Test Item

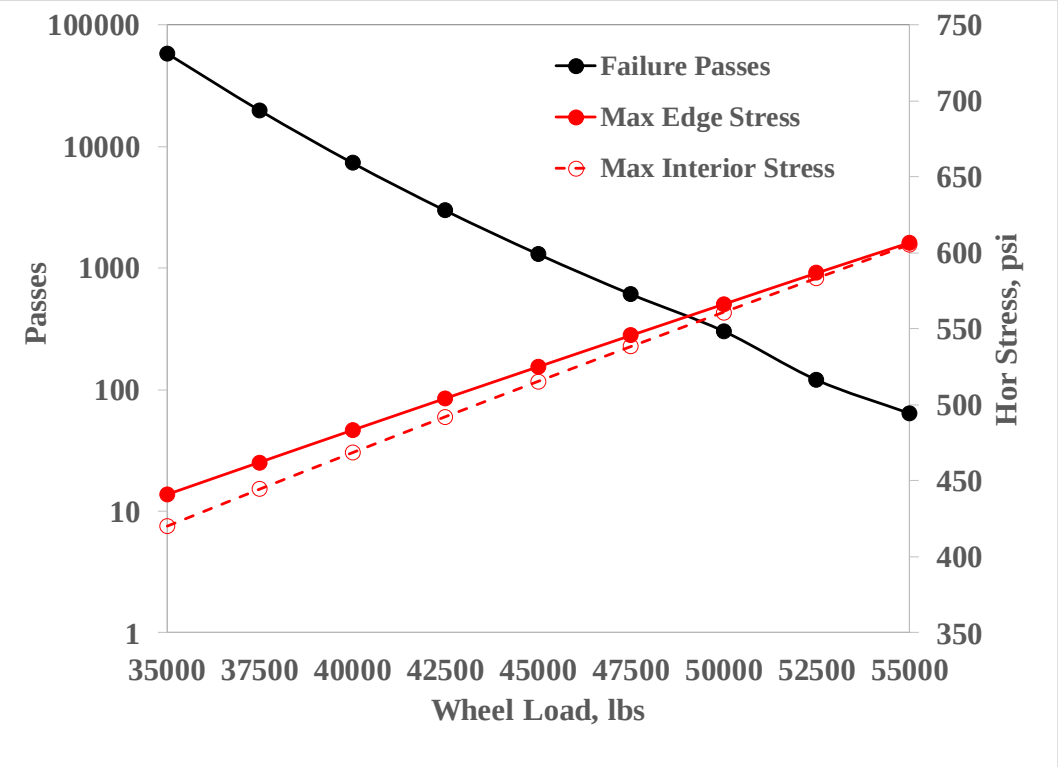

(b) South Test Item

Figure 9. FAARFIELD Predictions

3.2.2 TEST PROCEDURE

a. General. All traffic was conducted at a vehicle speed of 2.5 mph and with a nominal tire pressure of 220 psi.
b. Wander Pattern. The wander pattern consisted of 66 passes (Table A1 of Appendix A), with each passage of the NAPTV to the east being counted as a pass, and the return to the west counted as a second pass. These 66 passes were arranged in 9 wheel tracks, as shown in Table 3. For Track 0, the outside tire of each dual aligned with the longitudinal joint centered within each test item. Detailed carriage positions for each pass for 1 full wander can be found in Table A1 of Appendix A.
c. Slab Identification. All slabs were labeled as shown in Figure 4.
d. HWD Location. HWD test locations were marked at the center of all 12x12 ft. slabs and slab corners where ECS deflection sensors were installed. In addition, joint load transfer was evaluated at the transverse joint of STA 3+42, 3+54, 3+66, and 3+78.
e. Flexural Strength. Prior to traffic test, flexural strength test ASTM C78 was conducted on the beams cast during concrete placement and field cured. FAARFIELD was then re-run with in-situ R values to obtain more realistic maximum slab stresses.
f. Seating Loads. The test pavement was trafficked using the wander pattern shown in Figure 10 and as detailed in Table A2 of Appendix A. The seating load wander was conducted using a two-wheel (D) gear at a load of 10,000 pounds per wheel. This seating occurred every 10-

inches across the pavement width. Slab vertical movements were monitored using ECS deflection sensors and the effects of seating loads were noted.

g. Baseline HWD and PSPA. The baseline HWD and PSPA measurements were used to back-calculate layer moduli, and to monitor slab curling and changes of support conditions. After the seating load wander, HWD tests were performed at the locations specified in (d). The HWD testing was conducted with a four-drop loading sequence beginning with an approximate 36,000 pound seating load. The subsequent loads were approximately 12,000 pounds, 24,000 pounds, and 36,000 pounds. All PSPA measurements were collected from slab centers.

h. Ramp-up Response Test with full wander pattern. The purpose of this test was to make sure all systems were operating properly, and to assist in selecting the wheel load for the traffic test. Six-wheel and four-wheel gears were used for the north and south test item, respectively.
   1) A full traffic wander (66 passes) was applied on both north and south at a wheel load of 40,000 pounds. The condition of slabs was monitored to verify that test items were not damaged. Baseline sensor readings were recorded for both Phase I and II dynamic sensors. During Phase II testing, Phase I dynamic sensor responses were continuously collected and analyzed to monitor the deterioration of underlay concrete slabs.
   2) For both north and south test items, critical tracks of maximum strain gage responses were verified for Phase II embedded strain gages only.
   3) For both north and south test items, the extreme fiber strains based on gage locations from (2) were extrapolated. Next, both slab top and bottom stresses were estimated. Finally, these stresses were compared to the in-situ flexural strength and FAARFIELD calculations.
   4) For both north and south test items, the wheel load was increased in 2,500 pound increments. The critical tracks were trafficked in both directions (W→E and E→W). Step 3 was repeated until both of the following conditions were satisfied:
      - The maximum between the estimated slab top and bottom stress was 90% of the in-situ overlay flexural strength, R
      - The average of the estimated slab top and bottom stress was 80% of the in-situ overlay flexural strength, R

i. Traffic Test. The north test item was trafficked using a 3D gear and the south test item using a 2D gear at the same wheel loading determined from (h). Traffic continued until a single digit SCI condition was achieved on both sides. When a single digit SCI was attained on either test item, traffic was stopped on that item, but continued on the other test item until the SCI reached the target value.

Table 3. Wander Pattern

Track No.	Carriage Centerline Location, ft.	
	North	South
-4	-18.662	11.838
-3	-17.809	12.691
-2	-16.956	13.544
-1	-16.103	14.397
0	-15.250	15.250
1	-14.397	16.103
2	-13.544	16.956
3	-12.691	17.809
4	-11.838	18.662

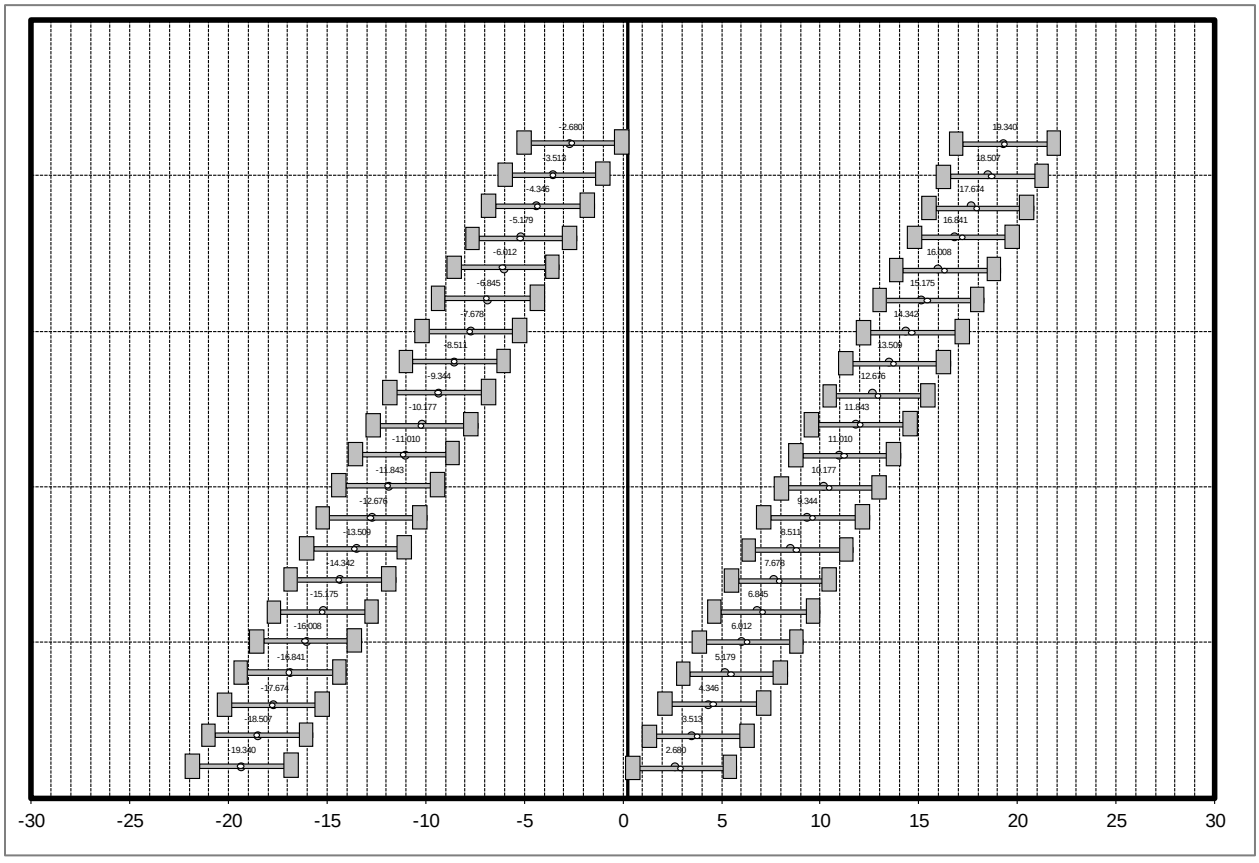

Figure 10. Seating Load Wander

3.2.3 MONITORING

a. Dynamic Responses. Embedded strain gage (EG) and Eddy Current sensor (ECS) data were collected through components of the data acquisition system called Signal Processing Units (SPUs), which allow manipulating raw signals acquired from a wide range of sensors to get values in engineering units. During traffic test, dynamic responses were monitored for any rupture at gage locations. For subsequent data analysis, raw data files were processed and stored.
b. Static Responses. The temperature and moisture data, which are entirely static (not load-dependent), were collected hourly to monitor environmental changes.
c. Pavement Condition.
    1) Manual Distress Survey. Distress survey was conducted daily for all 12x12 ft. slabs except for the center lane. The test pavement was observed informally after each wander and occurrences of any distresses were noted. Longitudinal, transverse and diagonal cracking; corner breaks; intersecting cracks and shattered slabs; and shrinkage cracking were surveyed following ASTM D5340 and considered for the calculation of the Structural Condition Index (SCI). Surveys were augmented with wire brushes, chalk markings, flashlights and other tools to ascertain the presence and pattern of very fine cracks as needed. Cumulative plots of crack mapping were submitted to the Principal Investigators (PIs) on a daily basis. The distresses were color-coded to separate dates/passes of distress survey on which new distresses were observed.
    2) Structural Condition Index (SCI) Calculation. After each distress survey, pavement inspections were updated in the PAVEAIR database and the SCI was calculated considering only those distress types associated to pavement fatigue damage as detailed in step (1).
    3) HWD and PSPA testing was conducted on a weekly basis.

4. FULL SCALE TEST

4.1 RAMP-UP RESPONSE TEST

The ramp-up response test in preparation for the CC8 Phase II Overlay traffic test was conducted October 3-4, 2017. The pavement was trafficked with a full wander at a wheel load of 40,000 pounds and the response of embedded strain gages (EGs) was monitored. Upon completion of the full wander, the raw data was processed and analyzed. For each pass, the maximum strain response was computed for all EGs.

The maximum tensile strain response of the EGs installed at the top of the overlay was observed to be smaller than at the bottom for both the north and south test item. The critical wander positions in the north test item corresponded to tracks (-2) and (-1) for the EGs at the top and bottom of the overlay, respectively. The maximum tensile strain at the top and bottom of the overlay in the north was captured by EG-N-O-II-9 and EG-N-O-II-16, respectively. In the south test item, track (1) was found to be the critical wander position for both EGs at the top and

bottom of overlay. The maximum tensile strain at the top and bottom of the overlay in the south was captured by EG-S-O-II-5 and EG-S-O-II-4, respectively.

For subsequent wheel load increments, only two vehicle passes (W→E and E→W) on each critical wander position were applied. The ramp-up test continued at three additional wheel load increments: 45,000, 50,000, and 55,000 pounds. The maximum strain responses recorded by the monitored EGs were linearly extrapolated to estimate the strains at both the top and bottom extreme fibers. Using the maximum horizontal stress predicted by FAARFIELD and the measured flexural strength of field cured beams, FAARFIELD based horizontal strains were obtained for different wheel load levels. These strains were used to define the envelope for maximum allowable responses during the ramp-up test. In Figures 11 and 12, allowable response envelopes at 80% and 90% of the design are compared to the extrapolated maximum tensile strains at the extreme fiber for both the north and south test item.

Figure 11 and Figure 12 show that, regardless of the wheel load magnitude, the extrapolated tensile strains at the top extreme fiber are well below the 80% envelope in both test items. Conversely, the tensile strains at the bottom extreme fiber fell on or slightly below the 80% envelope in the north test item, and in-between the 80% and 90% envelope in the south test item. Although the bottom tensile strains in the south test item appeared to increase with increasing wheel load (Figure 13b.), none of the extrapolated tensile strains exceeded the 90% design envelope. Given the unexpected discrepancy between design and measured responses even at wheel loads as high as 55,000 pound, a replicate of the ramp-up response test was conducted on October 4, 2017 to confirm the results from the first test. Even at a wheel load of 60,000 pounds, the extrapolated tensile strains never exceeded the 90% envelope during the second replicate. Thus, a wheel load of 55,000 pounds was conservatively selected to conduct the traffic test.

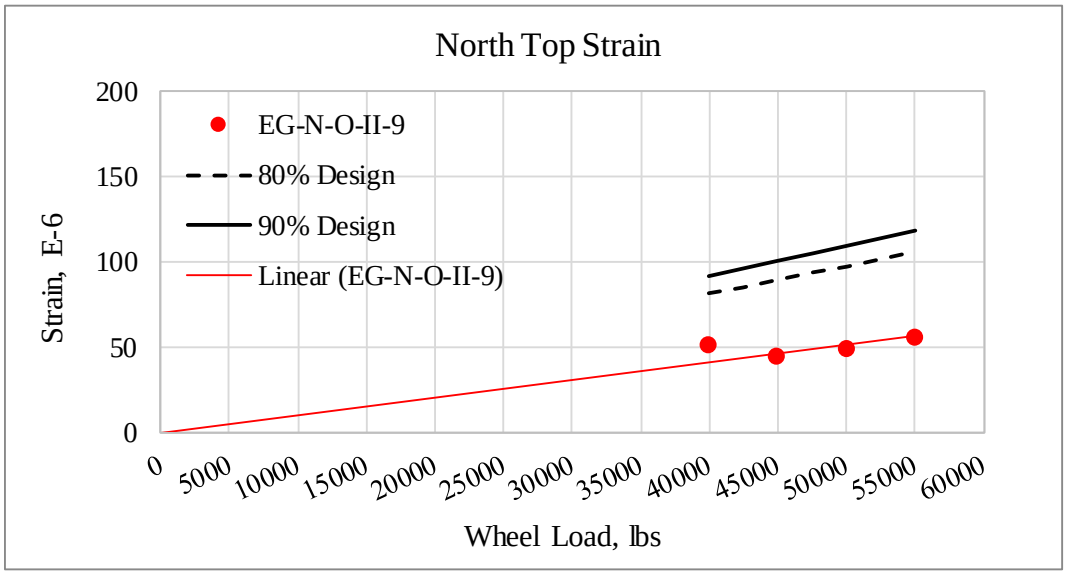

(a) Top Strain

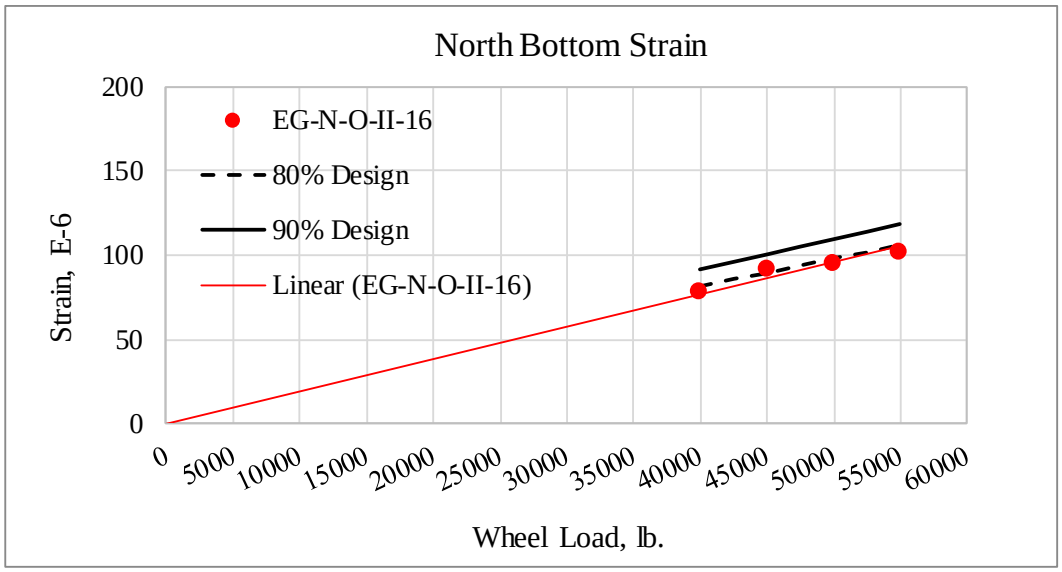

(b) Bottom Strain

Figure 11. Ramp-up Response Test Results, North Test Item (10/03/2017)

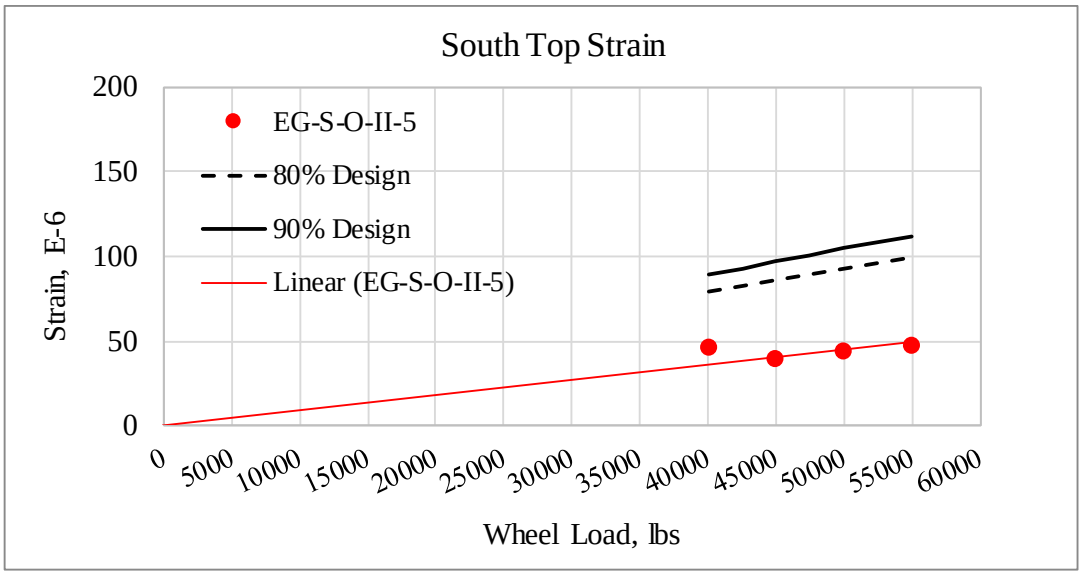

(a) Top Strain

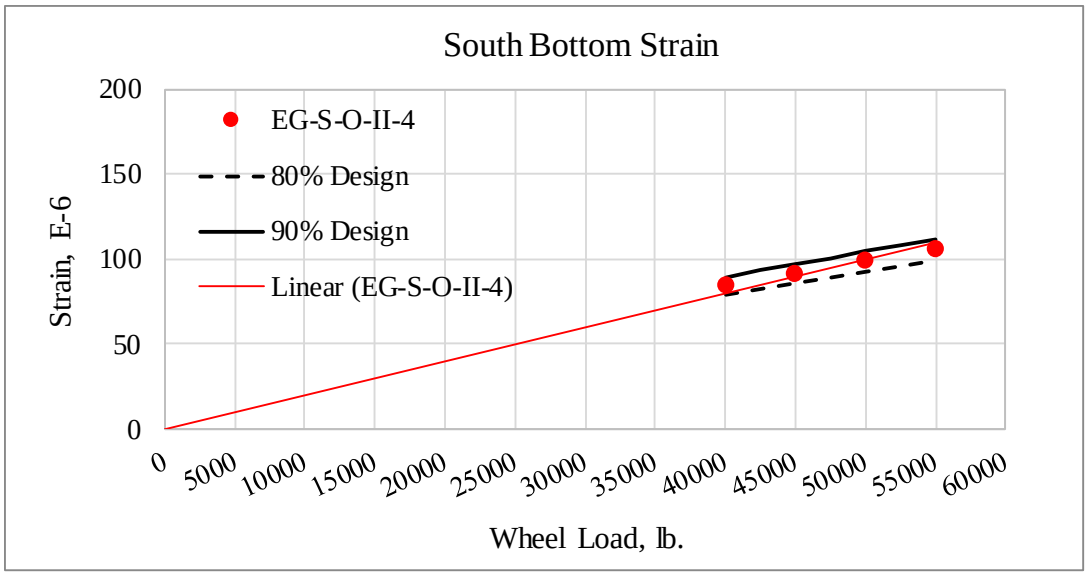

(b) Bottom Strain

Figure 12. Ramp-up Response Test Results, South Test Item (10/03/2017)

4.2 TRAFFIC TEST

Traffic testing was conducted using the NAPTV with a 3D gear configuration for the north test item and 2D for the south test item. The test was performed on both test items at a wheel load of 55,000 pounds, vehicle speed of 2.5 mph and nominal tire pressure of 220 psi. The wander pattern consisted of 66 passes, with each passage of the NAPTV from west to east being counted as a pass, and the return from east to west counting as a second pass. These 66 passes are arranged in 9 wheel tracks, as presented in Table A1 (Appendix A). Throughout the duration of traffic testing, HWD and PSPA data were collected on a weekly basis. Pavement distress surveys were conducted at the end of each trafficking day.

The initial goal for the traffic test was to achieve a single digit SCI on both the north and south test items. The traffic test started on October 10, 2017. The traffic test was terminated in the south test item on January 11, 2018 after a total of 29,370 vehicle passes were completed and a SCI value of 8 was attained. Traffic continued in the north test item until a SCI value of 11 was achieved on February 1, 2017 after a total of 37,290 vehicle passes were applied. A summary of the traffic history is presented in Table 4.

Table 4. Traffic History

Day No	Date	Number of Passes	Number of Wanders	Cumulative Passes (North)	Cumulative Passes (South)
1	10/10/2017	660	10	660	660
2	10/11/2017	660	10	1320	1320
3	10/12/2017	660	10	1980	1980
4	10/16/2017	660	10	2640	2640
5	10/17/2017	660	10	3300	3300
6	10/18/2017	660	10	3960	3960
7	10/19/2017	660	10	4620	4620
8	10/23/2017	660	10	5280	5280
9	10/24/2017	660	10	5940	5940
10	10/25/2017	660	10	6600	6600
11	10/26/2017	660	10	7260	7260
12	10/30/2017	660	10	7920	7920
13	10/31/2017	660	10	8580	8580
14	11/1/2017	660	10	9240	9240
15	11/2/2017	660	10	9900	9900
16	11/6/2017	660	10	10560	10560
17	11/7/2017	660	10	11220	11220
18	11/8/2017	660	10	11880	11880
19	11/9/2017	330	5	12210	12210
20	11/13/2017	660	10	12870	12870
21	11/14/2017	660	10	13530	13530
22	11/15/2017	660	10	14190	14190
23	11/16/2017	660	10	14850	14850
24	11/20/2017	410	6.2	15260	15260
25	11/21/2017	250	3.8	15510	15510
26	11/27/2017	660	10	16170	16170
27	11/28/2017	660	10	16830	16830
28	11/29/2017	660	10	17490	17490
29	11/30/2017	660	10	18150	18150
30	12/4/2017	660	10	18810	18810
31	12/5/2017	660	10	19470	19470
32	12/6/2017	660	10	20130	20130
33	12/7/2017	660	10	20790	20790
34	12/11/2017	660	10	21450	21450
35	12/12/2017	660	10	22110	22110
36	12/13/2017	660	10	22770	22770
37	12/14/2017	528	8	23298	23298
38	12/18/2017	660	10	23958	23958
39	12/19/2017	660	10	24618	24618
40	12/20/2017	500	7.6	25118	25118
41	12/21/2017	490	7.4	25608	25608
42	12/26/2018	275	4.2	25883	25883
43	1/2/2018	385	5.8	26268	26268
44	1/3/2018	660	10	26928	26928
45	1/8/2018	462	7	27390	27390
46	1/9/2018	660	10	28050	28050
47	1/10/2018	660	10	28710	28710
48	1/11/2018	660	10	29370	29370
49	1/16/2018	660	10	30030	
50	1/17/2018	660	10	30690	
51	1/18/2018	660	10	31350	
52	1/22/2018	660	10	32010	
53	1/23/2018	660	10	32670	
54	1/24/2018	660	10	33330	
55	1/25/2018	660	10	33990	
56	1/26/2018	660	10	34650	
57	1/29/2018	660	10	35310	
58	1/30/2018	660	10	35970	
59	1/31/2018	660	10	36630	
60	2/1/2018	660	10	37290	

In Table 4, partial numbers of wanders are observed between November 20 and 21, December 20 and 21, and December 26 and January 2. In all three cases, the partial wanders were completed on the next day of traffic test. The detailed explanation for these partial wanders is provided below:

- On November 20, traffic was suspended because one of the tires in carriage 2 registered high temperature. The partial wander was completed on November 21.
- On December 20, traffic was suspended due to low tire pressure in carriage 2, module 4. After the tire was replaced, the partial wander was completed on December 21.
- On December 26, traffic was suspended to conduct troubleshooting after two Variable Frequency Drive (VFD) faults occurred at station 405. The partial wander was completed on January 2.

5. BEHAVIOR OF TEST SECTION UNDER TRAFFIC

5.1 DISTRESS MAPPING

Distress mapping for CC7 was conducted on a daily basis after each day of trafficking. Distress surveys followed ASTM D5340 (*7*). All identified distresses were outlined with chalk when needed and measured using a tape measure. Any changes to existing distress were recorded along with any new distresses.

Results of visual distress surveys were documented in two ways: a scale map and a written log. The map displays all distresses found on the pavement on a scale drawing and keys the distress to the wander sequence number, station number, and slab identification number. Figure 13 provides a small sample of the distress graphic map. The distresses are numbered for reference to the written log. The greyed out area is the wander pattern location. On the left side, the station numbers are identified. The full length of the map is best viewed in digital form given the length to width ratio of the test pavement. All the distress maps generated during tCC8 Phase II Overlay Test are provided in Appendix B.

The written log provides all the distress information chronologically. Figure 14 provides a screenshot sample of the distress map written log. The written log documents the date of entry, the pass number, the type of distress, the distress number – which can be referenced to the graphic distress map, the location of the distress, and any relevant notes. The notes would indicate changes to existing distress, severity levels, merging of multiple previously identified distresses, etc. A complete written log is provided in Appendix C.

Minor surface cracking directly above some EGs that was observed prior to the traffic test is registered in the baseline distress survey. During the early stage of the traffic test, tight surface cracks isolated in the interior of slabs and developed in a random pattern, were observed in the north test item. In general, the south test item showed structural cracks and failed earlier than the north. Also, more corner breaks were observed on the south test item compared to the north. On both test items, corner breaks and longitudinal cracks were the dominant distress types. Development of reflective cracking from the underlay longitudinal joints was observed within the trafficked area on both test items. Additional analysis on the pattern of distress development will be elaborated in following sections of the report.

COLOR	DATE	INTIALS	TOTAL PASSES
	4/28/2017	JMD	0
	5/5/2017	JMD	0
	10/3/2017	JMD	0
	10/10/2017	JMD	660
	10/11/2017	JMD	1320
	10/12/2017	JMD	1980
	10/16/2017	JMD	2640
	10/17/2017	JMD	3300
	10/18/2017	JMD	3960
	10/19/2017	JMD	4620
	10/23/2017	JMD	5280

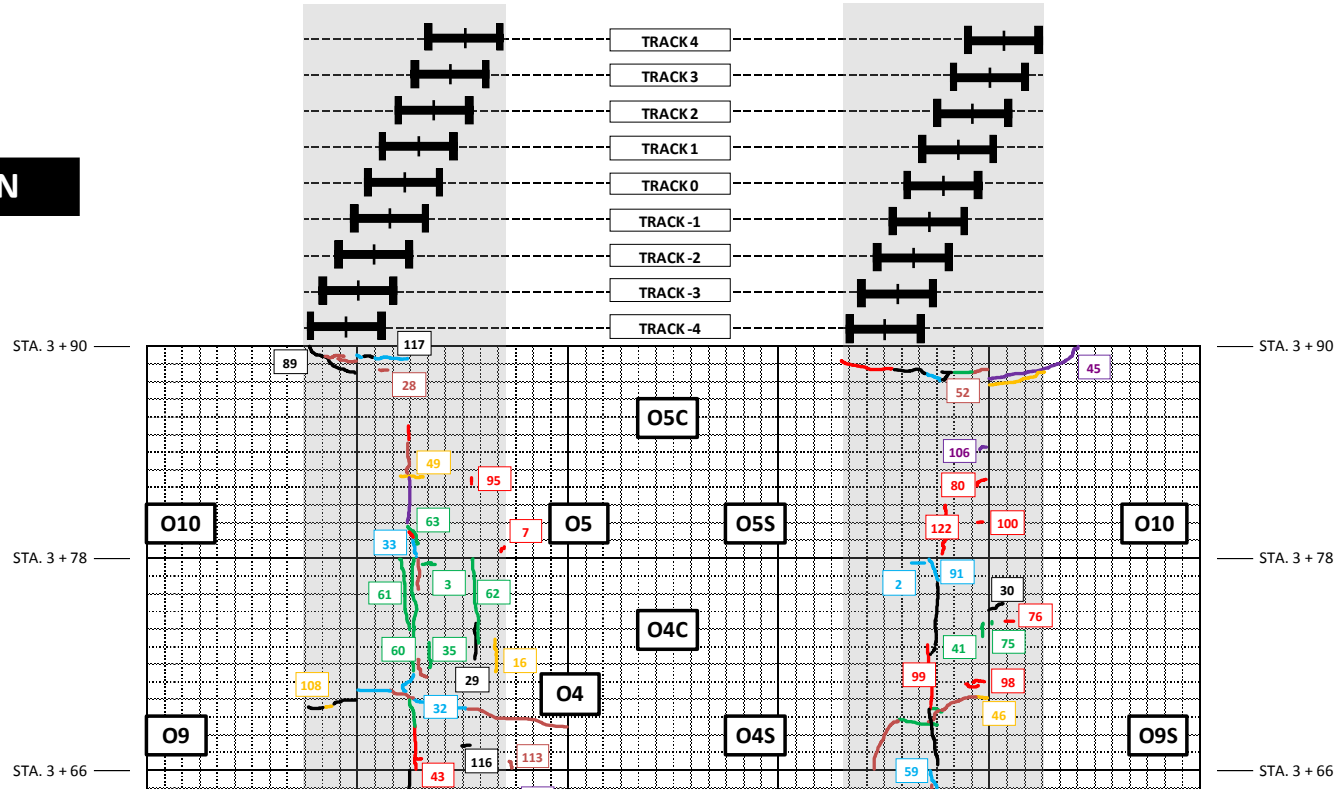

Figure 13. Example Section of Distress Map

DATE	TOTAL PASSES		DAILY PASSES	DISTRESS								NOTES
				DESCRIPTION	NO.	LOCATION						
						X AXIS (in.)			Y AXIS (in.)		SLAB	
	NORTH	SOUTH				WEST	MIDDLE	EAST	INITIAL	END		
4/28/2017	0	0	0	Shrinkage Crack	1		3		45	51	O2S	Crack is directly above sensor 1" below the surface.
5/5/2017	0	0	0	Shrinkage Crack	2		141		45	51	O4S	Crack is directly above sensor 1" below the surface.
10/3/2017	0	0	0	Shrinkage Crack	3		142		92	94	O4N	Crack is directly above sensor 1" below the surface. Found after 1 wander (66 passes) @ 40k lbs. as part of the ramp up pre-traffic testing.
10/3/2017	0	0	0	Shrinkage Crack	3		142		92	98	O4N	After track loads of 45k and 50k lbs. as part of the ramp up pre-traffic testing, the distress expanded to cover the full length of the embedded sensor.
10/3/2017	0	0	0	Shrinkage Crack	4		3		99	100	O7S	Crack is directly above sensor 1" below the surface. Found after 1 wander (66 passes) @ 40k lbs. and track loads of 45k and 50k lbs. as part of the ramp up pre-traffic testing.
10/10/2017	660	660	660	Shrinkage Crack	5		3		92	102	O2N	Crack is directly above sensor 1" below the surface.
10/10/2017	660	660	660	Shrinkage Crack	6	0		28	45	45	O3N	
10/10/2017	660	660	660	Shrinkage Crack	7	5		7	43	45	O5N	Crack emanates from a missing 1/2" aggregate at the pavement surface.
10/10/2017	660	660	660	Shrinkage Crack	8	141		148	9	15	O1S	
10/11/2017	1320	1320	660	Shrinkage Crack	9	17		28	90	90	O1N	
10/11/2017	1320	1320	660	Shrinkage Crack	10	71		79	41	41	O3N	
10/11/2017	1320	1320	660	Shrinkage Crack	11	34		54	35	35	O3N	
10/11/2017	1320	1320	660	Shrinkage Crack	12	24		34	35	45	O3N	
10/11/2017	1320	1320	660	Shrinkage Crack	13	110		125	35	35	O3N	
10/11/2017	1320	1320	660	Shrinkage Crack	14	135		144	45	45	O2S	

Figure 14. Example Section of Written Log

5.2 STRUCTURAL CONDITION INDEX (SCI) EVALUATION

A key element in the CC8 Phase II Overlay Test is continual pavement condition monitoring. Throughout the traffic testing, the structural performance of the test pavement was monitored and quantified by means of the SCI. SCI is a modification of the Pavement Condition Index (PCI) for Airports (rigid) method following ASTM D 5340 (*7*). Like PCI, SCI is based on visual inspection of the pavement surface and identification of standard distresses. The difference is that in the SCI only distresses related to structural loading are counted, while environmental and construction/material-related distresses are disregarded. In the field, pavements are divided into "sample units," and a subset of sample units is then randomly selected for inspection. Due to the small size of test area, the south and north test item were considered to constitute two separate sample units, and 100% of the slabs in each unit (i.e.; ten slabs) was inspected during the survey.

Surface cracks appeared directly above some EGs prior to commencement of the traffic test. Therefore, two sets of SCI values were calculated. For the first set, denominated "standard SCI," existing cracks prior to traffic were considered. For the second set, denominated "initial SCI," these cracks were excluded from the calculation. In Table 5, the two sets of SCI estimates are presented. Note that the number of passes, wanders and coverage are given as cumulative values. Due to the consideration of pre-existing cracks, the "standard SCI" values in Table 5 are slightly lower than the "initial SCI." However, both sets of SCI values eventually converge. For the north test item, the convergence occurred after only three days of traffic whereas for the south test item, towards the end of the traffic test. The "initial SCI" set was used for all the subsequent analysis presented in following sections.

Figure 15 illustrates the changes in SCI for each test item over the course of trafficking. The deterioration in the south test item is evidently faster than the north. The total number of vehicle passes required to achieve similar levels of deterioration upon traffic termination was 37,290 for the north test item whereas only 29,370 for the south test item. Under comparable structural conditions the north test item would be expected to fail first given that the 3D gear configuration is 50% heavier than the 2D used in the south. In Table 6, a comparative summary of the as-built properties of both test items is presented. Statistically, except for the k-value of P-154 subbase material, there was little to no discrepancy in as-built properties between the north and south test item. Furthermore, the fact that the P-154 layer in the south test item presented a higher k-value than the north, indicates stronger support conditions underneath the underlay in the south which in turn should contribute to extend rather than reduce the pavement life. Therefore, as-built properties can be ruled out as source of unexpected rapid deterioration in the south test item.

Table 5. Structural Condition Index (SCI)

Day No	Date	Passes	Wanders	Coverages	Standard SCI		Initial SCI	
					North	South	North	South
0	10/3/2017	0	0	0	98	95	100	100
1	10/10/2017	660	10	164	94	94	95	98
2	10/11/2017	1320	20	328	92	94	94	97
3	10/12/2017	1980	30	493	92	86	92	88
4	10/16/2017	2640	40	657	92	86	92	88
5	10/17/2017	3300	50	821	92	86	92	87
6	10/18/2017	3960	60	985	92	85	92	86
7	10/19/2017	4620	70	1149	92	85	92	86
8	10/23/2017	5280	80	1313	92	85	92	86
9	10/24/2017	5940	90	1478	92	80	92	80
10	10/25/2017	6600	100	1642	92	80	92	80
11	10/26/2017	7260	110	1806	92	80	92	80
12	10/30/2017	7920	120	1970	92	63	92	64
13	10/31/2017	8580	130	2134	92	59	92	60
14	11/1/2017	9240	140	2299	86	59	86	60
15	11/2/2017	9900	150	2463	86	59	86	60
16	11/6/2017	10560	160	2627	86	59	86	60
17	11/7/2017	11220	170	2791	86	59	86	60
18	11/8/2017	11880	180	2955	86	59	86	60
19	11/9/2017	12210	185	3037	86	59	86	60
20	11/13/2017	12870	195	3201	86	54	86	55
21	11/14/2017	13530	205	3366	81	49	81	50
22	11/15/2017	14190	215	3530	73	49	73	50
23	11/16/2017	14850	225	3694	73	49	73	50
24	11/20/2017	15260	231	3796	73	49	73	50
25	11/21/2017	15510	235	3858	73	49	73	50
26	11/27/2017	16170	245	4022	73	48	73	48
27	11/28/2017	16830	255	4187	73	35	73	36
28	11/29/2017	17490	265	4351	73	31	73	32
29	11/30/2017	18150	275	4515	67	31	67	32
30	12/4/2017	18810	285	4679	66	27	66	28
31	12/5/2017	19470	295	4843	66	27	66	28
32	12/6/2017	20130	305	5007	66	27	66	28
33	12/7/2017	20790	315	5172	66	27	66	28
34	12/11/2017	21450	325	5336	66	27	66	28
35	12/12/2017	22110	335	5500	66	27	66	28
36	12/13/2017	22770	345	5664	38	18	38	18
37	12/14/2017	23298	353	5796	34	18	34	18
38	12/18/2017	23958	363	5960	31	10	31	11
39	12/19/2017	24618	373	6124	30	10	30	11
40	12/20/2017	25118	381	6248	25	10	25	11
41	12/21/2017	25608	388	6370	23	10	23	11
42	12/26/2018	25883	392	6439	23	10	23	11
43	1/2/2018	26268	398	6534	20	8	20	8
44	1/3/2018	26928	408	6699	20	8	20	8
45	1/8/2018	27390	415	6813	20	8	20	8
46	1/9/2018	28050	425	6978	20	8	20	8
47	1/10/2018	28710	435	7142	20	12	20	12
48	1/11/2018	29370	445	7306	20	8	20	8
49	1/16/2018	30030	455	7470	11		11	
50	1/17/2018	30690	465	7634	11		11	
51	1/18/2018	31350	475	7799	11		11	
52	1/22/2018	32010	485	7963	11		11	
53	1/23/2018	32670	495	8127	11		11	
54	1/24/2018	33330	505	8291	11		11	
55	1/25/2018	33990	515	8455	11		11	
56	1/26/2018	34650	525	8619	11		11	
57	1/29/2018	35310	535	8784	11		11	
58	1/30/2018	35970	545	8948	11		11	
59	1/31/2018	36630	555	9112	11		11	
60	2/1/2018	37290	565	9276	11		11	

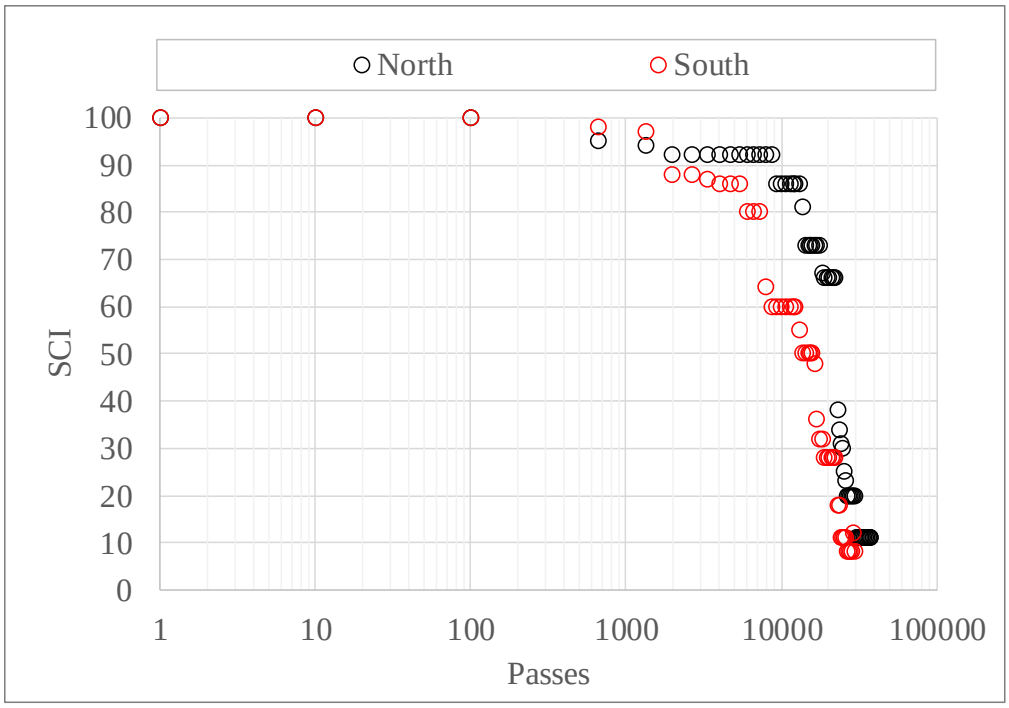

Figure 15. Overlay Structural Condition Index versus Passes

Table 6. Comparative Summary of As-built Properties

Layer	Property	North	South
PCC Overlay	Thickness, in	9.012	9.024
	271-day R, psi	688	712
HMA Interlayer	Thickness, in	1.464	1.356
PCC Underlay	Thickness, in	9.264	9.252
	179/172-day R, psi	610	638
P-154 Subbase	Thickness, in	10.78	10.88
	k-value, pci	216	272
Subgrade	CBR	7.2	7.4
	k-value, pci	110	131

It is well known that gross aircraft weight is one of the most important factors controlling airfield pavement life. Consequently, under constant wheel load and similar structural capacity, the pavement deterioration under a 3D gear should occur at a higher rate than under a 2D gear. This was consistently evidenced during the CC4 overlay tests (*3*). Figure 16 shows the changes in SCI for all test items in the CC4 Baseline Experiment. The north test items were trafficked with a 3D gear whereas the south test items with a 2D gear. As can be observed in Figure 16, the test items on the south consistently required more vehicle passes to attain a given deterioration level than the north test items. Considering the intact slab condition of the underlay and comparable as-built properties in both the north and south side of the baseline experiment, the reduced pavement life observed in the north test items was attributed to the gross aircraft weight imposed by the 3D gear.

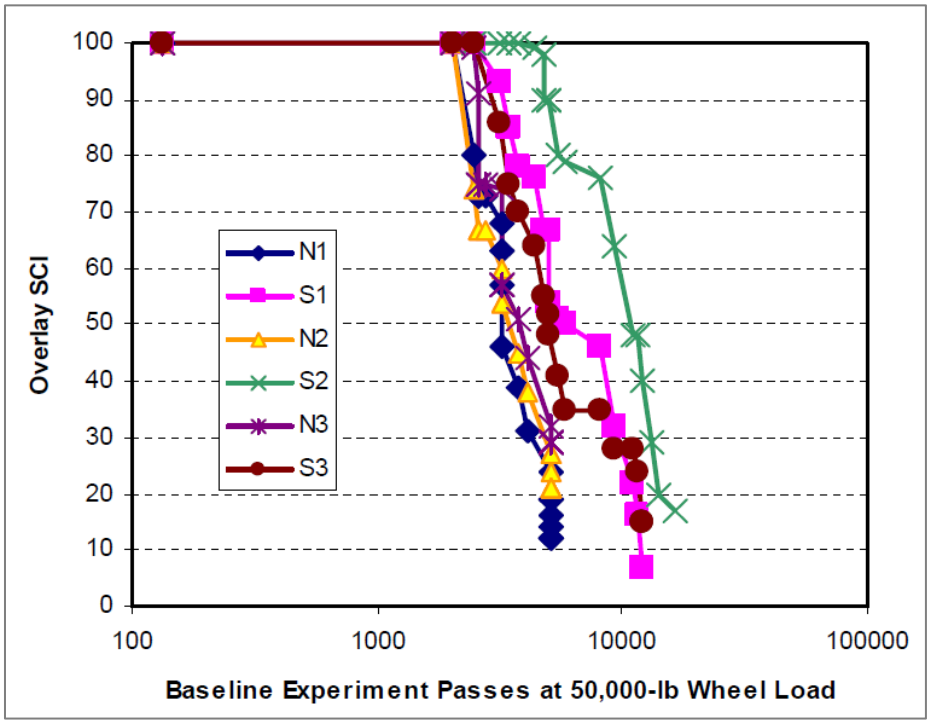

Figure 16. Overlay Structural Condition Index versus Passes, CC4 Overlay-Baseline Experiment

For the CC8 Phase II Overlay Test, the initial underlay SCI was 79 and 68 for the north and south test item respectively. In CC4, damaged slabs were used as underlay for the SCI Validation Experiment. Test items N2 and S2 in CC4, are of particular interest given that the overlay to underlay thickness ratio is the same as in CC8, and the initial underlay SCI values were 43 and 28 for the north and south test item, respectively. This difference in initial underlay SCI is similar to that in CC8 Phase II Overlay Test, although the initial condition age-wise of both experiments is not the same. Figure 17 shows the changes in SCI for all test items in the CC4 SCI Validation Experiment. Again, all test items in the south side required additional vehicle passes to achieve the same deterioration level as the test items in the north side. When specifically comparing test items N2 and S2, the damage imparted by the 3D gear was not only more significant than imparted by the 2D gear but also seemed to offset the existing initial SCI

deficit in S2. These findings reported in the CC4 SCI Validation Experiment confirm the significance of the aircraft gross weight as a factor driving the pavement performance.

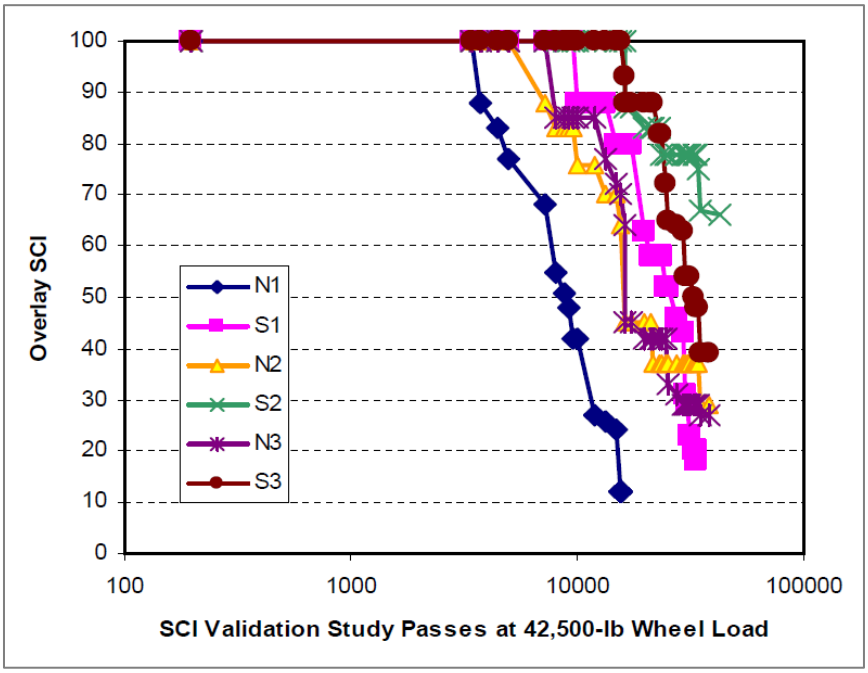

Figure 17. Overlay Structural Condition Index versus Passes, CC4 Overlay-SCI Validation

Given that the changes in SCI observed for both test items in the CC8 Phase II Overlay Test are not consistent with the anticipated effect of the gear load, and the as-built properties were ruled out as source of distortion in the expected performance trends; other factors must be investigated. Intangible initial structural conditions of the underlay, potential for localized damage and possible effects of staggered longitudinal joints should be considered as possibilities. Advanced analysis of the observed distress pattern is elaborated later in this report.

6. DATA AND PRELIMINARY ANALYSIS

6.1 INSTRUMENTATION DATA

In this section, the analysis of data produced by the sensors installed within the overlay is presented. Also, the instrumentation data is correlated to the pavement performance.

6.1.1 THERMOCOUPLE DATA (T)

Thermocouple trees were installed in both the north and south side of the pavement in one slab to monitor temperature gradients. Each tree consists of three thermocouples to measure the temperature at the bottom, middle, and top of the slab (see Figures 4 and 5). The same thermocouple configuration was used in both the underlay and overlay. Full-scale tests at the NAPTF are indoor experiments and therefore, temperature fluctuations are small compared to

what would be observed if exposed to the sun. Changes in the overlay temperature are illustrated in Figure 18. In Figure 18a, a comparison of north versus south temperature at the top, middle and bottom of the overlay are presented. The overlay temperature was observed to range from 29°F to 77°F. The general trends showed decreasing overlay temperature as the weather shifts from fall into the winter, reaching minimum values after the first week in January. Then, a rebound in temperature was observed for the remaining traffic test.

The temperature fluctuation at top of the overlay decreased with depth. Also, a slight difference in temperature was observed between north and south thermocouples. Figure 18b shows the difference between the north and south temperature at top, midpoint and bottom of the overlay. An average temperature differential of -0.5°F evidenced that the north test item remained slightly colder than the south throughout the traffic test. This is because the south wall of the building is more exposed to sunlight than the north.

In Figure 19, temperatures measured by thermocouples installed in the underlay are compared to overlay temperatures. In both the north and south test item (Figures 19a and 19b), the underlay thermocouples generally showed higher values than the overlay which was expected given that the underlay was less exposed to cold air temperatures. In general, the shallower the thermocouple the lower the temperature.

Figure 20a shows the temperature differential between the bottom of the overlay and top of the underlay. The mean differential was found to be -0.7°F suggesting that the existing temperature gradient is not negligible. In Figure 20b the interlayer temperature throughout the traffic test was estimated as the average temperature between the bottom of the overlay and top of the underlay. As in the overlay, the interlayer temperature on the south side was found to be slightly higher than the north. The general analysis and observations on thermocouple data discussed in this section, were considered for the advanced analysis presented later in this report.

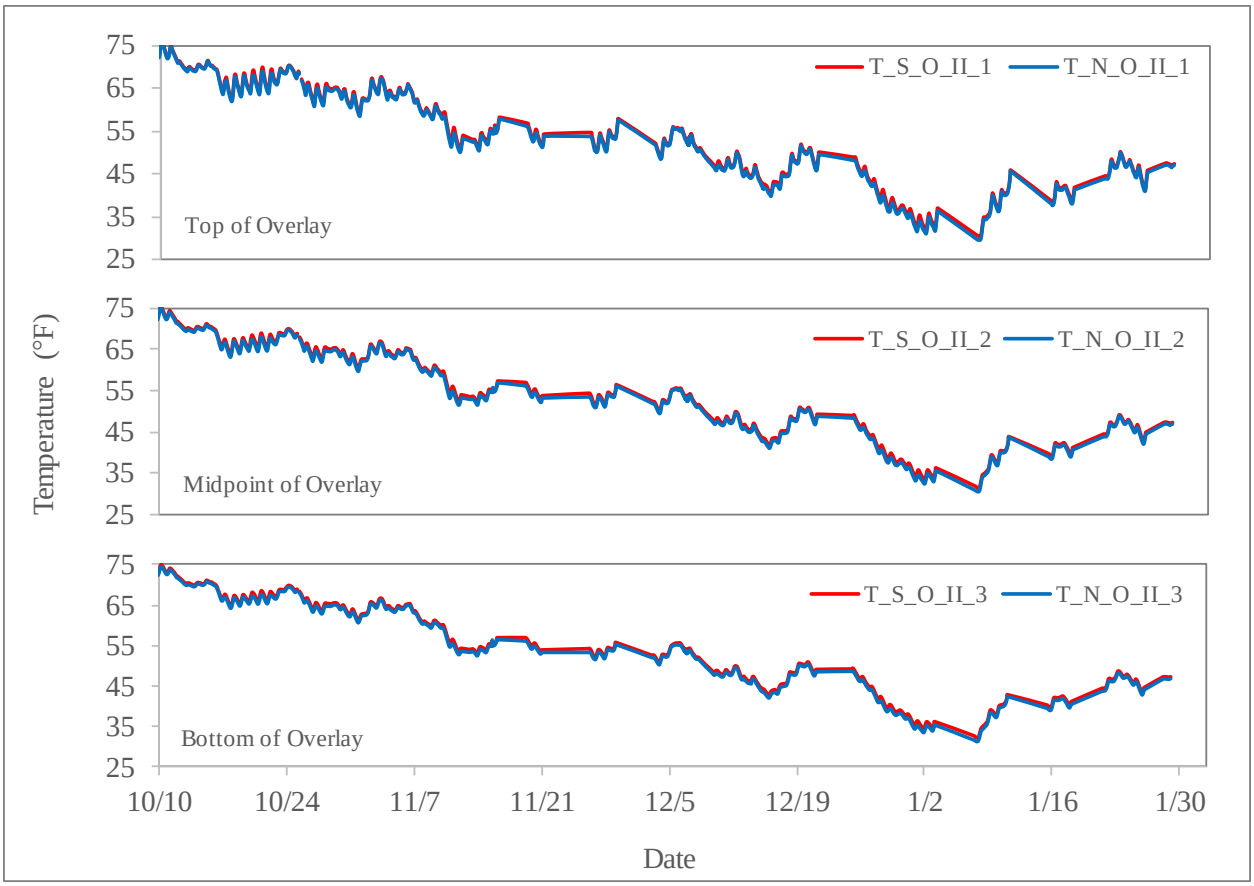

(a) Comparison: North vs. South

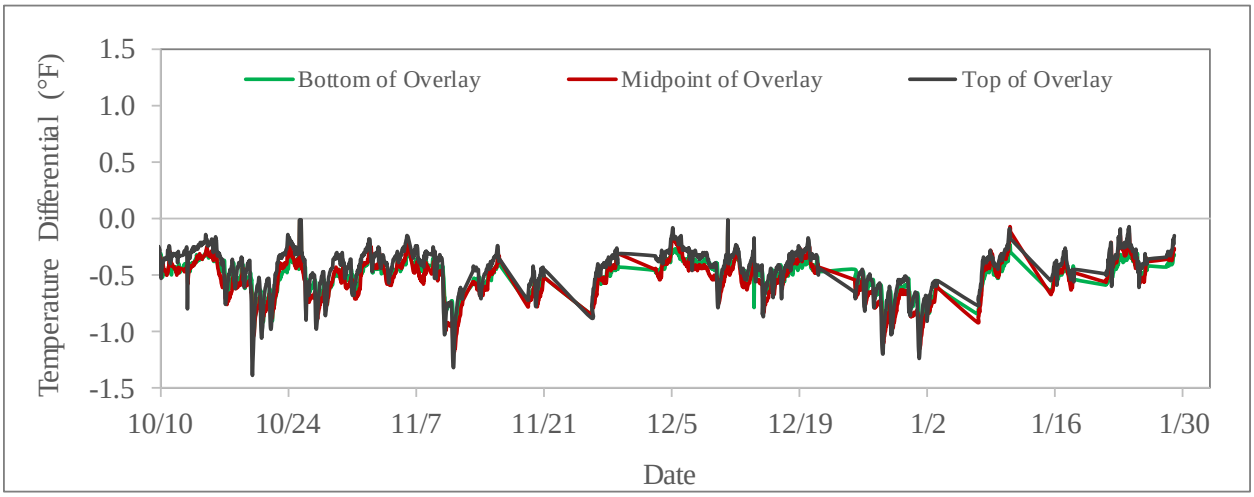

(b) Temperature Differential: North minus South

Figure 18. Overlay Thermocouple Data

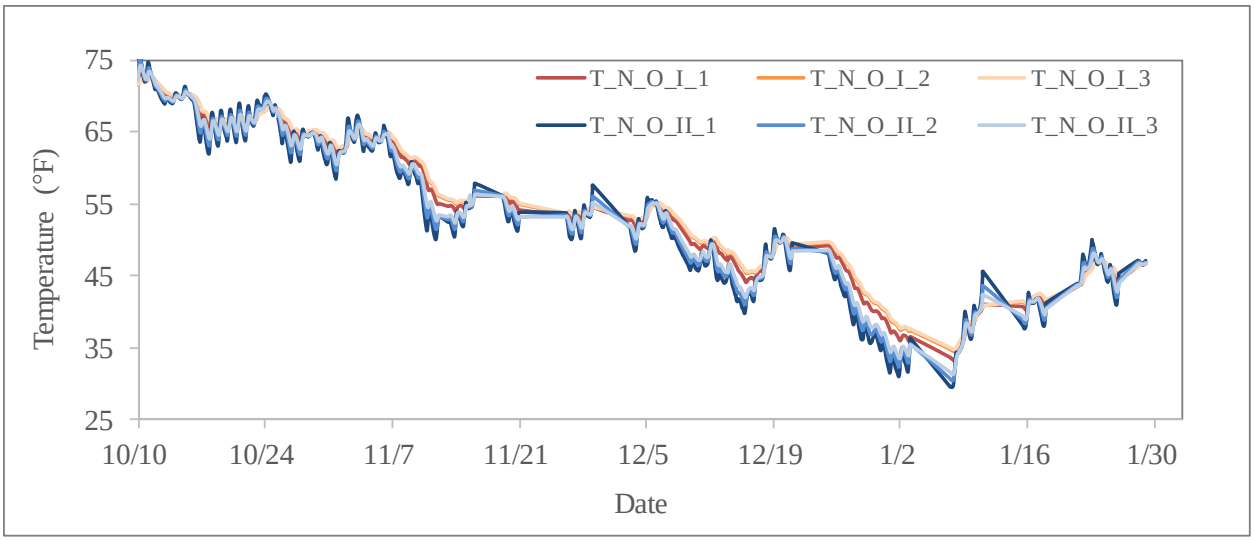

(a) North Test Item

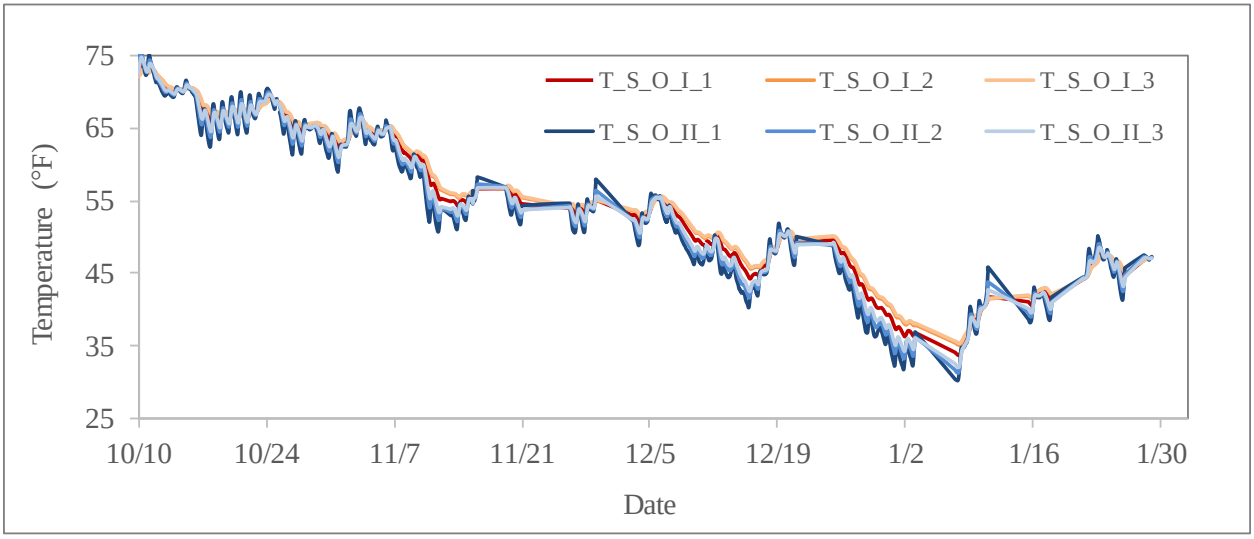

(b) South Test Item

Figure 19. Comparison of Overlay vs. Underlay Temperature Data

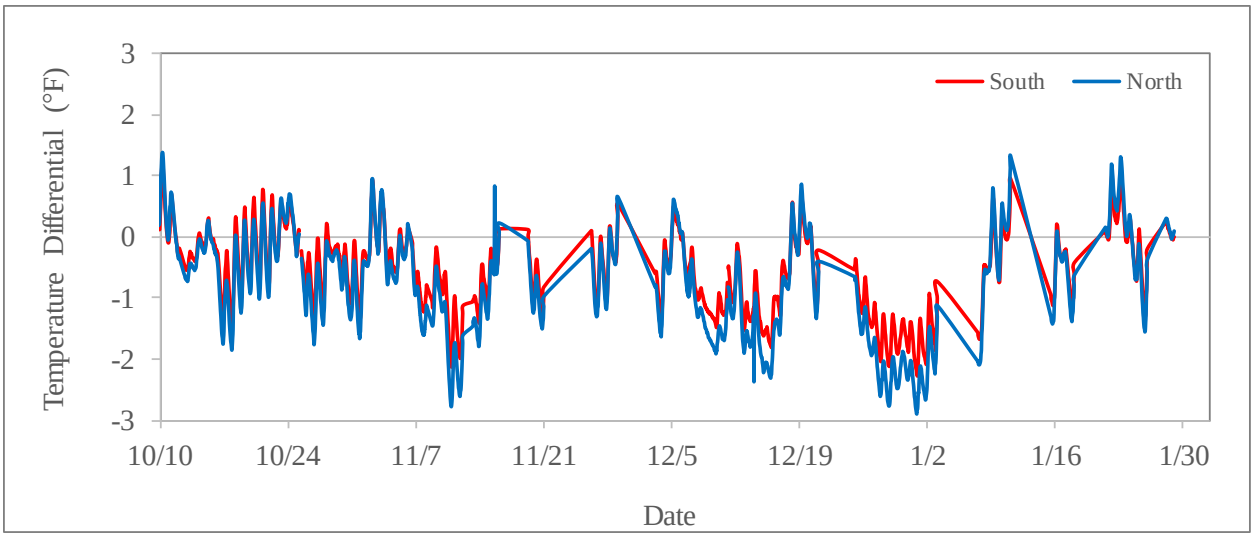

(a) Temperature Differential Between Bottom of Overlay and Top of Underlay

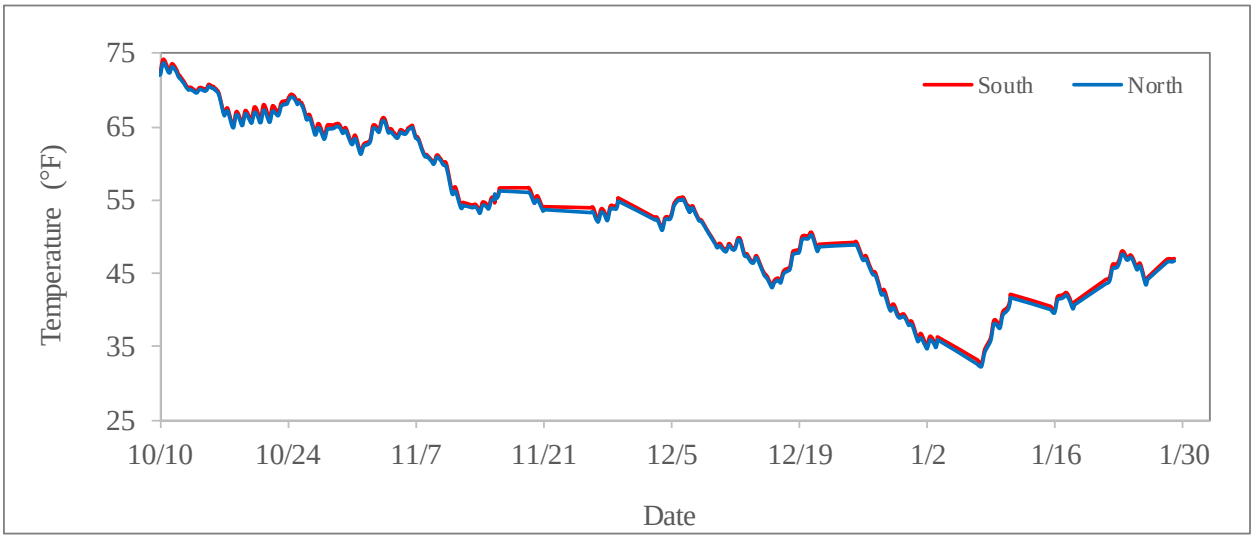

(b) Comparison of Interlayer Temperature: North vs. South

Figure 20. Estimated Temperature of the HMA Interlayer

6.1.2 EMBEDDED STRAIN GAGE DATA (EG)

6.1.2.1 CRITICAL TRACK VERIFICATION

The typical response of the EGs was monitored during the first ten wanders of the traffic test. In Table 7, the critical track corresponding to the maximum tensile strain observed for each EG is summarized. As anticipated, the critical tensile response in the EGs located near the bottom of the overlay was observed when the outer wheel in either carriage passed directly over the gage. Once the critical tracks were identified, monitoring and analysis of EG data continued ignoring all other tracks.

Table 7. Embedded Strain Gage Critical Track

North Test Item				South Test Item			
Sensor ID	Orientation	Critical Track	Offset[1] (ft.)	Sensor ID	Orientation	Critical Track	Offset[1] (ft.)
EG-N-O-II-1	Transverse	0	4.5	EG-S-O-II-1	Transverse	0	4.5
EG-N-O-II-2	Transverse	-4	1.1	EG-S-O-II-2	Transverse	4	1.1
EG-N-O-II-3	Transverse	-4	-2.4	EG-S-O-II-3	Transverse	4	-2.4
EG-N-O-II-4	Transverse	4	-0.1	EG-S-O-II-4	Transverse	-4	-0.1
EG-N-O-II-5	Longitudinal	-1	-0.1	EG-S-O-II-5	Longitudinal	1	-0.1
EG-N-O-II-6	Longitudinal	-1	-0.1	EG-S-O-II-6	Longitudinal	1	-0.1
EG-N-O-II-7	Longitudinal	0	0.3	EG-S-O-II-7	Longitudinal	0	0.3
EG-N-O-II-8	Longitudinal	0	0.3	EG-S-O-II-8	Longitudinal	0	0.3
EG-N-O-II-9	Longitudinal	-2	-1.0	EG-S-O-II-9	Longitudinal	2	-1.0
EG-N-O-II-10	Longitudinal	-1	-0.1	EG-S-O-II-10	Longitudinal	1	-0.1
EG-N-O-II-11	Longitudinal	0	0.3	EG-S-O-II-11	Longitudinal	0	0.3
EG-N-O-II-12	Longitudinal	0	0.3	EG-S-O-II-12	Longitudinal	0	0.3
EG-N-O-II-13	Transverse	0	4.5	EG-S-O-II-13	Transverse	0	4.5
EG-N-O-II-14	Transverse	-4	1.1	EG-S-O-II-14	Transverse	4	1.1
EG-N-O-II-15	Transverse	-3	-1.6	EG-S-O-II-15	Transverse	3	-1.6
EG-N-O-II-16	Transverse	4	-0.1	EG-S-O-II-16	Transverse	-4	-0.1

Note: Even and odd sensor sequential number correspond to EGs located near the top and bottom of slab, respectively
[1] *Distance from the gage position to the closest wheel for the indicated critical track*

6.1.2.2 ANALYSIS

Performance Measure using Crack Density

In addition to SCI, the crack density parameter (CD) was used to quantify the performance of concrete overlay (*2, 3*). Each overlay slab in the scale distress map was first subdivided into 144 discrete units with an area of one square foot. The CD was then visually determined as the percent of discrete units where cracking was observed. For illustration purposes, Figure 21 shows a corner break on slab O7N (green) that extends over ten discrete units (red). Hence, the CD for slab O7N was estimated as $(11 \div 144) \times 100 = 7.6\%$. The accuracy of crack density estimates increases with the number of discrete units per slab. Research conducted using CC4 data determined that 100 discrete units provided visually reasonable crack density and was time-efficient for crack density determination in 12.5 ft. square slabs (*8*). Thus, assuming 144 discrete units per slab was deemed reasonable considering the slab size (12 ×12 ft.) used in CC8. Tables 8 and 9 summarize CD (%) estimates for each slab on the north and south side, respectively.

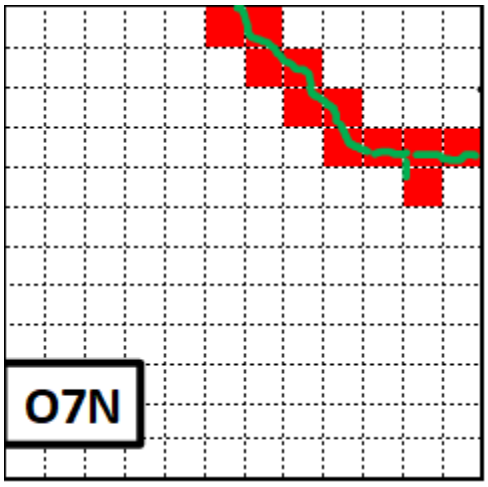

Figure 21. Crack Density Calculation for Slab O7N

In Figure 22, the changes in the averaged CD with number of vehicle passes are illustrated. An apparent decrease in the rate of change in CD occurred after approximately 23,000 vehicle passes. A side-by-side comparison between the changes in SCI and CD is given in Figure 23. As anticipated, the CD increases with decreasing SCI. The potential for CD to capture the occurrence of localized distresses is discussed in the following section

Table 8. Crack Density for All Slabs on the North Test Item

Date	Pass #	Wander	SCI	Test Item CD	CD per Slab									
					O1N	O2N	O3N	O4N	O5N	O6N	O7N	O8N	O9N	O10N
10/4/2017	100	2	100	0	0	0	0	1	0	0	0	0	0	0
10/13/2017	1980	30	92	2	3	1	7	3	1	0	0	0	0	0
10/20/2017	4620	70	92	4	8	13	8	10	3	0	0	0	0	0
10/27/2017	7260	110	92	5	8	15	8	11	4	0	0	0	0	0
11/3/2017	9900	150	86	6	10	19	9	18	4	0	0	0	0	0
11/9/2017	12210	185	86	7	10	19	10	26	6	0	0	0	0	0
11/16/2017	14850	225	73	9	12	26	20	26	6	0	0	0	0	3
11/30/2017	18150	275	67	11	15	29	20	28	8	0	1	0	1	3
12/7/2017	20790	315	66	11	17	29	20	30	10	1	1	0	2	3
12/15/2017	23298	353	34	13	23	29	20	31	17	1	3	0	2	3
12/22/2017	25608	388	25	13	23	29	20	31	18	1	3	0	2	6
1/12/2018	29370	445	20	14	24	29	20	31	19	1	3	0	2	6
1/19/2018	31350	475	11	14	24	29	20	31	19	1	3	0	2	6
1/26/2018	34650	525	11	14	24	29	20	31	19	1	8	0	2	6
2/2/2018	37290	565	11	15	24	29	20	33	20	1	8	0	4	8

Table 9. Crack Density for All Slabs on the South Test Item

Date	Pass #	Wander	SCI	Test Item CD	CD per Slab									
					O1S	O2S	O3S	O4S	O5S	O6S	O7S	O8S	O9S	O10S
10/4/2017	100	2	100	0	0	1	0	1	0	0	1	0	0	0
10/13/2017	1980	30	88	1	1	7	0	1	0	0	1	0	0	0
10/20/2017	4620	70	86	2	2	9	1	3	0	0	1	0	1	0
10/27/2017	7260	110	80	3	8	10	1	3	0	0	1	0	1	3
11/3/2017	9900	150	60	5	14	17	3	3	3	0	1	0	1	4
11/9/2017	12210	185	60	7	17	19	15	7	7	0	1	0	2	4
11/16/2017	14850	225	50	8	18	21	19	12	7	0	1	0	2	6
11/30/2017	18150	275	32	11	19	22	20	15	10	6	5	2	2	6
12/7/2017	20790	315	28	11	25	22	20	17	10	6	5	2	2	6
12/15/2017	23298	353	18	12	25	23	21	17	13	6	5	2	2	6
12/22/2017	25608	388	11	12	25	23	24	17	14	6	5	2	2	6
1/12/2018	29370	445	8	13	25	29	24	17	14	6	8	3	3	6

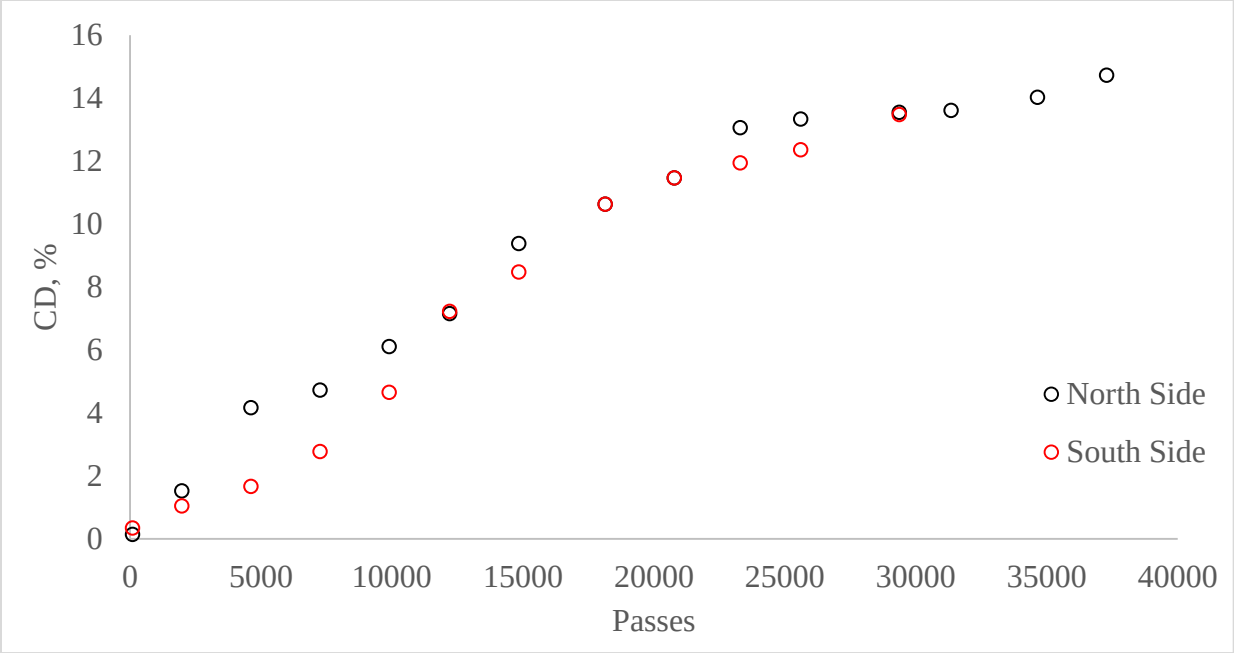

Figure 22. Development of CD on the North and South Test Item

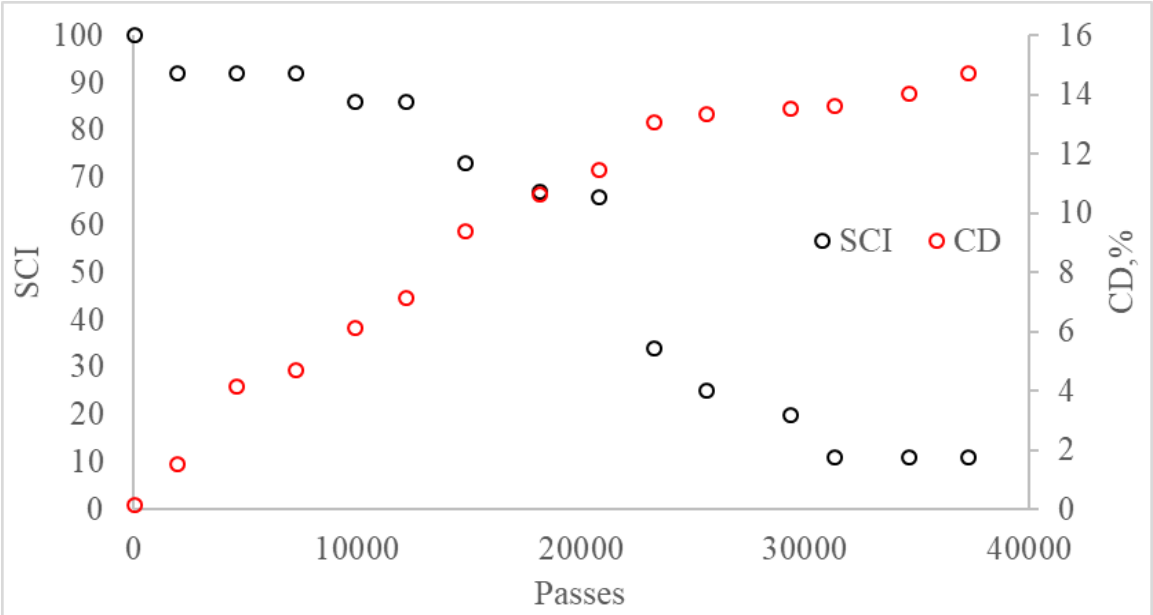

(a)

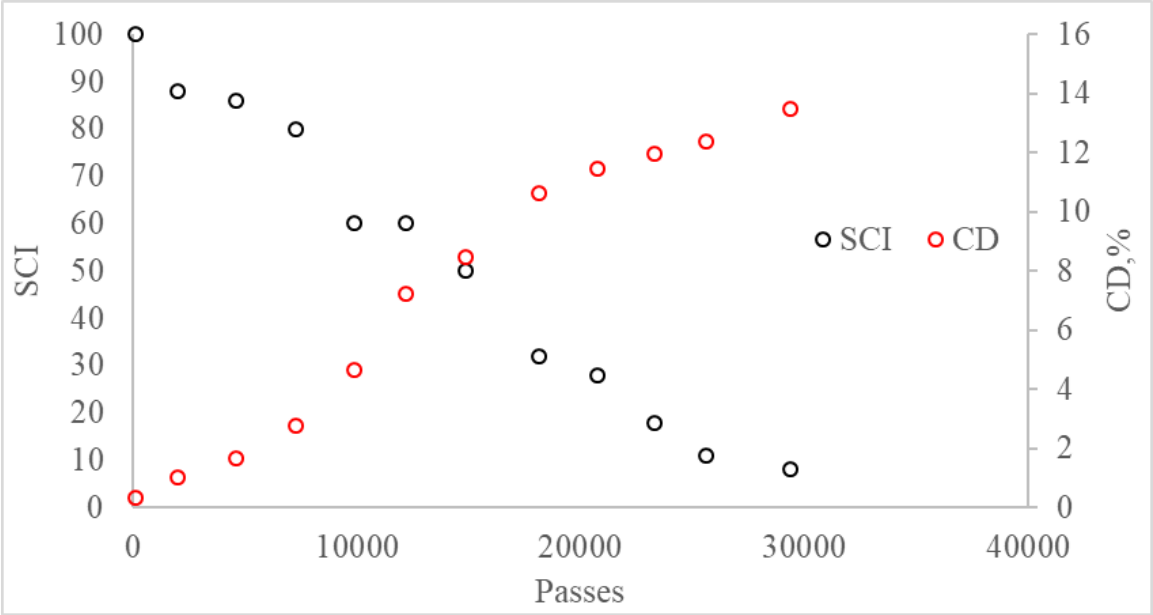

(b)

Figure 23. Comparison between SCI and CD: (a) North; (b) South

Correlation between Strain Responses and Local Distresses

The maximum strain responses from multiple sensors showed significant changes during the traffic test. Figure 24 shows sharp drops in the responses of EG-S-O-II-7 and EG-S-O-II-8 took place during the third day of trafficking. On the same day, the occurrence of a corner break was reported in the distress survey (Figure 25). The changes in EG responses allow for a more accurate estimate of both the crack initiation time and, potentially, the time of completion for crack propagation to the bottom of the slab in the case of a top-down crack.

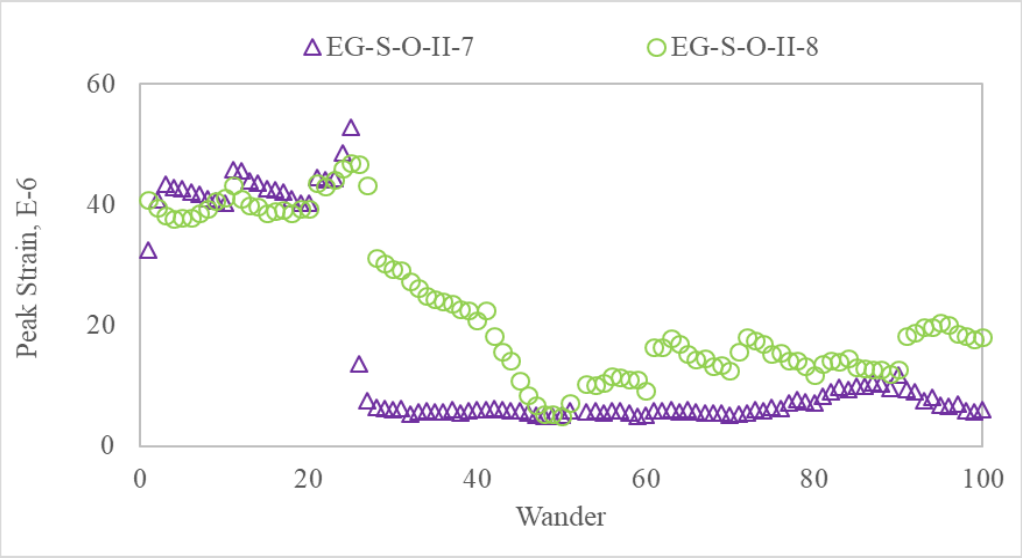

Figure 24. Peak Strains for EG-S-O-II-7 and EG-S-O-II-8

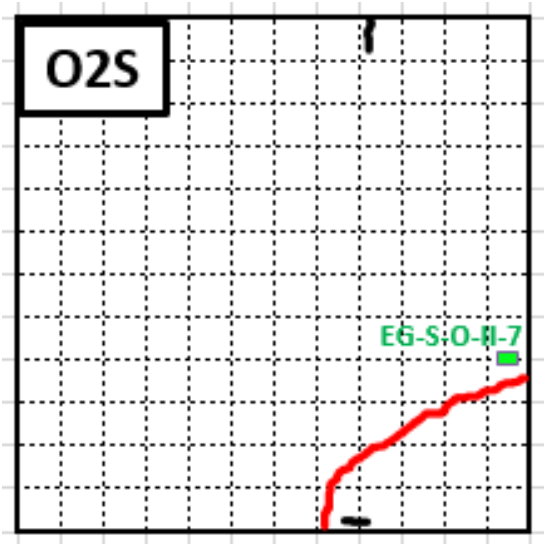

Figure 25. Corner Break Observed on Slab O2S during the 3rd Day of Traffic Test (Wander 21 to 30)

Given that the original CD value was estimated for the entire slab, its ability to capture and reflect the effect of localized distress became limited. Figure 26 shows that the strain responses of EG-S-O-II-9 in slab O9S increased from 16 to 30 microstrain, which may be an indication of crack development or local damage near the embedded sensor. However, as shown in Figure 27, minimum surface cracking was observed on slab O9S whereas significant cracking was observed on the adjacent slab O4S. A localized crack density (LCD) parameter was introduced as illustrated in Figure 27. The LCD was calculated as the percent of discrete units where cracking was observed within a virtual 12×12 ft. slab centered on the sensor of interest.

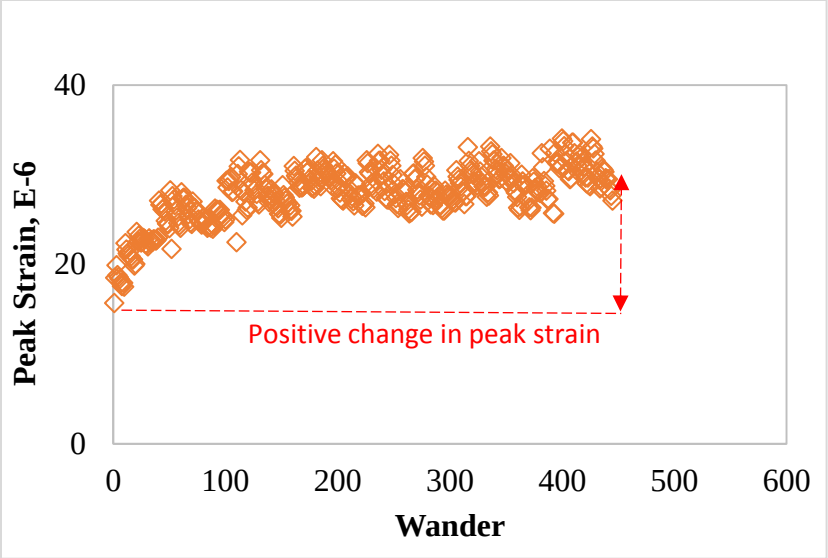

Figure 26. Peak Strain Change of EG-S-O-II-9 Due to Trafficking

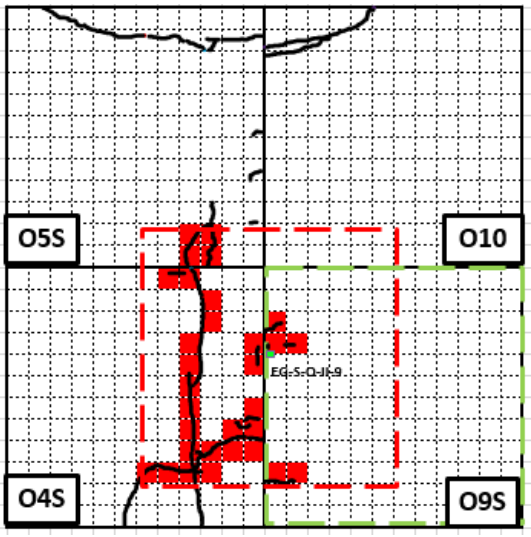

Figure 27. CD (green) vs. LCD (red) on Distress Map

Figure 28 shows the correlation between LCD and peak strain change for all the EGs. The change in peak strains increased with increasing LCD. In Figure 29, the same data is segregated by both the EG location within the slab (Figure 29a) and EG orientation (Figure 29b). While a positive correlation between LCD and change in the peak strains was observed for both top and bottom sensors, the LCD was only affected by the peak strain change from transverse EGs.

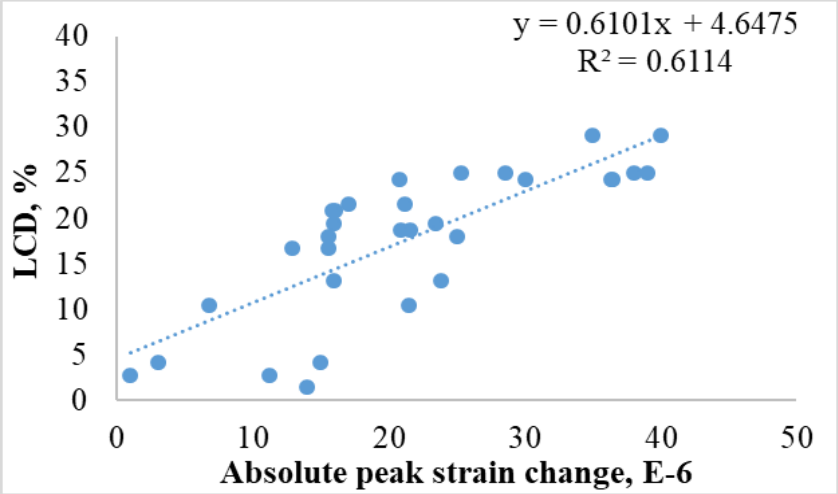

Figure 28. Correlation between LCD and Change in Overlay Peak Strains Considering a 12×12 ft. Virtual Slab

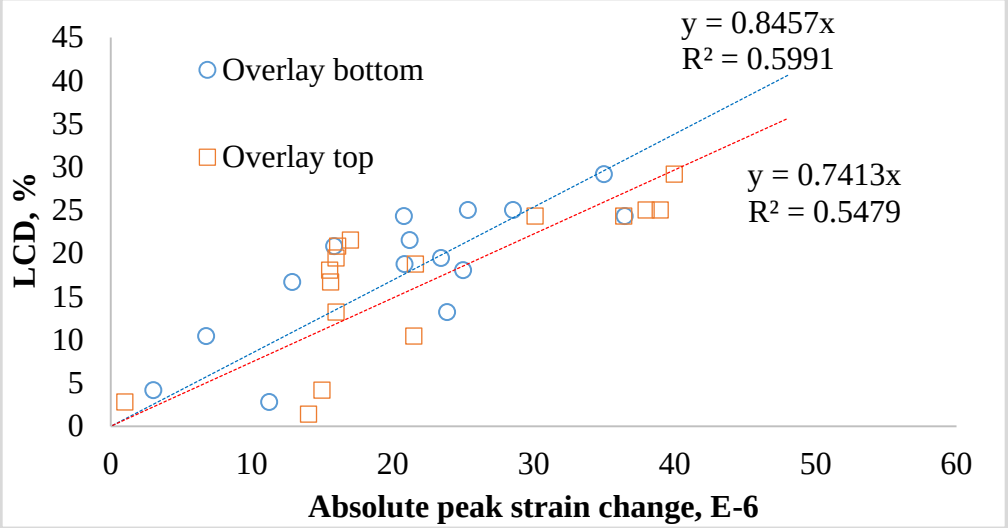

(a)

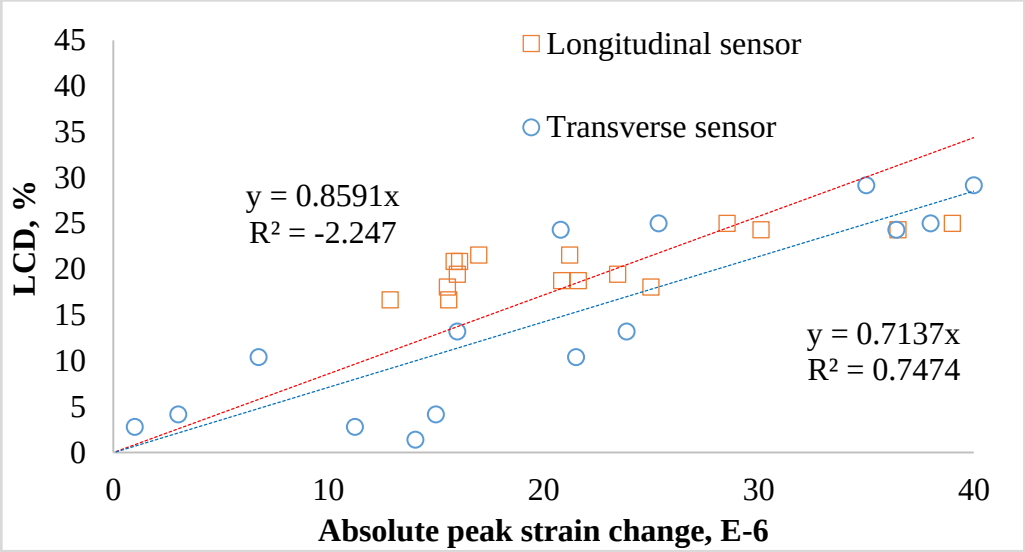

(b)

Figure 29. Correlation between LCD and Change in Peak Strain Considering a 12×12 ft. Virtual Slab: (a) Top vs. Bottom EGs, (b) Longitudinal vs. Transverse EGs

T/C Ratio (Tensile/Compressive Strain Ratio)

The relative change in peak tensile and compressive strains was evaluated by the T/C ratio. The T/C was defined as the ratio of peak tensile to peak compressive strain recorded by the same EG when the vehicle traveled over the critical track. An example of peak responses from transverse-top sensor EG-N-O-II-1 on Track 2 is shown in Figure 30.

Table 10 shows the median T/C ratio for the sensors at different locations in the overlay. The initial and final T/C ratios corresponded to the first and last wander, respectively. In general, the peak tensile strains were much higher than the peak compressive strains. The T/C ratio for the top sensors tended to increase over the course of traffic test, whereas the ratio for the bottom sensors decreased. This observation suggests increasing tensile stresses at the pavement surface and therefore potential dominance of top-down cracking.

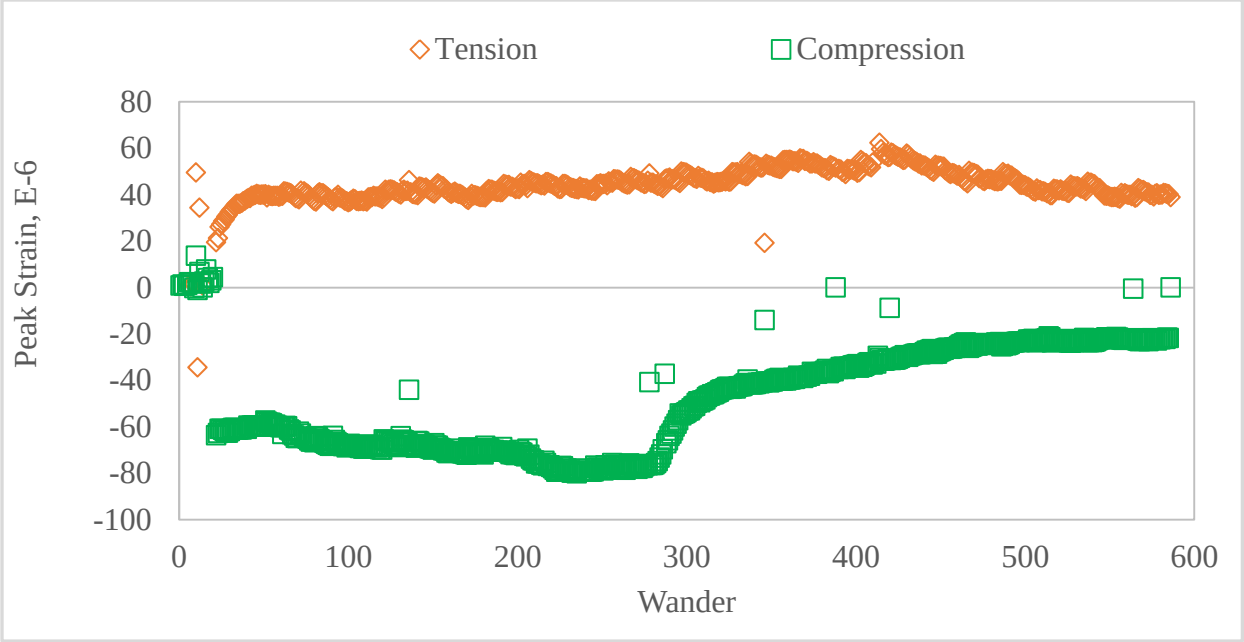

Figure 30. Peak compressive and tensile strain from EG-N-O-II-1 recorded at Track 2

Table 10. Median T/C Ratio for Sensors at Different Locations in Overlay

Sensor location	Initial T/C ratio	Final T/C ratio	T/C ratio change
Top	1.0	1.8	0.3
Bottom	4.1	2.2	-1.4

NAP (Neutral axis position)

The possibility of neutral axis shifting was evaluated. The neutral axis position NAP relative to the bottom of the slab was computed based on both the compressive and tensile strains, and their distance from the neutral axis. The maximum compressive strain of the top-longitudinal sensor EG-N-II-9 is on Track -1. In this case, the maximum tensile strain of sensor EG-N-II-10 (installed near the bottom of the overlay below EG-N-II-9) corresponding to Track -1, should also be considered for NAP estimates. Figure 31 shows EG-N-II-9 and EG-N-II-10 maximum compressive and tensile responses, respectively. The responses shown in Figure 31 shall be used in estimating the NAP.

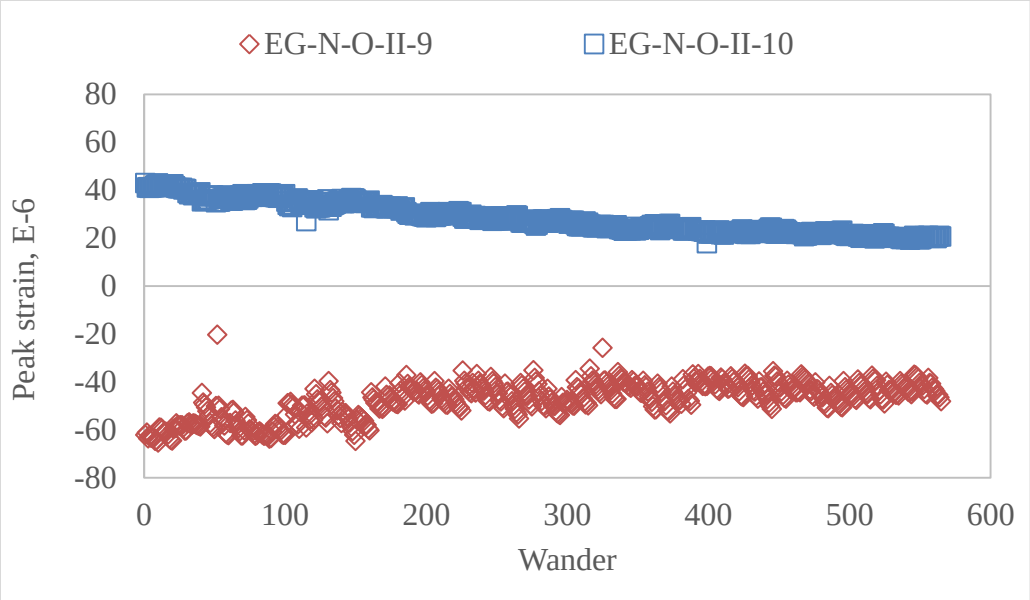

Figure 31. Strain Responses from Sensor Pair EG-N-O-II-9 and EG-N-O-II-10

The calculated initial and final NAP for all EG pairs (top and bottom) in the overlay are shown in Figures 32 and 33, respectively. Figure 32 shows that the initial NAP ranged from 2.1 to 4.9 inches, while the final NAP ranged from 1.6 to 5.7 inches. Note in Figure 33 that only one NAP estimate (marked in blue) is greater than 5 inches, whereas the rest EG pairs showed NAP values smaller than 4 inches (marked in red). As the mid depth of overlay slab is 4.5 inches, the significantly lower NAP values were most likely caused by the asphalt interlayer.

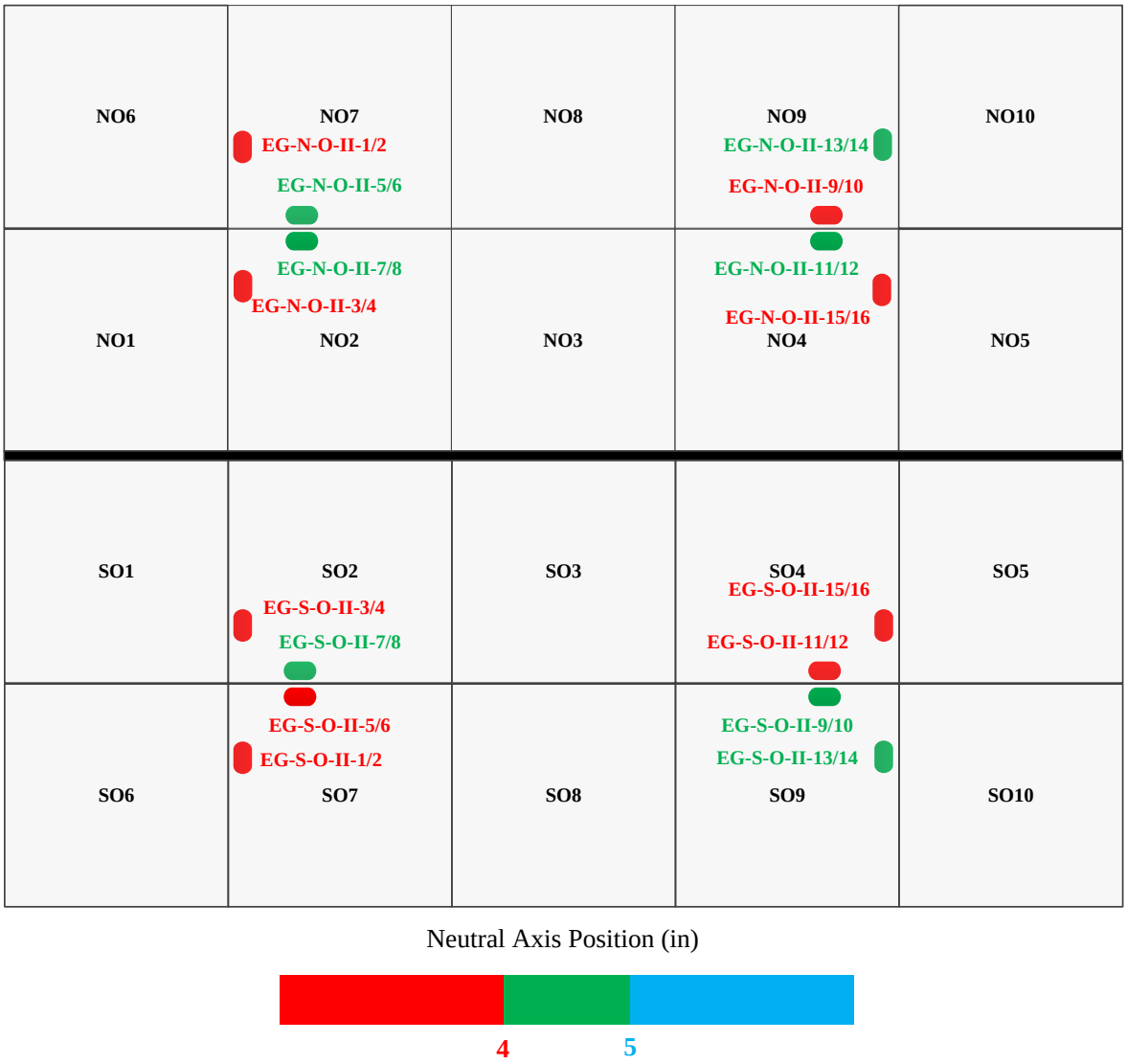

Figure 32. Distribution of Initial NAP Estimates

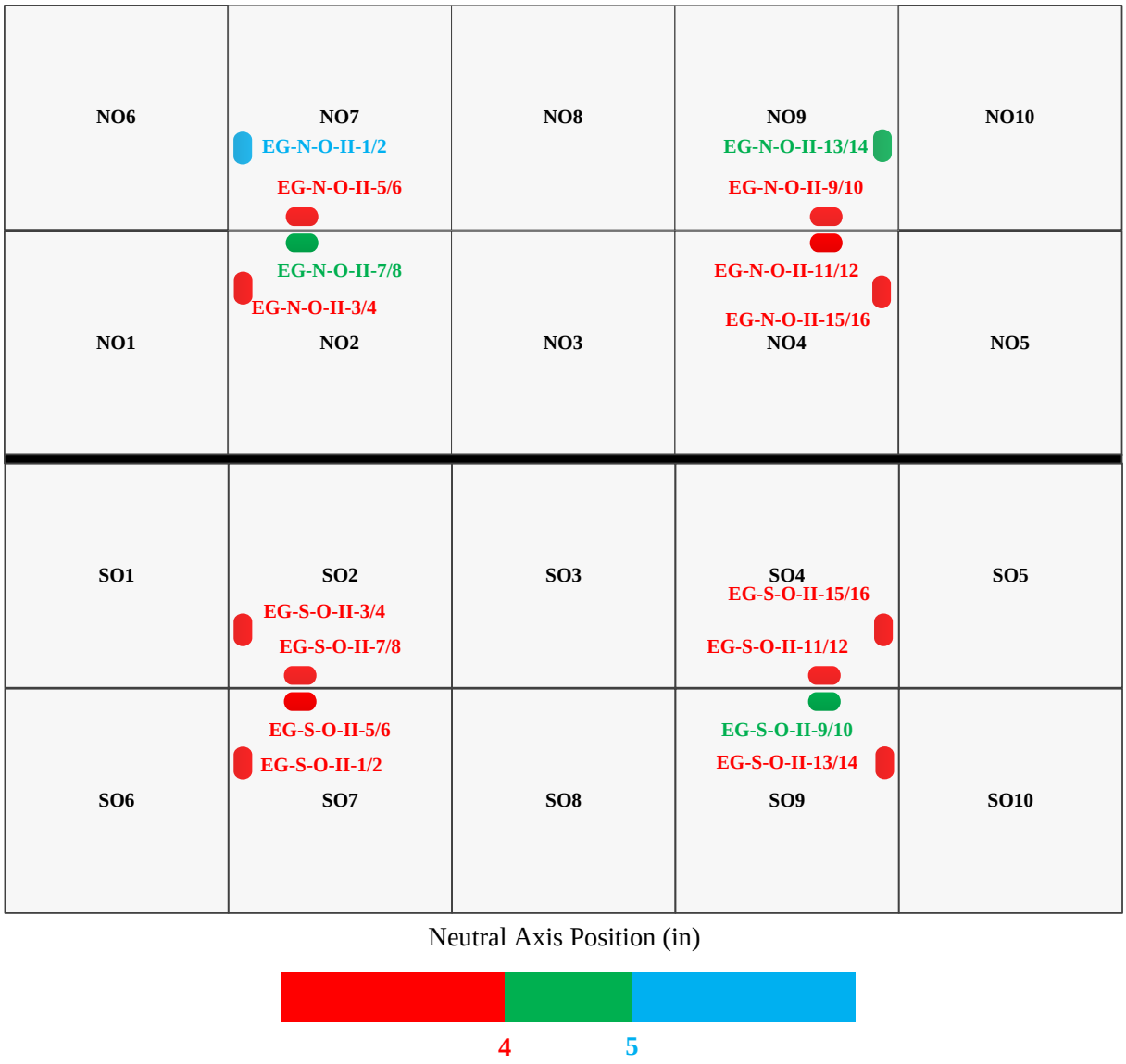

Figure 33. Distribution of Final NAP Estimates

For illustrative purposes, Figure 34 shows the maximum strain responses of two EG pairs (top and bottom) on the south side overlay and underlay, respectively. The estimated NAP in both cases was found to be located below the slab mid-depth. Although relatively close, the position of overlay EGs on the horizontal plane relative to the underlay EGs is not the same. However, it is expected that plotting both paired responses together would provide a fair representation of the state of stress in the concrete layers. Similar charts generated for other pairs of EGs, can be found in Appendix D.

In general, the initial overlay NAP (first wander) was observed to be slightly below the mid-depth, suggesting a possible bonded condition between the asphalt interlayer and overlay. As

expected for unbonded PCC overlays, a strain reversal was observed at the interface above and beneath the interlayer. The effect of traffic induced damage in the overlay was reflected not only by the NAP downward shifting but also by the reduction in strain response (last wander) captured by both top and bottom EGs.

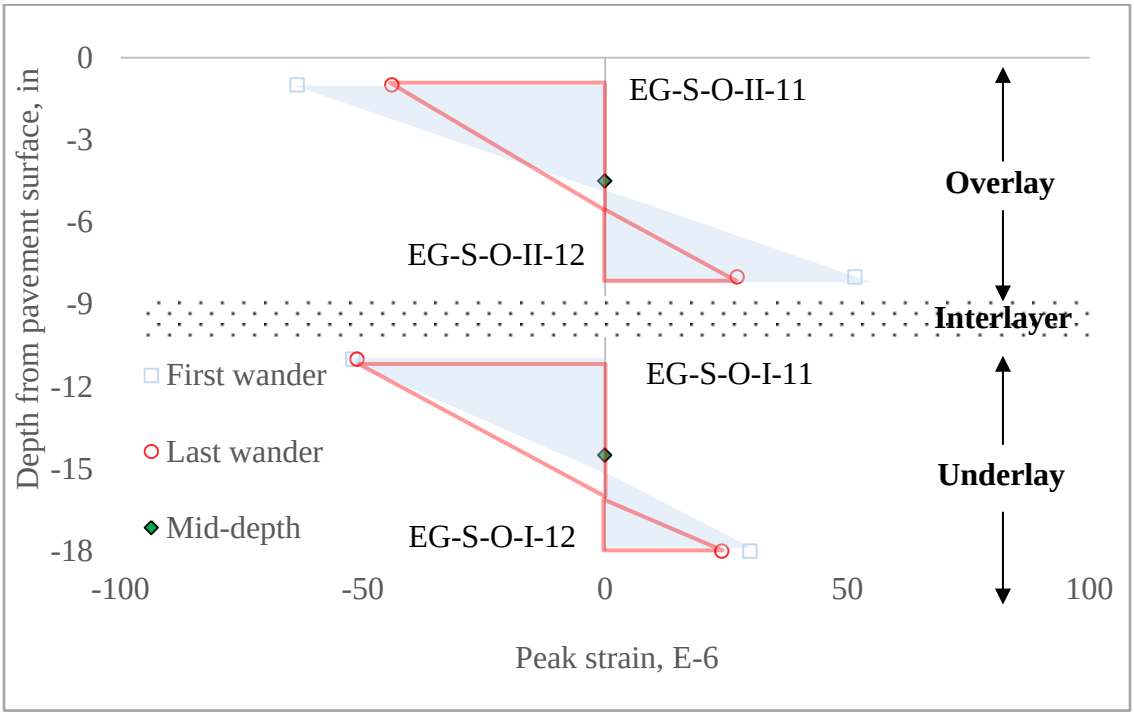

Figure 34. Example of NAP Downward Translation Captured by Overlay (EG-S-O-II-11, EG-S-O-II-12) and Underlay (EG-S-O-I-11, EG-S-O-I-12) Strain Gages

6.1.3 EDDY CURRENT SENSOR DATA (ECS)

6.1.3.1 CRITICAL TRACK VERIFICATION

The typical response of the ECS was monitored during the first ten wanders of the traffic test. In Table 11, the critical track corresponding to the maximum deflection observed for each ECS is summarized. As anticipated, the critical deflection response in the ECSs was observed when the outer wheel in either carriage passed directly over the sensor. Once the critical tracks were identified, monitoring and analysis of ECS data continued ignoring all other tracks.

Table 11. Eddy Current Sensor Critical Track

Sensor ID	Critical Track	Offset[1] (ft.)
ECS-N-O-II-1	-1	-0.1
ECS-N-O-II-2	0	0.3
ECS-N-O-II-3	-1	-0.1
ECS-N-O-II-4	0	0.3
ECS-S-O-II-1	1	-0.1
ECS-S-O-II-2	0	0.3
ECS-S-O-II-3	1	-0.1
ECS-S-O-II-4	0	0.3

[1] *Distance from the gage position to the closest wheel for the indicated Critical track*

6.1.3.2 ANALYSIS

Correlation between Deflection Responses and Local Distresses

The response captured by the ECS corresponds to the separation between two concrete layers. Most ECSs showed nearly constant responses of negligible magnitude (i.e., less than 5 mil) throughout the course of the traffic test. However, the maximum deflections observed for ECS-N-O-II-2 and ECS-S-O-II-1 ranged between 10 and 20 mils, and the response of these two ECS were found to correlate with the occurrence of distresses within the sensor vicinity. In Figure 35, the maximum deflection of ECS-N-O-II-2 is initially observed to become more negative (i.e., increasing absolute deflection). Beyond wander 195 the trend reverted so that the maximum deflection became less negative (i.e., decreasing absolute deflection) with additional trafficking. This inflection point is consistent with the occurrence of a longitudinal crack (see red marked crack in Figure 36), which took place between wanders 195 and 205.

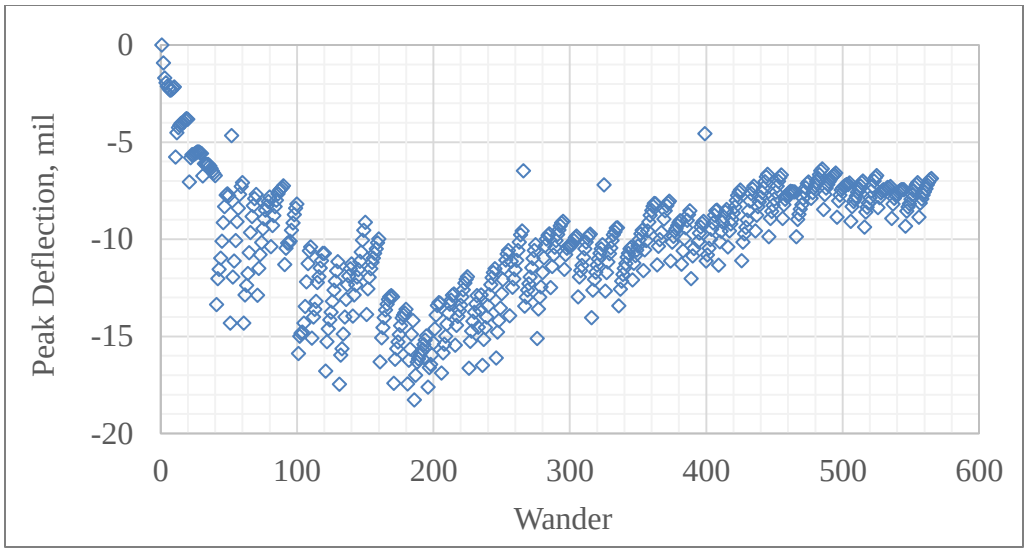

Figure 35. Change in ECS-N-O-II-2 Maximum Response with Traffic for the Critical Track

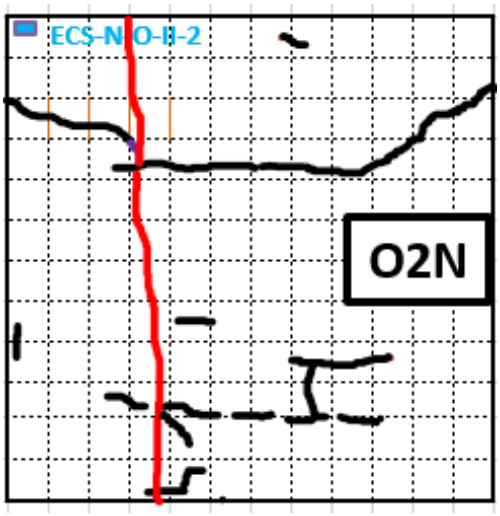

Figure 36. Longitudinal Crack Captured by ECS-N-O-II-2 Response

Figure 37 shows the change in the maximum deflection response of ECS-S-O-II-1. Past wander 100, an increase in the rate of change in maximum deflection was observed. Between wander 255 and 265, the maximum deflection began to level off. This is consistent with the occurrence of the corner break shown in Figure 38, which took place within the same timeframe.

Figure 37. Change in ECS-S-O-II-1 Maximum Response with Traffic for the Critical Track

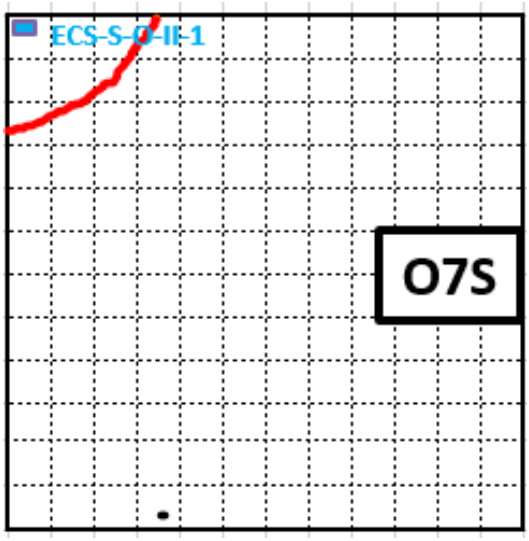

Figure 38. Corner Break Captured by ECS-S-O-II-1 Response

Effect of Pavement Temperature on ECS Response

Figure 39 captures pavement temperature effects on the response of ECS-S-O-II-1. The estimated temperature of the HMA interlayer (Section 6.1.1) was used in Figure 39. The traffic test normally started at 6:00AM and ended at 3:00PM. In the chart, every group of 10 consecutive data points showing an increasing trend correspond to the 10 traffic wanders applied to the pavement on a daily basis. The temperature usually increased over the course of the day,

which in turn was reflected on the increasing trend in peak deflections. Similar correspondence between daily temperature changes and maximum response was observed for EGs.

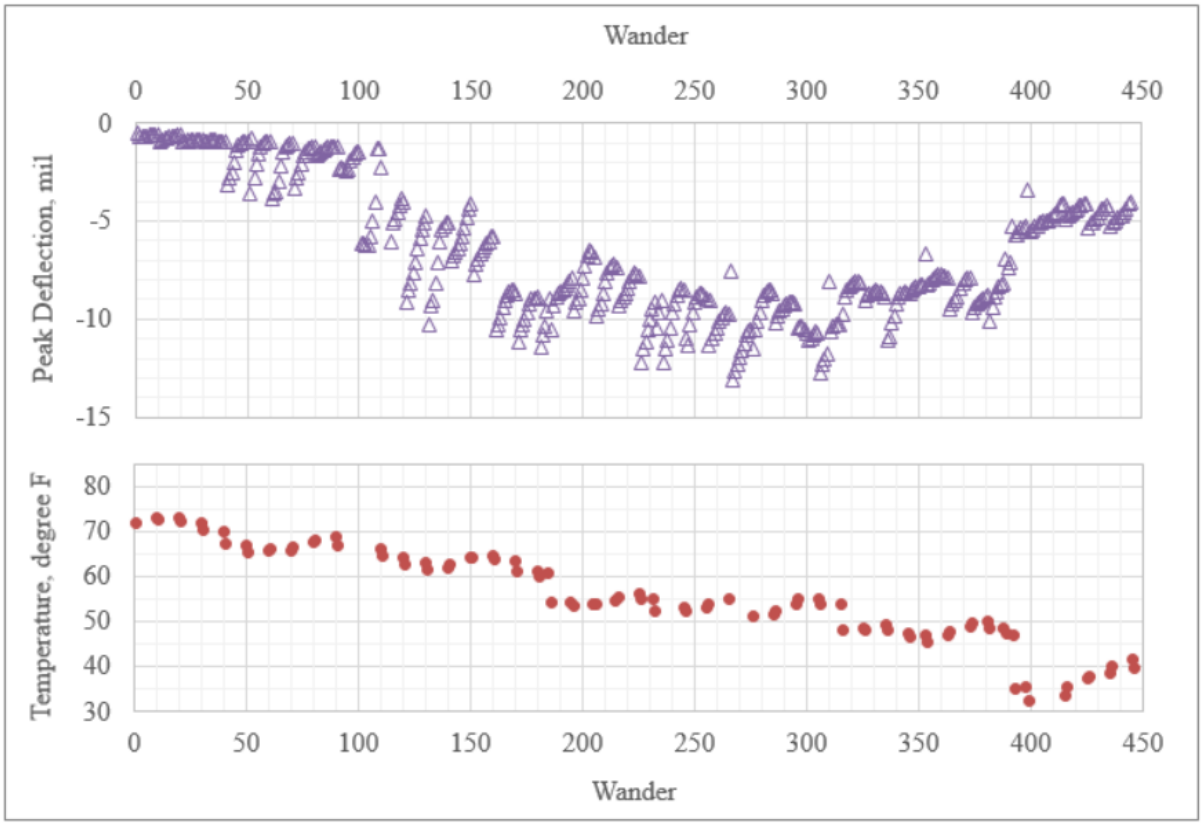

Figure 39. Pavement Temperature Effect on the Response of ECS-S-O-II-1

It was mentioned in the previous section that the increasing trend in the rate of change in maximum deflection for ECS-S-O-II-1leveled off with the occurrence of a nearby corner break. However, after approximately 490 wanders, there was a sharp drop in temperature corresponding to a traffic pause of one week. Along with the 10°F-drop in temperature, a sharp reduction in the measured peak deflection was observed. In general, although of a second order, some evidence of temperature effects upon the ECS response was observed.

6.2 DEFLECTION DATA

6.2.1 DEFLECTION BASIN

Heavy Weight Deflectometer (HWD) testing was conducted prior to, during and after the traffic test. HWD test locations included all slab centers, selected corners, and the midpoint on slab edges along the transverse joints; as indicated by the blue dots in Figure 40. HWD testing was conducted using a KUAB Model 150 tester with a four-drop loading sequence beginning with an approximate 36,000-pound seating load. The subsequent loads were approximately 12,000

pounds, 24,000 pounds, and 36,000 pounds. At each load level, surface deflections were measured using a total of eight geophones spaced at a regular interval of 12 inches. The positions of these geophones are -12, 0, 12, 24, 36, 48, 60, and 72 inches, respectively. The first position (i.e., -12) corresponds to 12 inches front from the center of the loading plate. Raw deflection data were first normalized by adjusting deflections to a standard load (i.e., 12,000, 24,000, and 36,000 pounds).

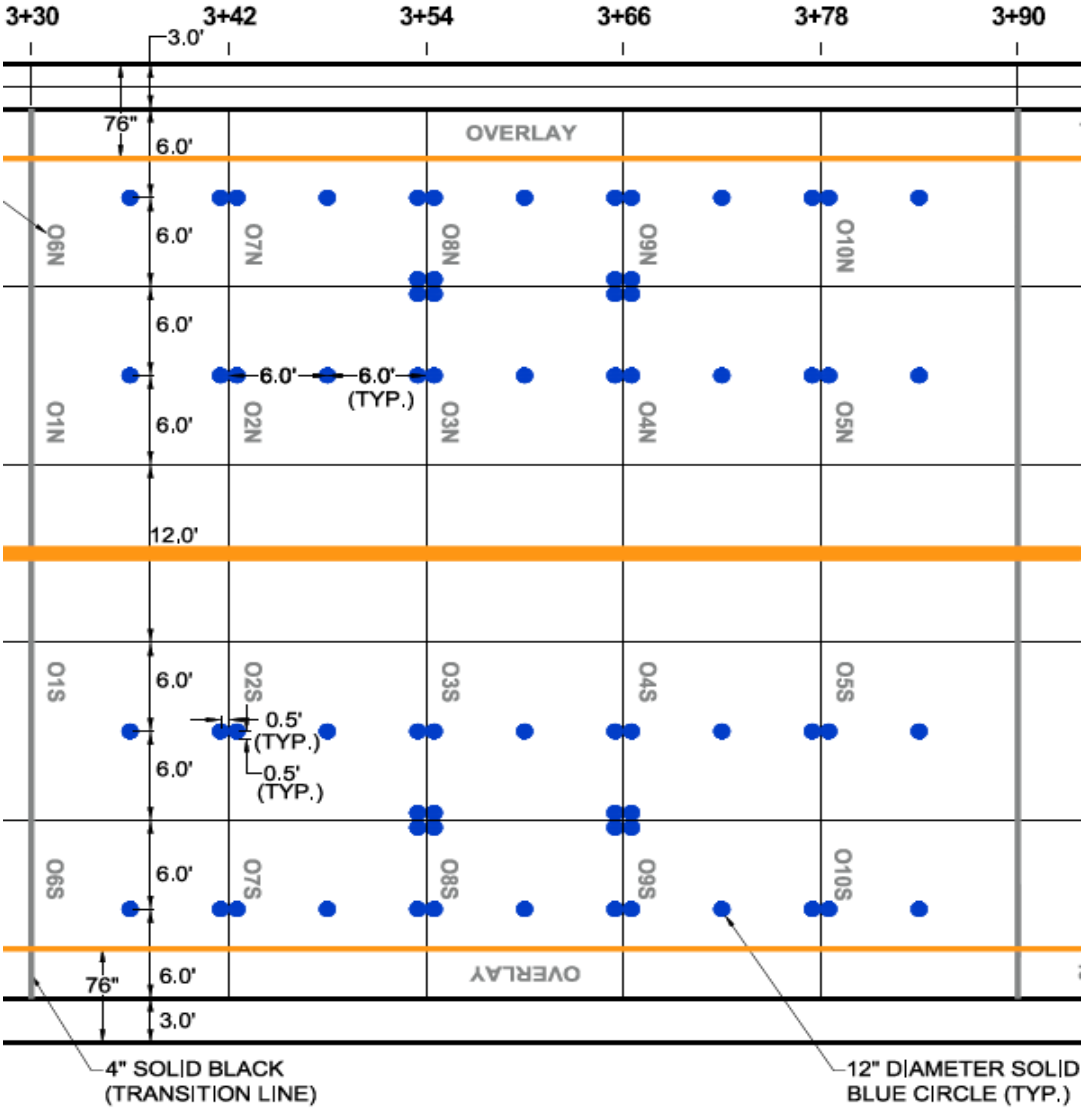

Figure 40. HWD Testing Locations

Deflection basins measured at the slab centers corresponding to 36,000 pounds are plotted in Figures 41 and 42 for the north and south test item, respectively. On the north test item (see Figure 41), notable changes in the deflection basin over the course of trafficking were observed in slabs O1N through O5N. In these slabs, deflections gradually increased with respect to the baseline. This indicates that the overall strength of the pavement system deteriorated with

traffic. On slabs O1N and O3N, an increase in deflections was noticed at the geophone located 72 inches from the center of the loading plate. This suggests that some of the damage accumulated in deeper layers during the traffic test. In general, no significant variations in the deflection basin were observed for slabs O6N through O10N. However, some changes were recorded by the geophones at 48 and 60 inches in slabs O7N and O9N. This indicates the possibility of isolated damage in supporting layers. As expected, the outer slabs O6N through O10N did not exhibit significant deterioration.

Figure 42 shows the deflection basins for slabs on the south test item. Again, no significant variation in deflection basins were observed on the outer slabs (i.e., O6S through O10S) compared to those in the inner lane (i.e., O1S through O5S) which received most of the traffic. Deflection on inner slabs increased over the course of traffic. Slab O5S presented the least variation in the deflection basin over time, and showed the least amount of distresses as reflected by the crack density parameter (see Table 9). Conversely, slab O1S showed the most significant changes in the deflection basin starting on 11/30/2017. Such changes reflected the severe deterioration underwent by slab O1S within the same period: occurrence of a diagonal crack across the slab center and subsequent shattering after 11/30/2017 (see distress survey log in Appendix C).

6.2.2 IMPACT STIFFNESS MODULUS (ISM)

Impact Stiffness Modulus (ISM) was calculated from the ratio of HWD test load (P) and the maximum deflection (δ_{max}), i.e., deflection at the center of the loading plate, in response to a test load. The ISM was calculated for the maximum P at 36,000 pounds, using Equation 1:

$$ISM = \frac{P}{\delta_{max}} \quad \text{Eq. 1}$$

Prior to the calculation of ISM, load and deflection values were collected from the HWD tests conducted at the center of every slab on both the north and south side. Figures 43(a) and 43(b) show the ISM calculated from HWD tests conducted over the course of traffic test. On the south test item, traffic was stopped after 01/12/2018. Therefore, there was no ISM reported after that date. Additional analysis on ISM is elaborated later in this report.

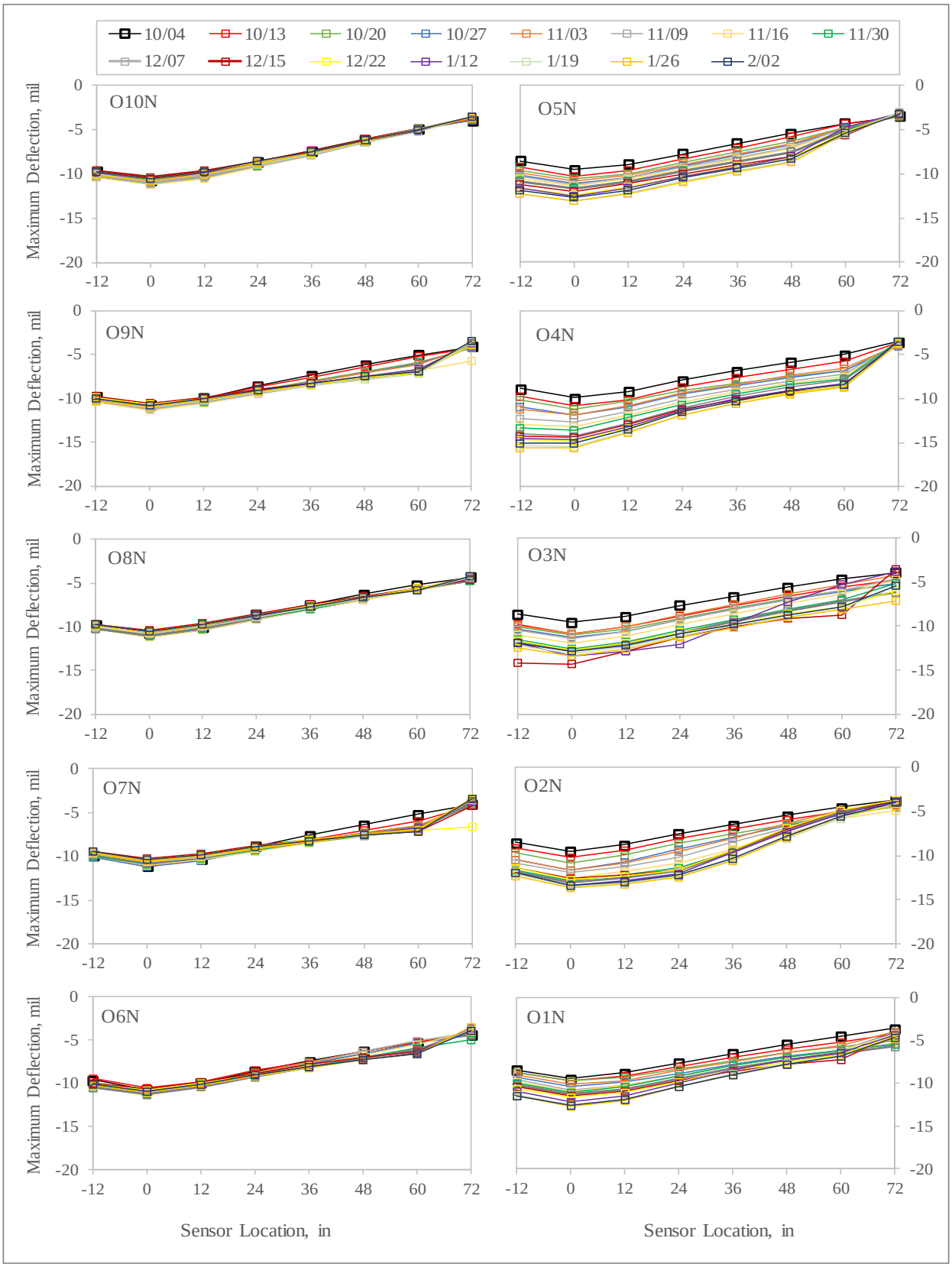

Figure 41. Slab Center Deflection Basins, North Test Item

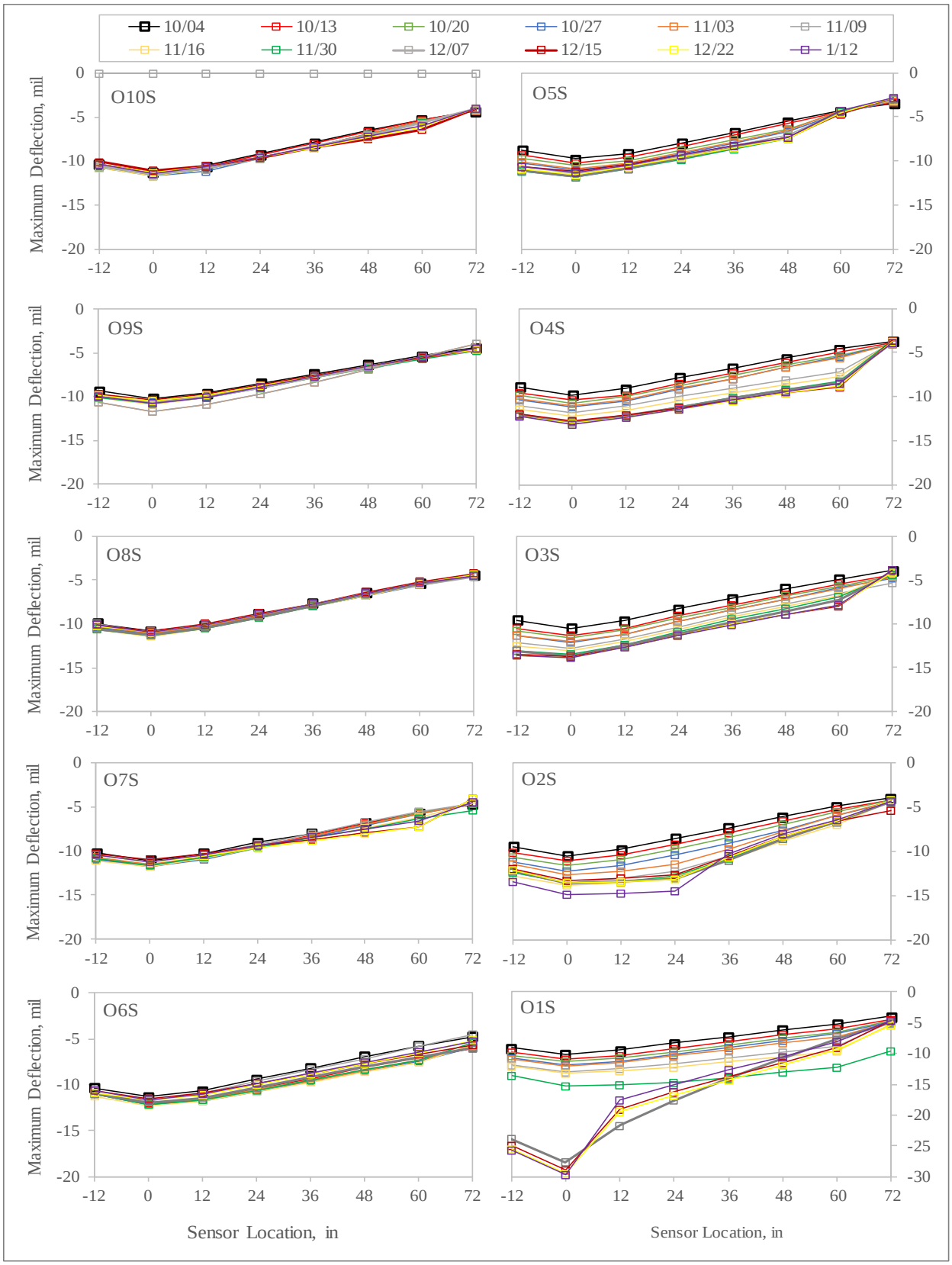

Figure 42. Slab Center Deflection Basins, South Test Item

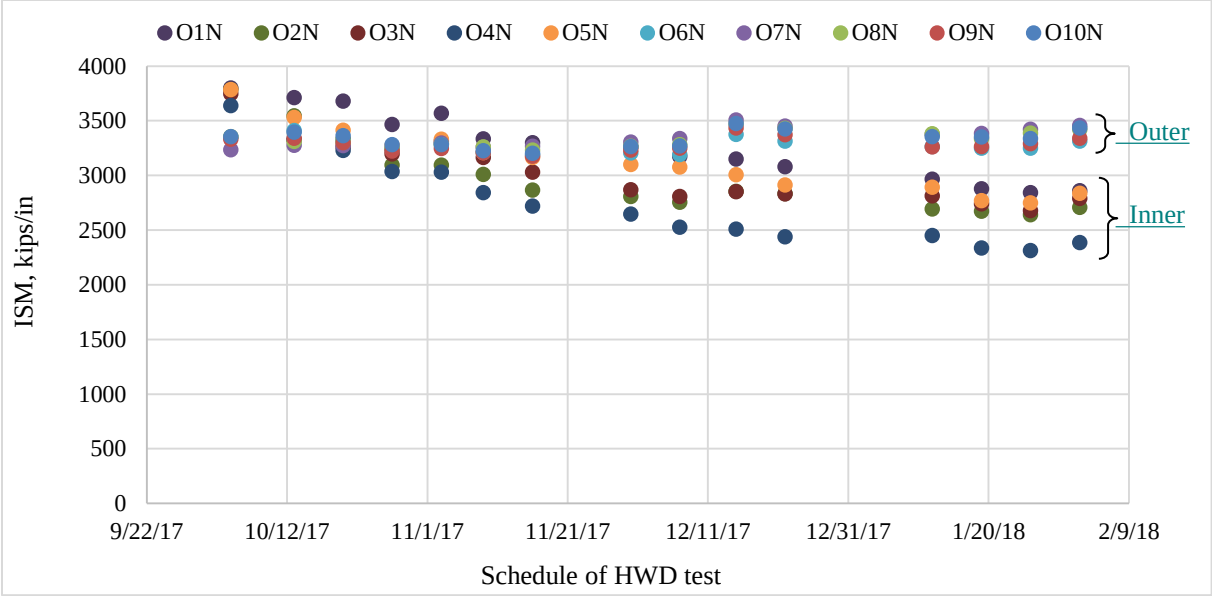

(a)

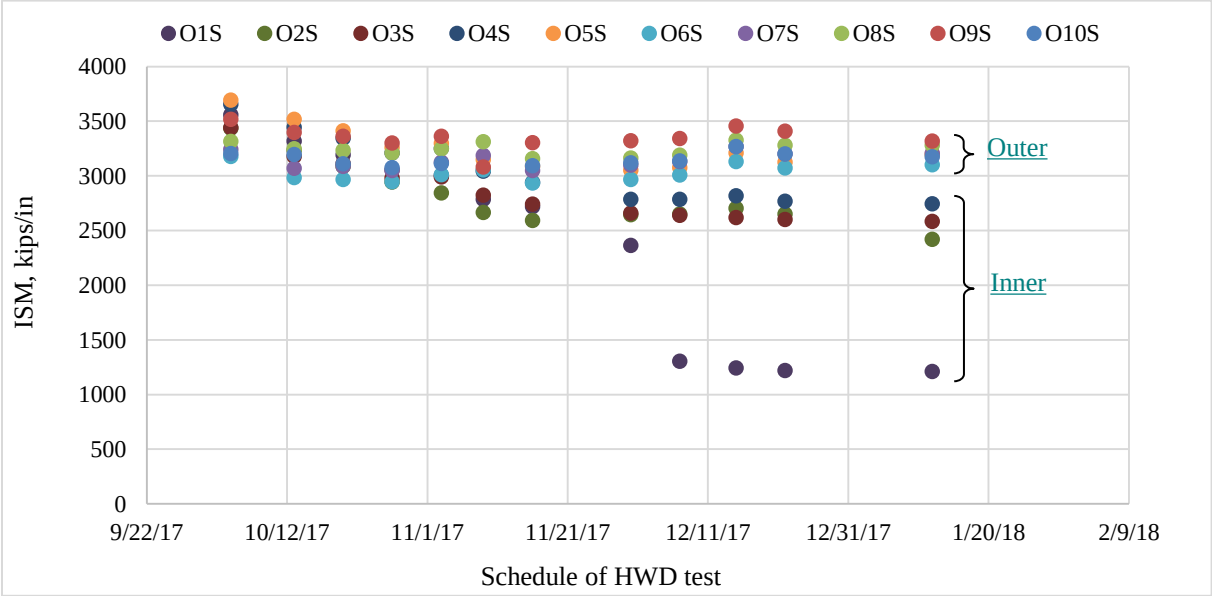

(b)

Figure 43. ISM on the Center of Slabs: (a) North Test Item, (b) South Test Item

7. ADVANCED ANALYSIS

7.1 FAILURE MECHANISM

In the following sections, four aspects of the pavement performance were investigated to attempt explaining the overlay failure mechanism: the distress pattern, slab corner deterioration, slab interior deterioration, and joint deterioration.

7.1.1 DISTRESS PATTERN

In the preliminary structural condition evaluation presented in Section 5.2, the test item trafficked with 4-wheel gear configuration failed first. In both the CC4 Baseline Experiment and SCI Validation Study, under constant wheel load the pavement deterioration of test items subjected to traffic with a 3D gear occurred at a higher rate than test items subjected to traffic with a 2D gear (*2,3*). However, the changes in SCI with traffic reported in CC8 showed the opposite trend. As-built properties were ruled out as source of premature deterioration in the south test item. In this section, an attempt is made to identify other possible sources of premature deterioration by analyzing the overlay distress pattern in detail.

In Figure 44, the changes in SCI with traffic for the north and south test item are presented with details on the occurrence of major distresses driving sharp drops in the SCI. Note in Figure 56 that on the south test item, the first corner break (CB #17) and second corner break (CB #45) appeared before completion of only 2000 and 6000 passes, respectively. Three additional corner breaks (CB# 101, CB #111, and CB #140) appeared later over the course of trafficking on the south test item. On the north test item, the first and only corner break (CB #89) appeared after approximately 14000 passes were applied to the overlay. This indicates possible underlaying conditions that made the south test item prone to early development of localized damage. The complete collection of distress maps and written logs of the surveys can be found in Appendix B and Appendix C, respectively. The potential for excessive slab corner movement as result of separation between the overlay and underlay is addressed in detail later in this report.

In Figures 45 to 49, a selection of distress maps obtained at different times over the course of traffic illustrate the observed distress pattern. The distress maps in Figures 45 and 46 capture the occurrence of CB #17 and CB #45 in the south test item, respectively. Note in Figure 46 that only random, tight and isolated interior surface cracks were observed on the north during the early stage of trafficking. The next sharp drop in SCI for the south test item is associated with the first shattered slab (SS #54) as indicated in Figure 44. This shattered slab was reported after the 12^{th} day of traffic test with 7920 total cumulative passes as shown by the distress map in Figure 47. As seen in Figure 47, slab O2S was shattered mainly by linear cracks that reflected from the underlying longitudinal joints of CC8 Phase I overlay. It is speculated that the early occurrence of CB #17 triggered reflective cracking in the south side. Figure 48 shows evidences that by the time CB #89 appeared in the north test item, reflective cracking from the underlaying pavement had spread over both test items. The difference between the north and south test item SCI began to narrow down after 22770 vehicle passes with the occurrence of the first shattered slab SS#124 on the north side (Figure 44. The gap in SCI between test items keeps decreasing with additional passes until the final overlay condition illustrated in Figure 49 was achieved.

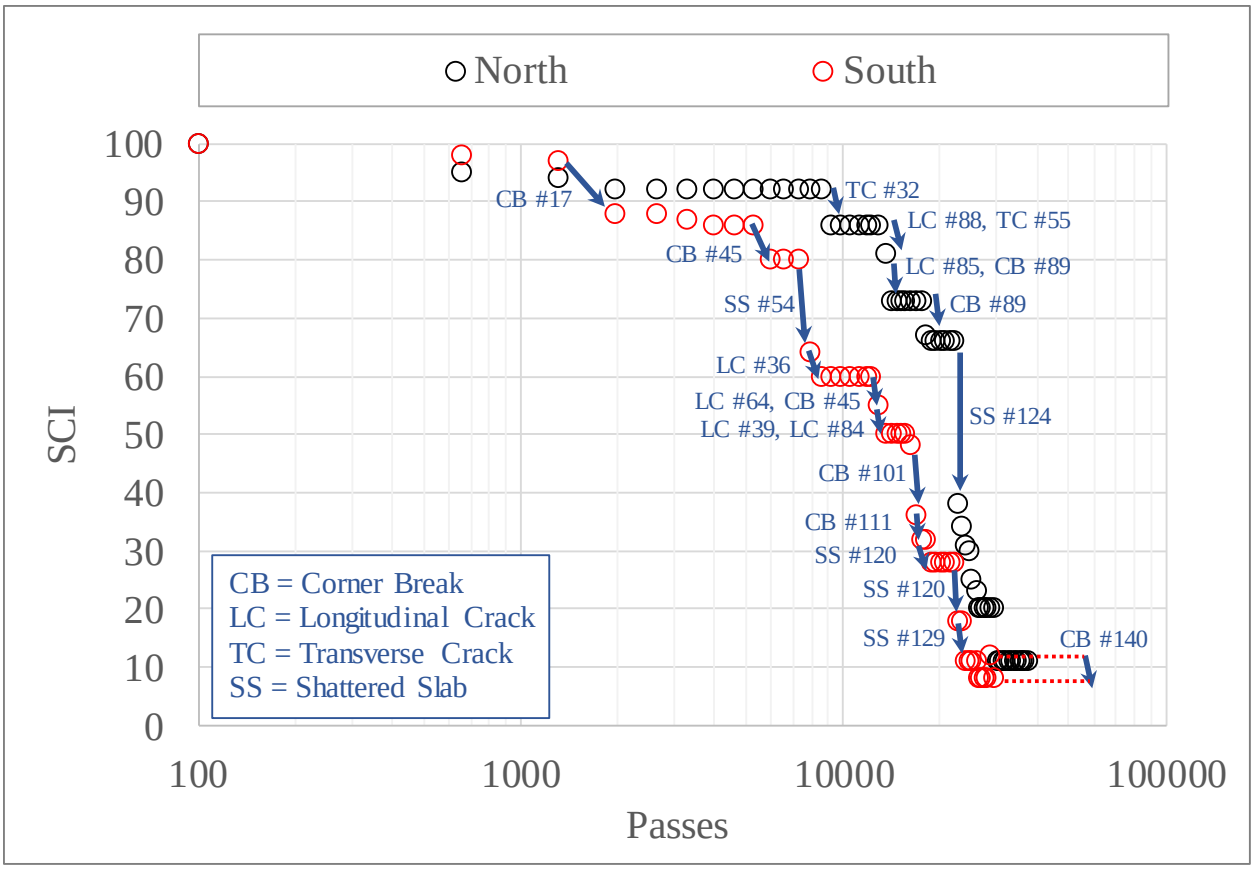

Figure 44. Major Distresses Driving Sharp Drops in the Overlay SCI

In general, corner breaks and longitudinal cracks were the dominant overlay distresses. A total of five corner breaks were reported in the south side whereas only one was reported in the north. The initial underlay SCI value for south test item was 68 whereas for the north test item the SCI was 79. This supports the speculation of underlay damage with higher incidence on the south side, during the overlay traffic test. Premature deterioration of the overlay south test item may have reflected the underlay pattern of deterioration. It is expected that an assessment of the underlay final condition as part of the CC8 forensic investigation will provide additional elements to explain the observed distress pattern.

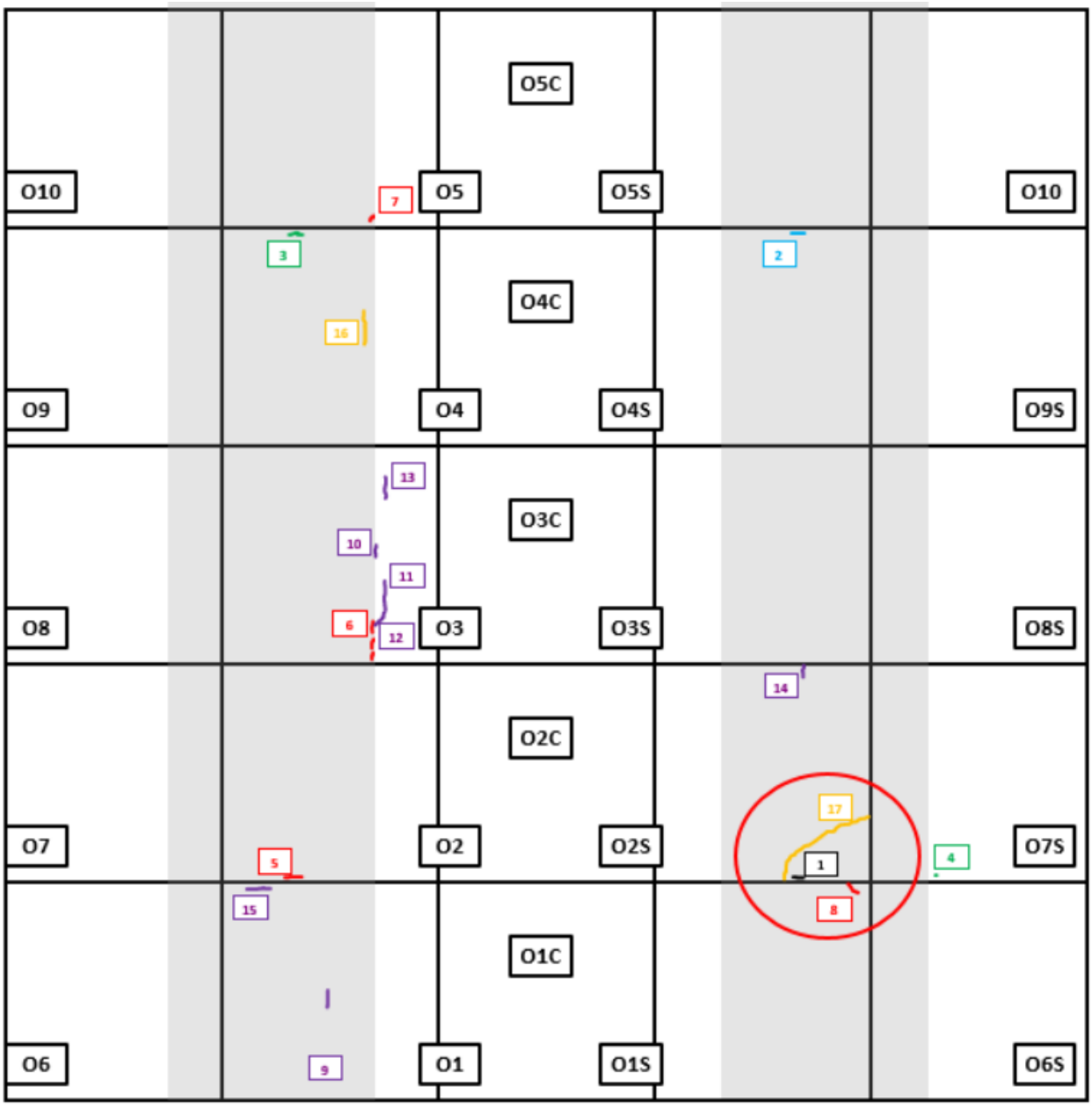

Figure 45. Distress Map - 3rd Day, 1980 Vehicle Passes

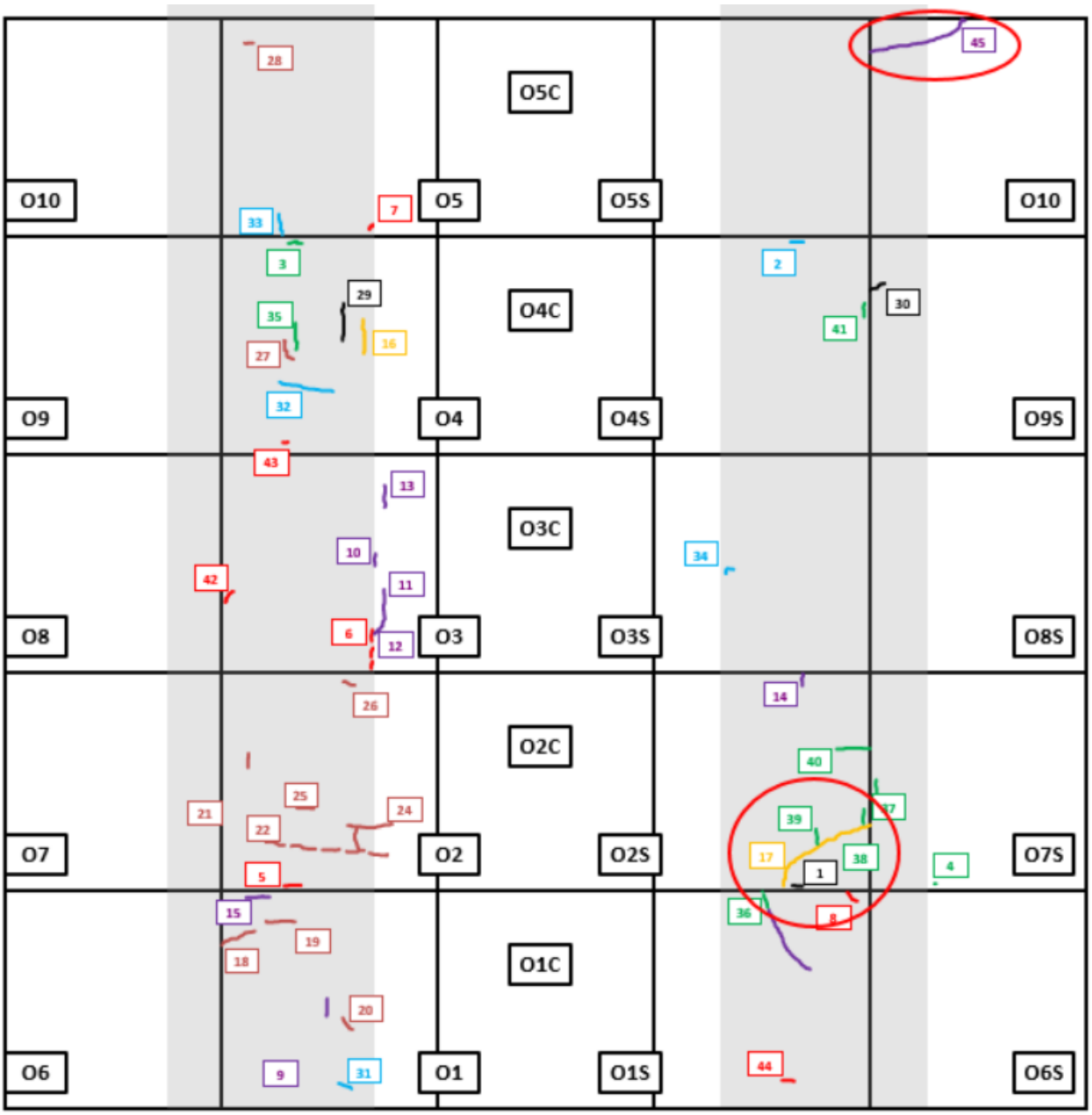

Figure 46. Distress Map – 9th Day, 5940 Vehicle Passes

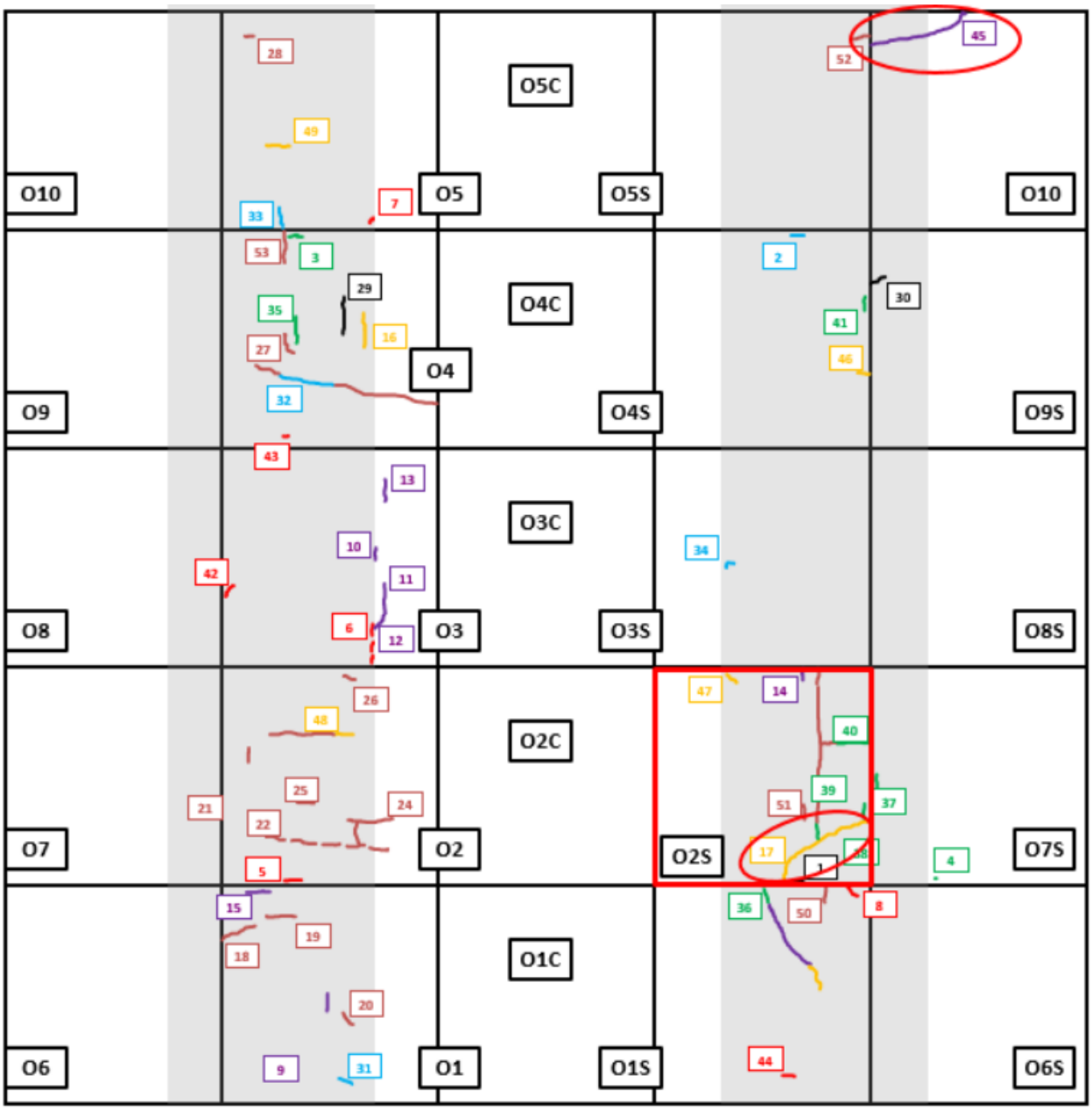

Figure 47. Distress Map – 12th Day, 7920 Vehicle Passes

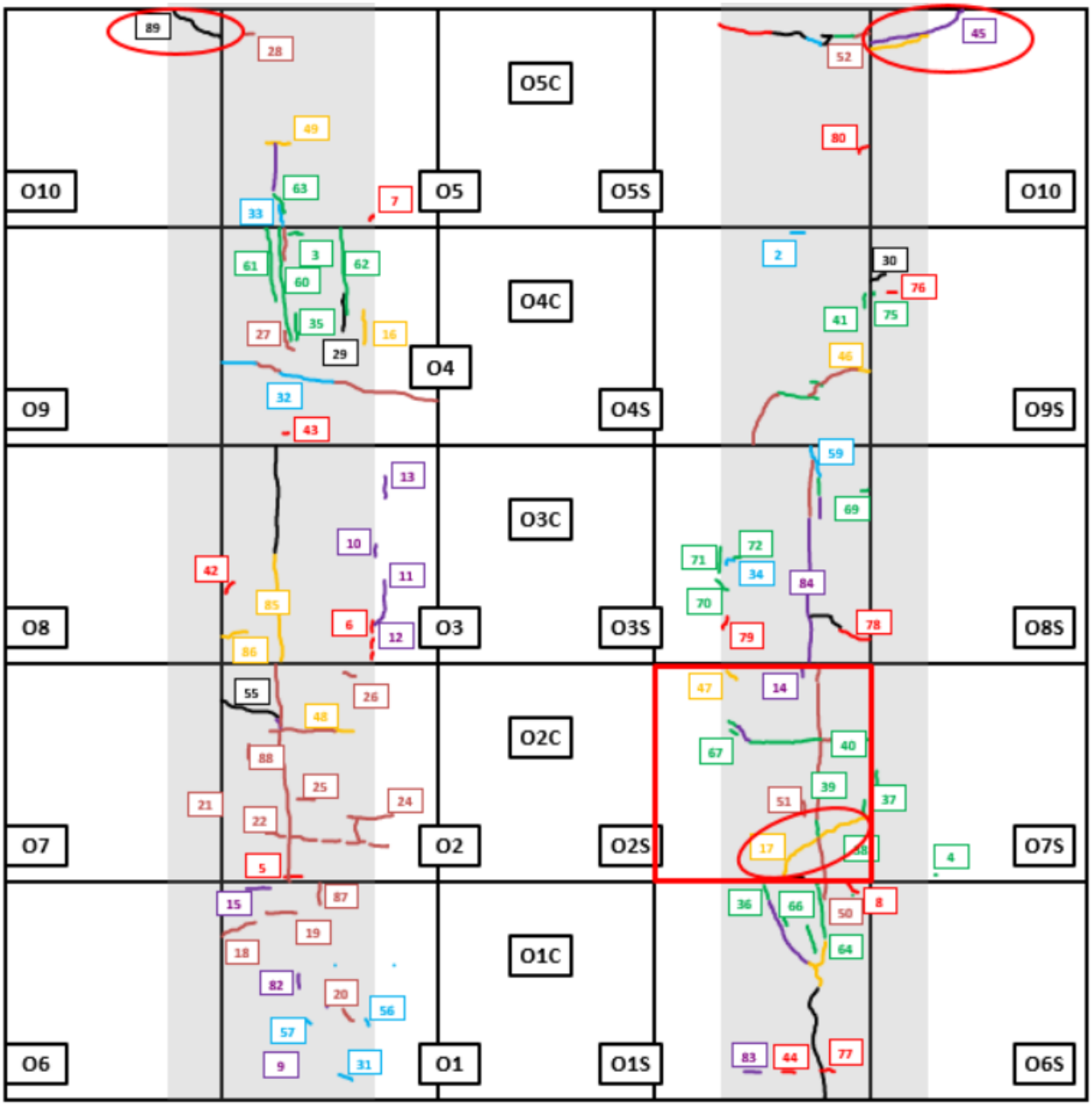

Figure 48. Distress Map – 22nd Day, 14190 Vehicle Passes

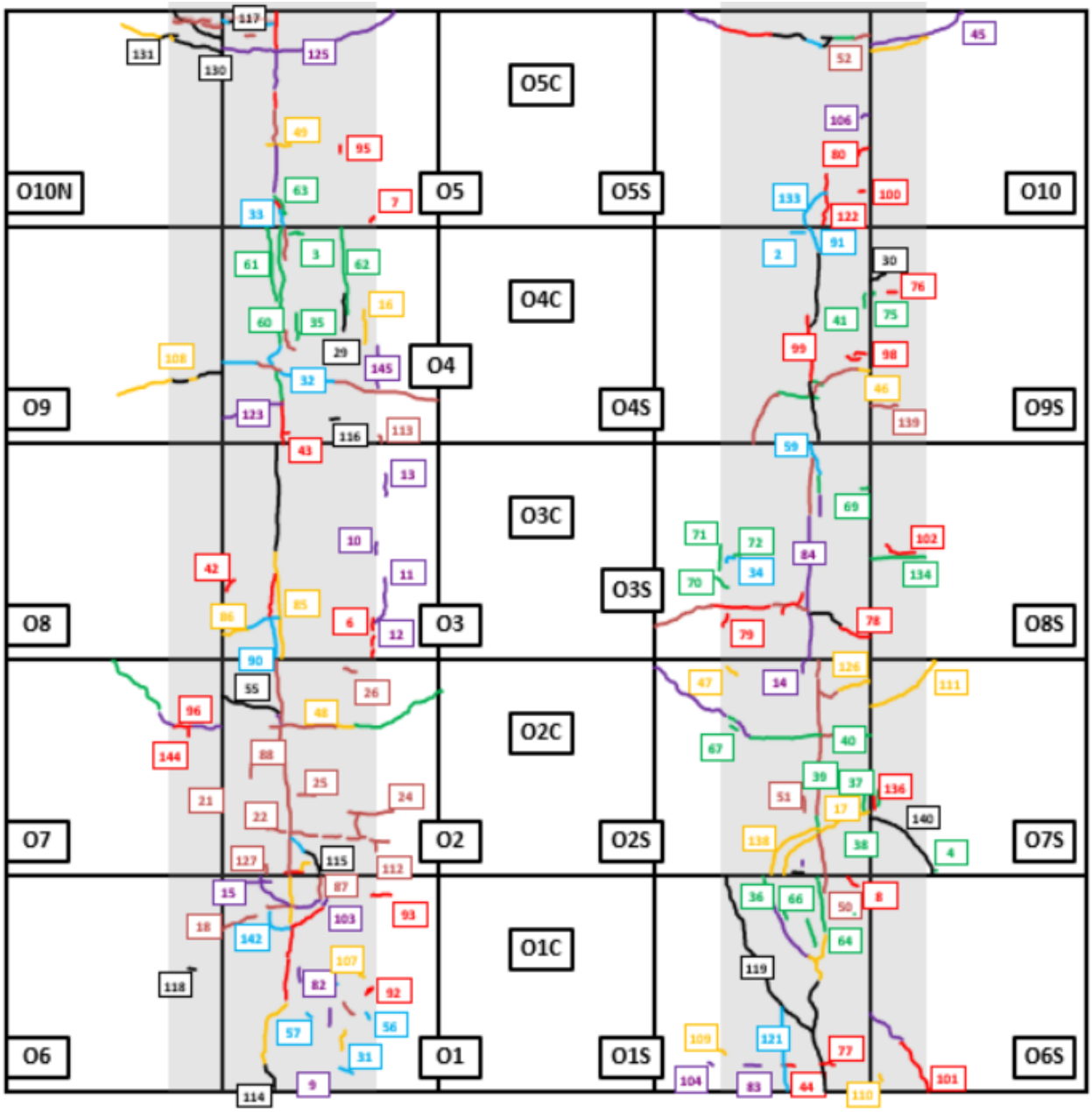

Figure 49. Distress Map – 60th Day, Vehicle Passes: 37290 (North) and 29370 (South)

7.1.2 CORNER DETERIORATION

In this section, corner deterioration was investigated by evaluating the corner-to-center deflection ratio; and conducting a void analysis.

Corner-to-Center Deflection Ratio

HWD tests were conducted at different locations within the slabs as illustrated in Figure 40. In certain slabs these locations include both the center and corner of the slab. Later, the corner-to-center deflection ratio corresponding to the heaviest load (i.e., 36,000 pounds) was calculated for selected locations of the slabs on both the north and south test item. In both test items, the corners were designated using three characters. The first two characters correspond to the slab number and test item side, and the last indicates the corner orientation (e.g., 2NE corresponds to the east corner of slab 2 in the north test item). On the north test item, the corners evaluated were: 2NE, 3NW, 3NE, 4NW, 7NE, 8NW, 8NE, and 9NW. On south test item, the following corners were included: 2SE, 3SW, 3SE, 4SW, 7SE, 8SW, 8SE, and 9SW. The corner-to-center deflection ratio was repeated for every weekly HWD testing to determine how the parameter changes over the course of trafficking.

Figure 50(a) and (b) show the variation of the corner-to-center deflection ratio over time in the north and south test items, respectively. During the baseline HWD testing, the corner-to-center deflection ratio ranged from 1.1 to 1.7. After the traffic test started on 10/10/2017, the corner-to-center deflection ratio showed an increase. The slabs along the outer lane (i.e.; slabs O6N through O10N) in the north test item consistently showed an increasing trend of the ratio. Along the inner lane (i.e., slabs O1N through O5N) the trend was inconsistent. As seen in Figure 50(a), corners 7NE and 8NW experienced the most significant increase of corner-to-center deflection ratio in the north test item. This can be due to loss of underlaying support. Upon completion of the traffic test, a terminal ratio over 2.0 was observed in the following corners: 3NW, 7NE, 8NW, and 8NE. The assessment of corner deterioration in these locations will be complemented with the void analysis presented in the following section.

On the south test item, the terminal corner-to-center deflection ratio in all corners evaluated, except 8SE were over 2.0 as seen in Figure 62(b). Furthermore, in corners 3SW, 4SW, 8SW, and 9SW slab corner deflections as high as 3 times slab center deflections were measured at some point during the traffic test. This is evidence that loss of support from underlaying layers in the south test item was more significant than the north side. Also, this is consistent with the deterioration observed in the south test item where corner breaks dominated the distress pattern. Moreover, this reinforces the speculation that the underlaying support conditions in the south test item may have induced the unexpected high rate of deterioration and premature failure relative to the north test item. The void analysis addressed in the next section will complement the evaluation of corner deterioration in the south test item.

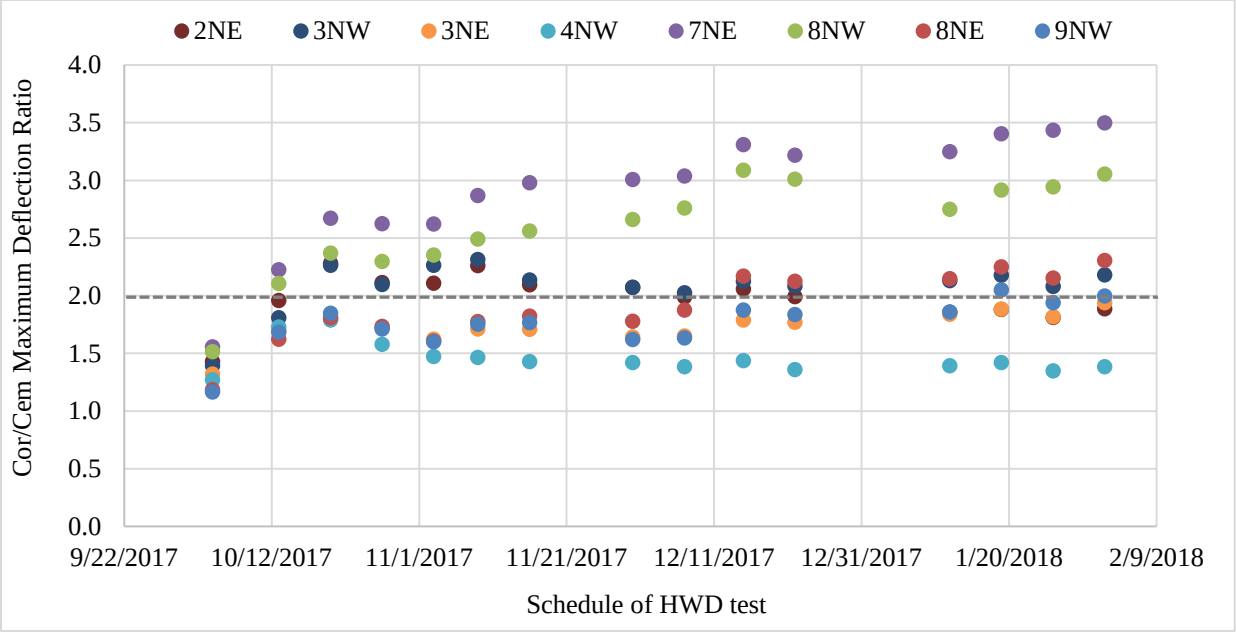

(a)

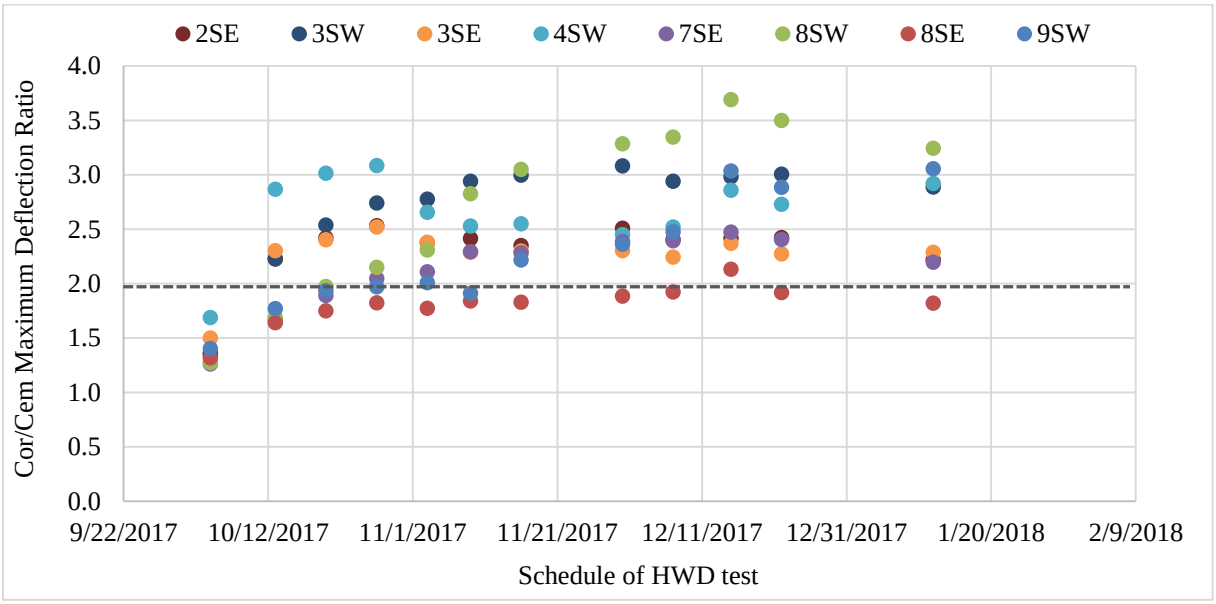

(b)

Figure 50. Corner-to-Center Deflection Ratio: (a) North Test Item, (b) South Test Item

Void Analysis

Slab support conditions are key for the performance of rigid pavements. The occurrence of surface distresses such as corner breaks, joint faulting, and slab cracking, can result from loss of support. Figures 51(a) through (d) show initial and terminal maximum corner deflections (D_0) from three HWD load levels for both the north and south test item. Intercept values along the vertical axis greater than zero, may indicate the presence of voids. If the intercept is small

enough, a void can be ruled out. Figure 51(a) and (b) show the maximum corner deflections from the baseline HWD testing on both the north and south test item. In both test items, intercepts close to zero were observed. This indicates that, prior to trafficking, there were no voids underneath the slab corners evaluated.

Figure 51(c) and (d) show the maximum corner deflections from the last HWD testing conducted on each test item. The traffic test on the north and south test item was terminated after 37,290 and 29,370 vehicle passes, respectively. Slab corners 3NW, 7NE, 8NW, and 8NE all had terminal corner-to-center deflection ratios greater than 2.0. Based on the observed intercepts, only corner 8NW exhibited a slight potential for void existence. However, no corner break was reported at this location. The presence of voids underneath all other corners evaluated in the north test item can be disregarded. Moreover, only one corner break was observed in the north test item which is consistent with the absence of evidence supporting the existence of voids.

On the south test item, slab corner 8SE was the only corner for which HWD analysis did not show evidence of a void. This is consistent with the analysis of corner-to-center deflection ratio where 8SE was the only corner with terminal corner-to-deflection ratio under 2.0. Intercepts for the remaining slab corners deviated from zero and indicated small to medium voids. In the case of corner 7SE and 8SW, there was only a slight potential for the existence of voids. In general, the presence of voids in the south test item is consistent with corner breaks dominating the distress pattern, and with the premature deterioration and failure relative to the north side. This also supports the supposition that there were deficient support conditions for some of the slabs in the south test item.

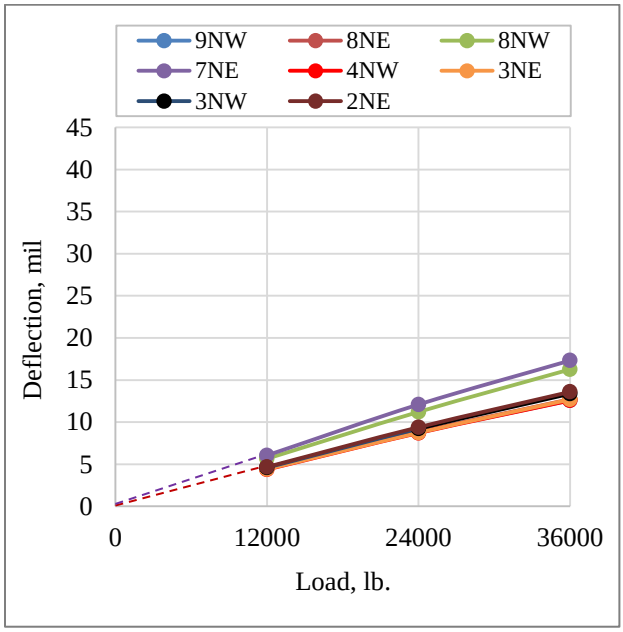

(a)

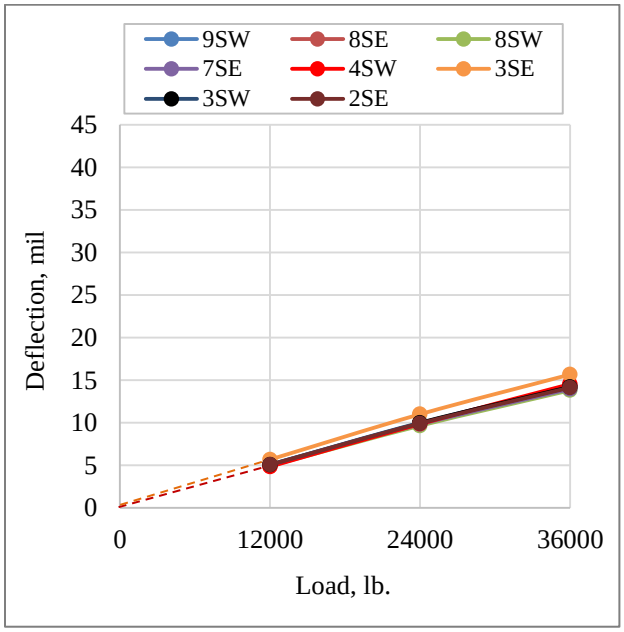

(b)

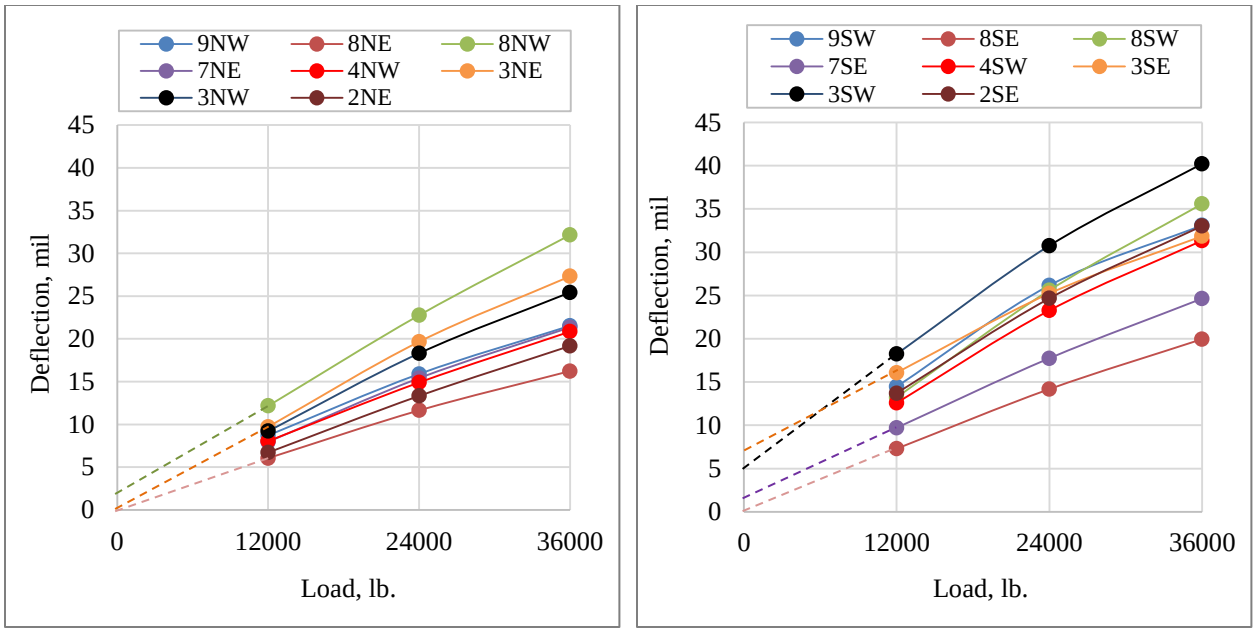

(c) (d)

Figure 51. Void Detection on Slab Corners: (a) Baseline-North, (b) Baseline-South, (c) Terminal-North, (d) Terminal-South

7.1.3 INTERIOR SLAB DETERIORATION

Interior slab deterioration was investigated using three parameters:

- ISM that represents the overall stiffness of an entire pavement system/cross-section
- Backcalculated layer moduli (*E*-values) that represent stiffness of individual layers
- Dissipated energy from material damage.

These parameters are discussed in this section.

ISM

Figure 52(a) and (b) show the change in ISM over the course of trafficking for both north and south side slabs. On both sides, the slabs along the inner lane (i.e., O1N through O5N and O1S through O5S on the north and south side, respectively) exhibited a gradual decrease in ISM values. Changes in ISM on the outer slabs were not significant. It indicated that the overall stiffness of the pavement system along the inner lane deteriorated due to traffic induced damage. A sudden drop in ISM observed in Figure 52(b) for slab O1S after about 11,000 vehicle passes is consistent with the observations made on deflection basin data in Section 6.2.1 (drop followed the occurrence of a diagonal crack across the center with subsequent slab shattering). This sharp drop in ISM was mainly due to the increase in measured deflections resulting from the severe deterioration undergone by the slab.

To understand the correlation between the overlay deterioration and overall pavement stiffness, average ISM values are plotted against SCI in Figure 53 for both the north and south test item. Prior to attaining a SCI value of 60, the decreasing trends in ISM on the north and south test item

were fairly close. Below this threshold SCI value, the ISM values on the North side shifted up before continuing the decreasing trend. Since then, it was observed that the averaged ISMs on north side are greater than those on the south side. A similar data shift of less magnitude was observed for the south test item when the overlay attained a SCI below 20. Since these threshold SCI values on both sides of the pavement were attained on the same date the coldest season begun, it is speculated that the ISM data shifts reflect the effect of temperature on measured deflections.
The increased stiffness of the asphalt interlayer at low temperatures possibly contributed to an increase of the overall pavement stiffness which leads to a drop in the measured deflections.

Backcalculated Layer Moduli

Layer moduli were backcalculated using the HWD deflection basin collected from the center of the slabs. The backcalculation was performed using BAKFAA. The pavement structure and material properties used for backcalculation are summarized in Table 12. Except for PCC, seed moduli were assigned based on material type. Both overlay and underlay PCC seed modulus was determined from PSPA tests which were conducted on the same locations as HWD tests. In the case of underlay, the terminal PSPA modulus from CC8 Phase I Test was assigned as seed modulus. It was also assumed that the PCC overlay was fully-bonded with the HMA interlayer. The same was assumed for the interface between P-154 and P-152 layers. Unbonded condition was assumed for all other interfaces. The section geometric parameters were assigned based on the layer thicknesses.

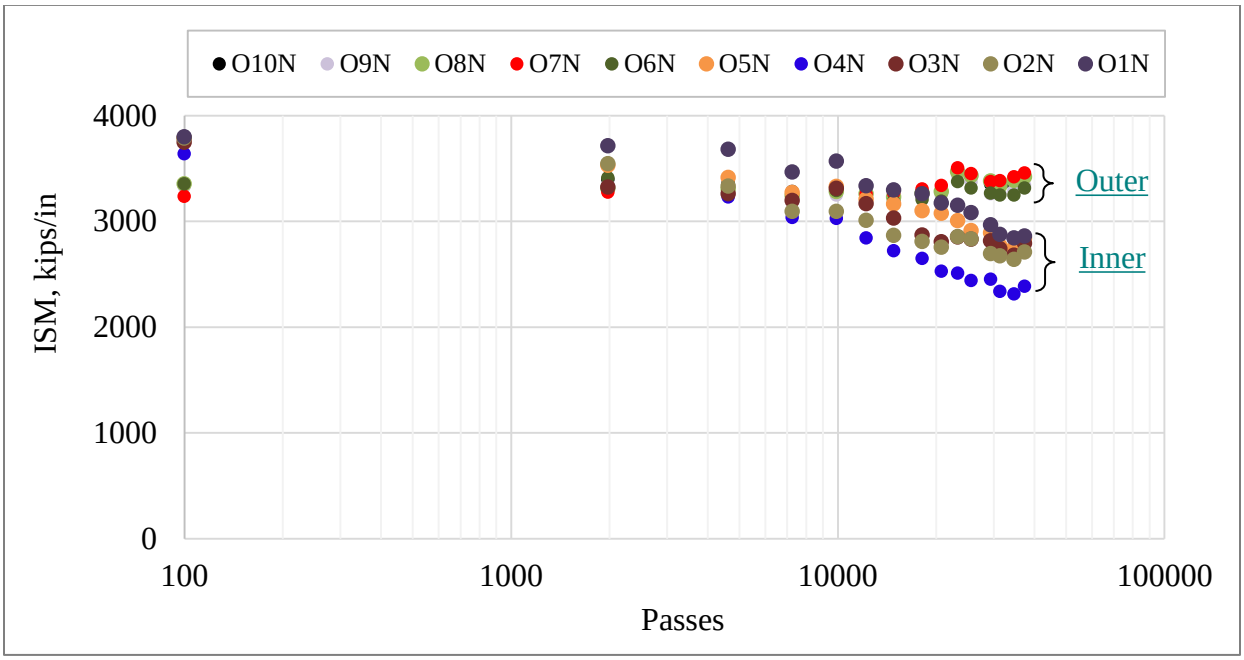

(a)

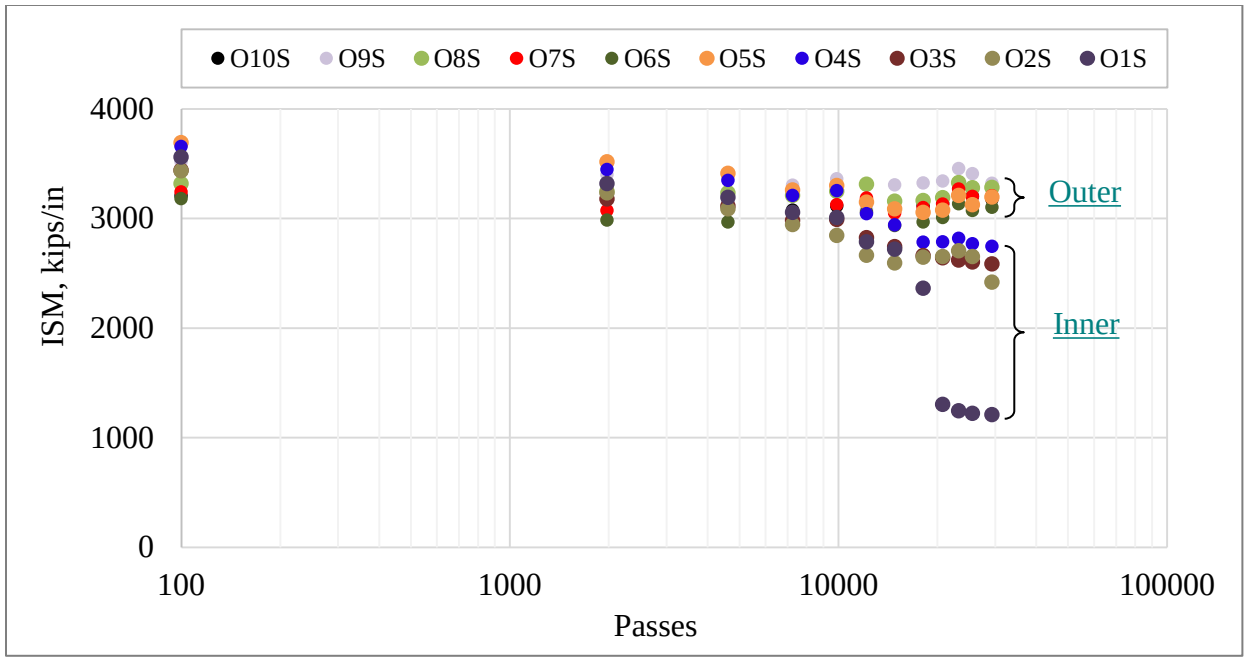

(b)

Figure 52. Change in ISM Over the Course of Traffic: (a) North Test Item, (b) South Test Item

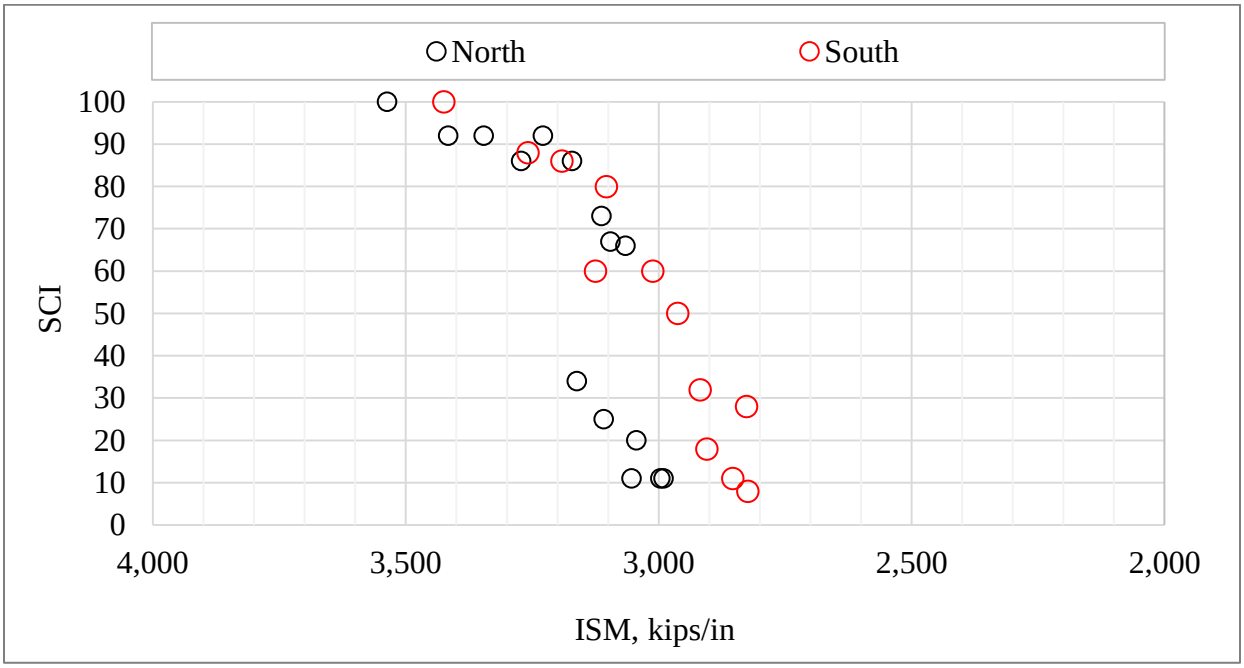

Figure 53. Changes in ISM with SCI

Table 12. Pavement Structure and Material Properties Used for Backcalculation

Layer	Seed Modulus (ksi)	Poisson's Ratio	Interface Condition	Thickness (in)
PCC (Overlay)	4800	0.15		9
			1.0[1]	
HMA (Interlayer)	350	0.35		1.4
			0.0[2]	
PCC (Underlay)	4100	0.15		9
			0.0	
Subbase	120	0.3		11
			1.0	
Subgrade	30	0.4		-

[1] *fully-bonded*
[2] *unbonded*

Moduli were backcalculated for five individual layers as indicated in Table 12. Later, moduli as backcalculated from different slabs were averaged on the north and south test item, respectively. Figure 54(a) through (e) show the trend of modulus variation over the course of trafficking. In general, the layer moduli degraded. The rate of modulus degradation was high in the PCC overlay and underlay compared to that in unbound materials. The layer moduli on the north test item were slightly higher than those on the south test item.

The unbound layers (i.e., subbase and subgrade) also degraded with slight difference in trends. Earlier, it was discussed that the deflection at some geophones located at higher radial offsets increased with pass number. The increase in those deflection values led to such trends in unbound layer moduli. The subgrade modulus started to degrade earlier than the subbase modulus. One possible reason is that the subgrade comprises clay, which is a stress-softening material, and thereby, stress increase in this layer due to progressive deterioration of the PCC overlay lead to a modulus degradation. Figure 55 shows the change in average PCC overlay modulus with change in SCI for both north and south test item. For both test items, the modulus degraded with decreasing SCI.

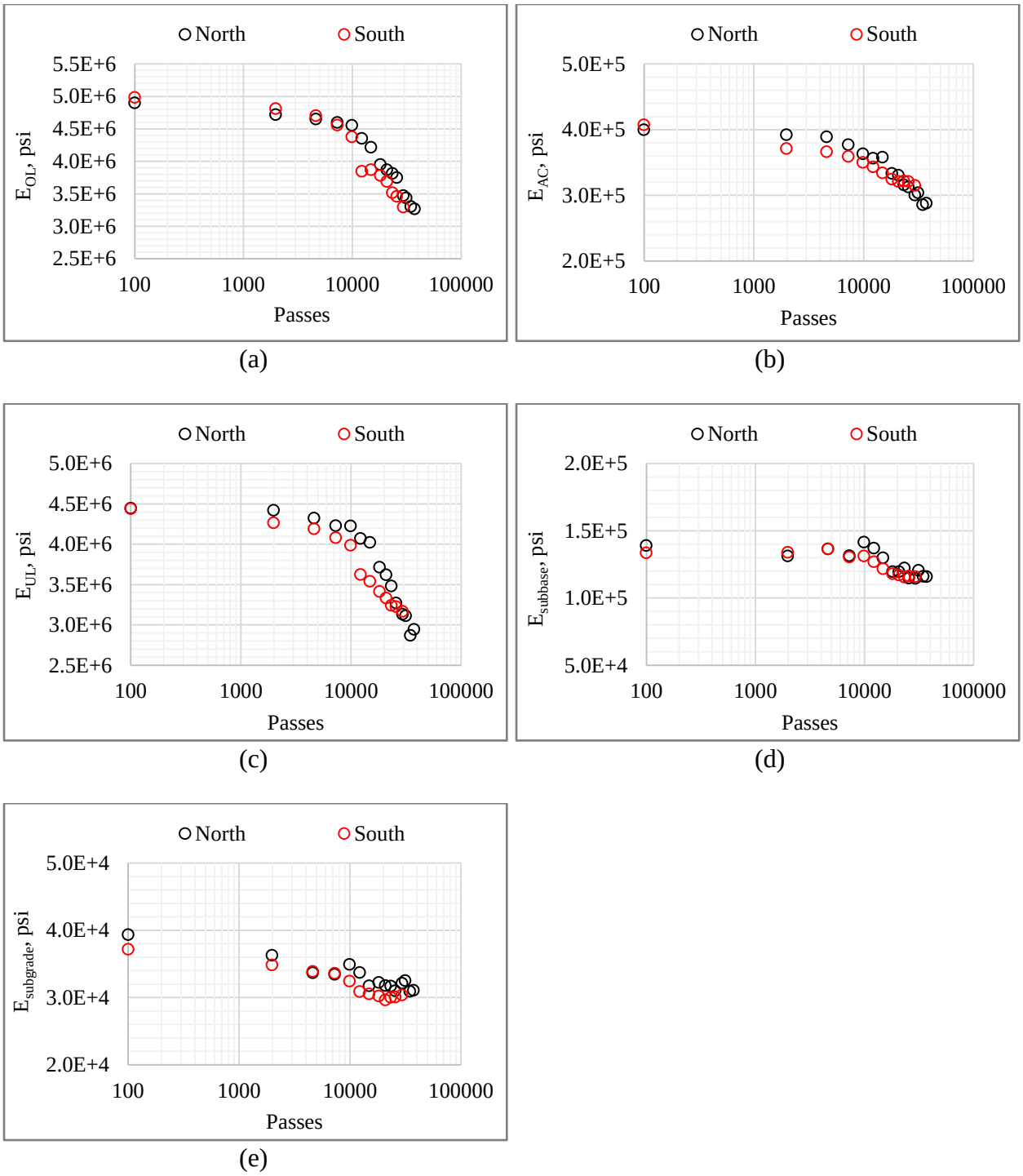

Figure 54. Change in Backcalcaulated Moduli of Pavement Layers Over the Course of Traffic: (a) Concrete Overlay, (b) Asphalt Interlayer, (c) Concrete Underlay, (d) Subbase, (e) Subgrade

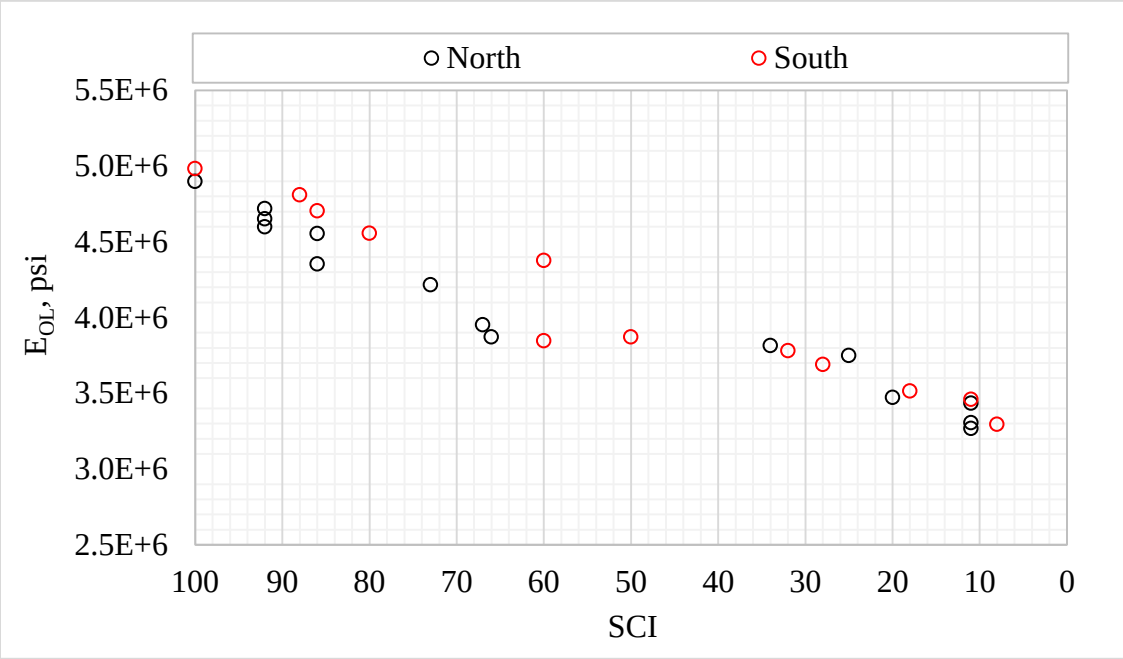

Figure 55. Change in the Overlay Backcalculated Modulus with Change in SCI

Dissipated Energy

It is known that net energy loss is zero whenever a linear elastic solid is subjected to a cycle of loading and unloading. In the case of dynamic loading, an amount of energy is typically dissipated from a system due to so-called inertial effect (i.e., time lag between load and resulting deformation). Energy can also be dissipated if a material exhibits viscosity, heat generation and/or damage. This energy can be quantified from an area enclosed within a load-displacement or stress-strain curve during a complete cycle of loading-unloading. Details on the methodology to compute dissipated energy from a 'Hysteresis Loop' as constructed during HWD testing can be found in the published literature (*9*). In the case of a pavement system that is subjected to dynamic loading at different times (e.g., HWD test), the amount of dissipated energy exclusively associated to the inertial effect and/or viscosity should be fairly constant. However, increasing dissipated energy can result from damage associated to either surface or underlaying distresses. Dissipated energy may have advantage over SCI and CD, in capturing material damage for the case of underlaying bottom-up cracks that are not fully propagated to the surface.

Based on this concept, the dissipated energy was calculated from the weekly HWD tests on inner slabs of both the north and south test item. Load and deflection time histories at the center of the loading plate were collected at 36,000-pound load. Prior to calculating the dissipated energy, both load and deflections were normalized to a 36,000-pound load. Figure 56(a) shows the hysteresis loop derived from normalized load-displacement data. These data were collected from a HWD test on slab O1N on October 13, 2017. The area enclosed within this loop was calculated by deducting the unloading area from the loading area. The calculation of dissipated energy was repeated for every round of HWD testing. Figure 56(b) shows the change in

dissipated energy over the course of traffic. Evidently, the amount of dissipated energy increased throughout the traffic test. Thus, changes in energy observed in this example might capture traffic-induced damage in and/or underneath the slab.

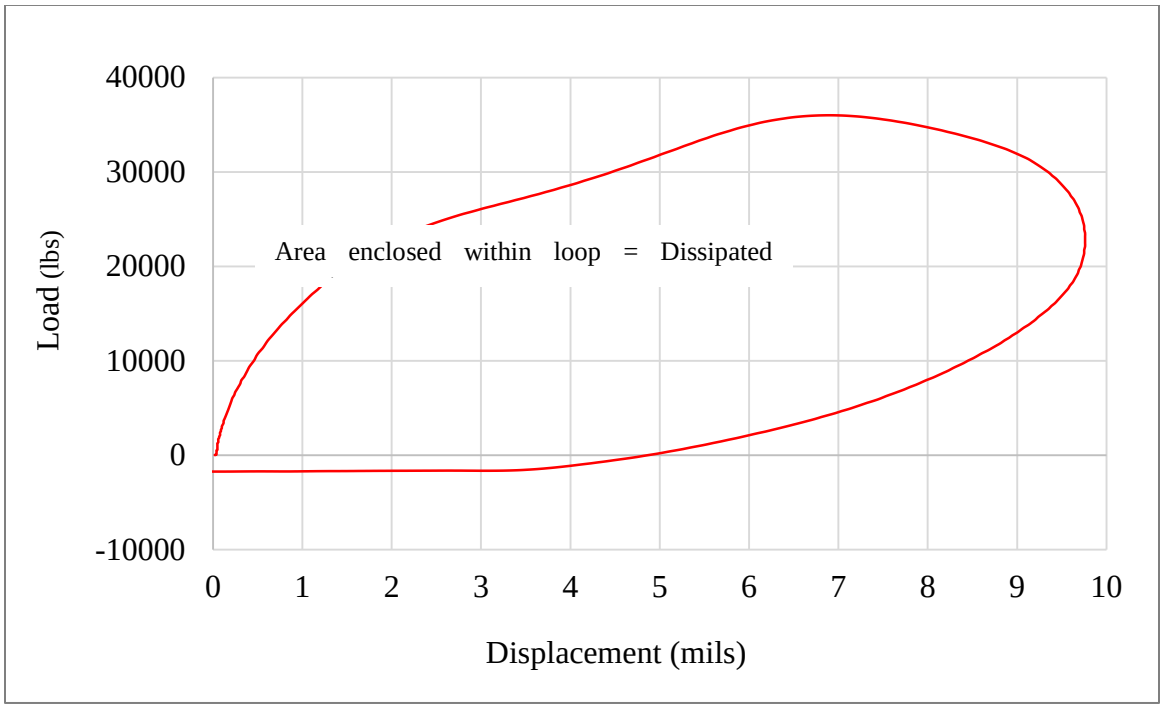

(a)

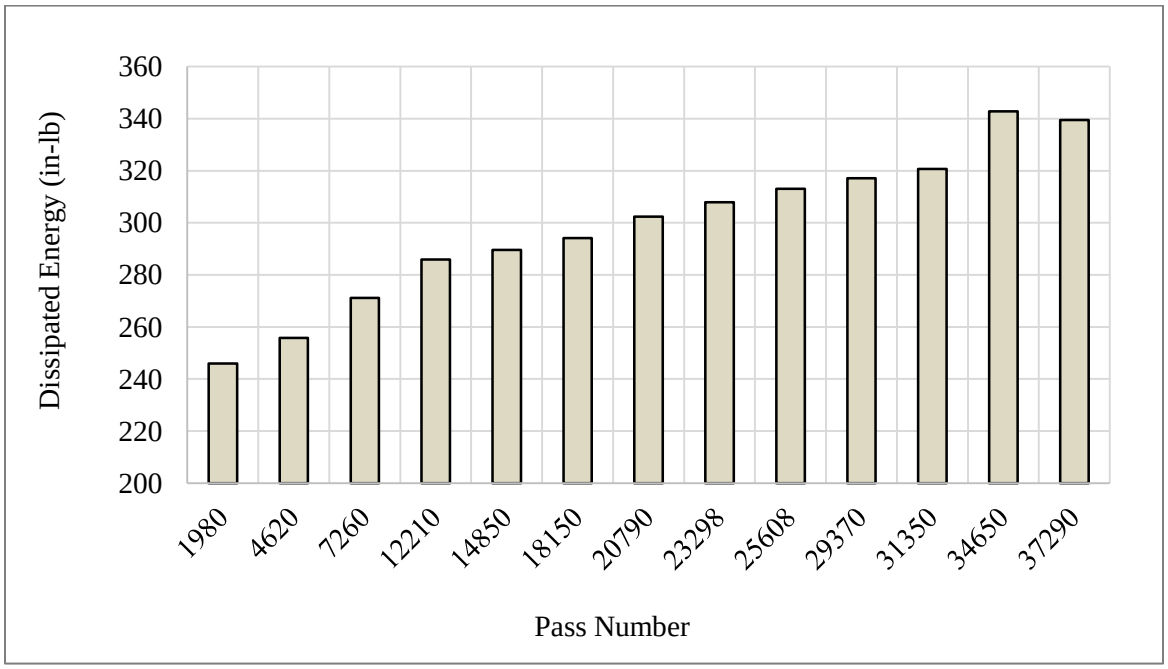

(b)

Figure 56. Dissipated Energy: (a) Calculation, (b) Change Over the Course of Traffic

In Figure 57, changes in dissipated energy were correlated to changes in crack density for the inner slabs of both the north and south test item. In general, both parameters increased with vehicle pass number. As shown in Section 6.1.2.2., a good correlation was found between crack density and pavement deterioration. Figure 57 shows that the changes in dissipated energy follow a similar trend as changes in crack density. Therefore, the inception and propagation of distresses quantified by crack density seem to be a factor driving the observed changes in dissipated energy.

In Figure 58(a) and (b), trends of change in dissipated energy and SCI are examined. It should be noted that the dissipated energy values were the average of all inner slabs on both the north and south test item. The dissipated energy increased with decreasing SCI. This indicates that the degradation of pavement structural integrity in terms of SCI can also be related to dissipated energy.

Dissipated energy increases with increasing crack density and decreasing SCI. The SCI was calculated considering load-related surface distresses, i.e., a portion of distresses that were included in crack density computation. Therefore, crack density and SCI were inter-related. Though the trends of dissipated energy over crack density and SCI show intuitive correlations, dissipated energy was expected to provide additional information regarding pavement damage (or stiffness reduction) due to possible presence of bottom-up cracking not shown on the surface. Considering that any increase in dissipated energy may indicate progression of damage in the overlay, degradation of the layer stiffness or modulus should be expected. In Figure 59, the backcalculated moduli of the overlay inner slabs was correlated to the dissipated energy for each test item. The overlay modulus degraded as dissipated energy increased. This suggests a potential for application of dissipated energy as an indicator of modulus degradation whenever crack density and/or SCI cannot capture the real scenario of pavement internal damage.

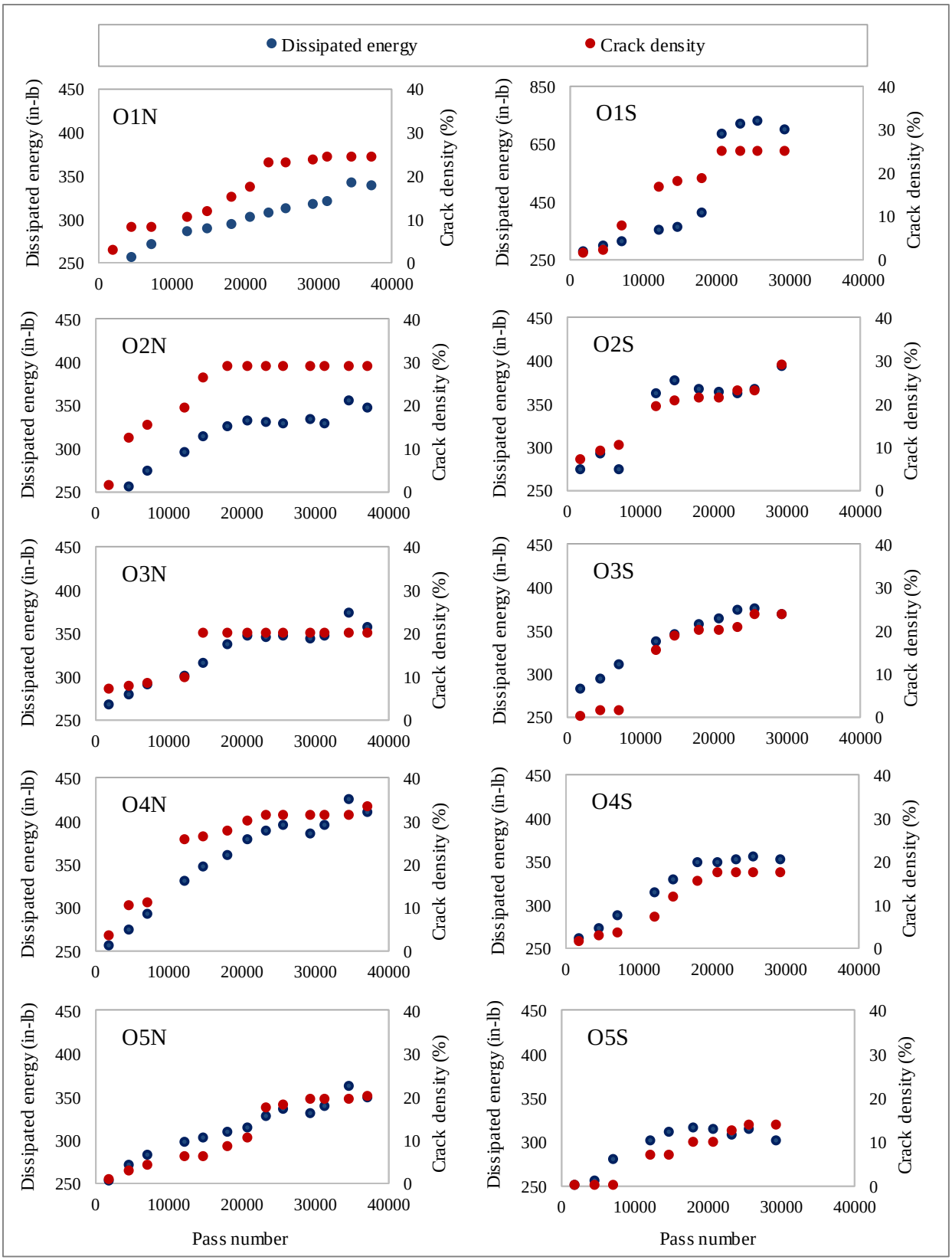

Figure 57. Comparison of Changes in Dissipated Energy and Crack Density with Pass Number

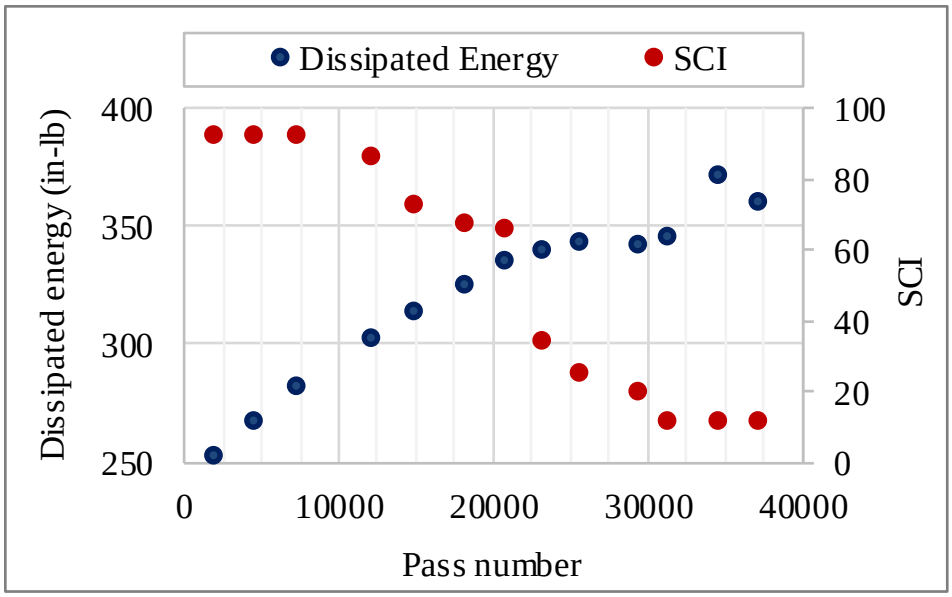

(a)

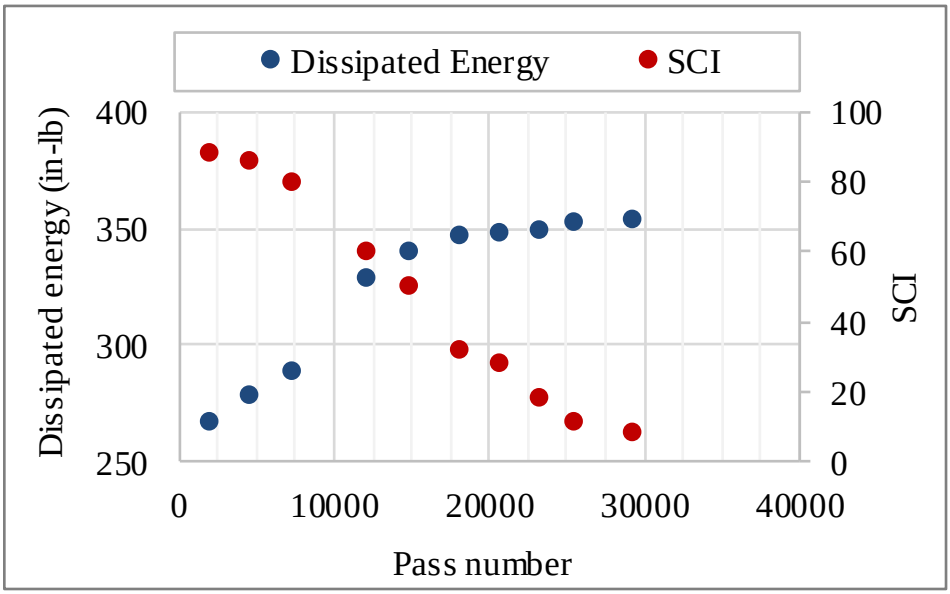

(b)

Figure 58. Comparison of Changes in Dissipated Energy and SCI with Pass Number: (a) North Test Item, (b) South Test Item

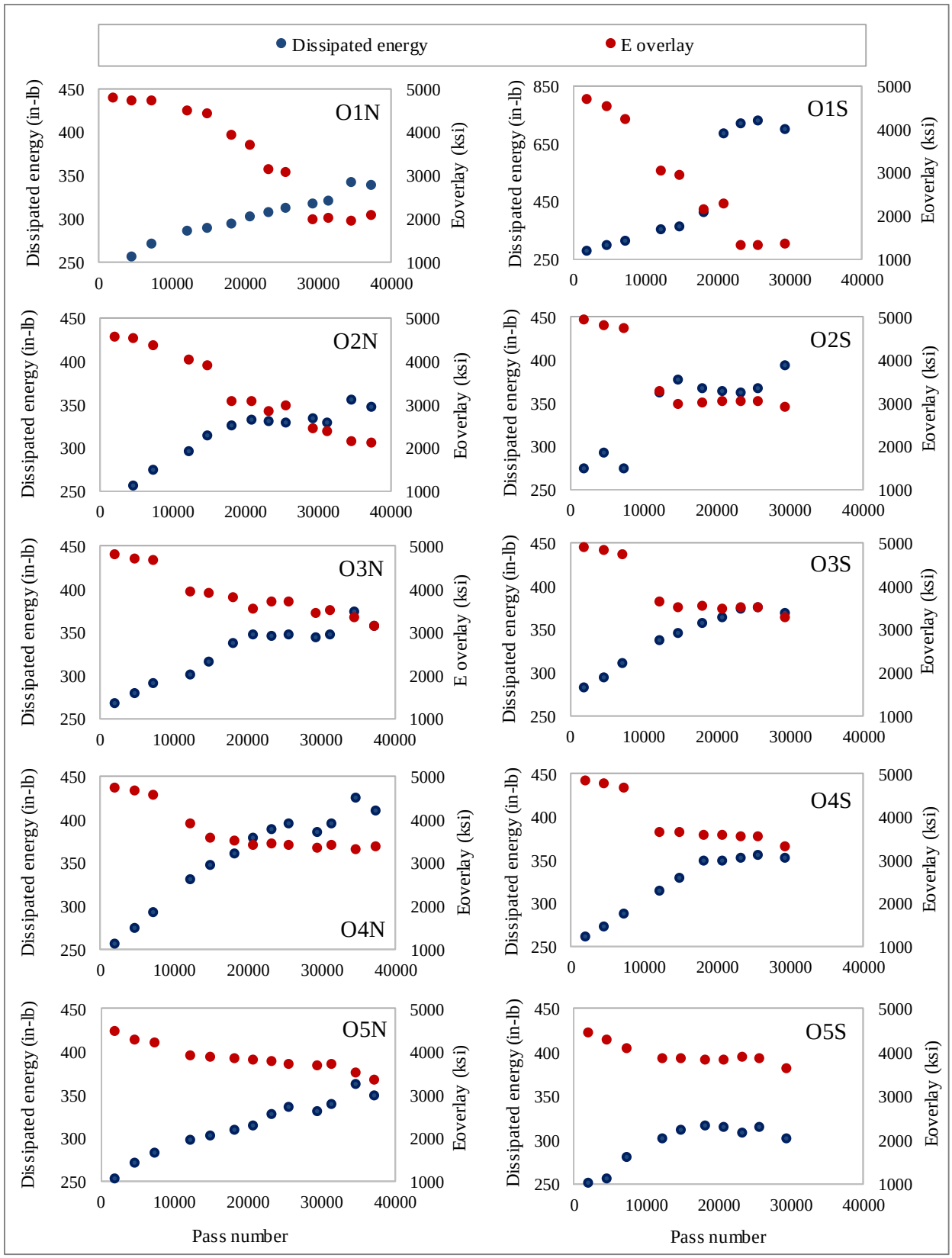

Figure 59. Comparison of Changes in Dissipated Energy and Overlay Modulus with Pass Number

7.1.4 JOINT DETERIORATION

There are 8 transverse joints (4 on the north and 4 on the south) in the overlay test area. HWD tests were conducted along these joints to determine the Load Transfer Efficiency (LTE) based on the deflection measurement. Figure 60 shows a schematic of a HWD testing to determine LTE. A 36,000 pound load was applied along the edge of a slab and the deflection at the center of the loading plate known as 'Loaded Deflection, δ_{ld}', was determined. At the same time, the deflection on the unloaded or free slab, was also measured 12 inch apart from the center of the loading plate using a geophone. This is known as 'Unloaded Deflection, δ_{ul}'.

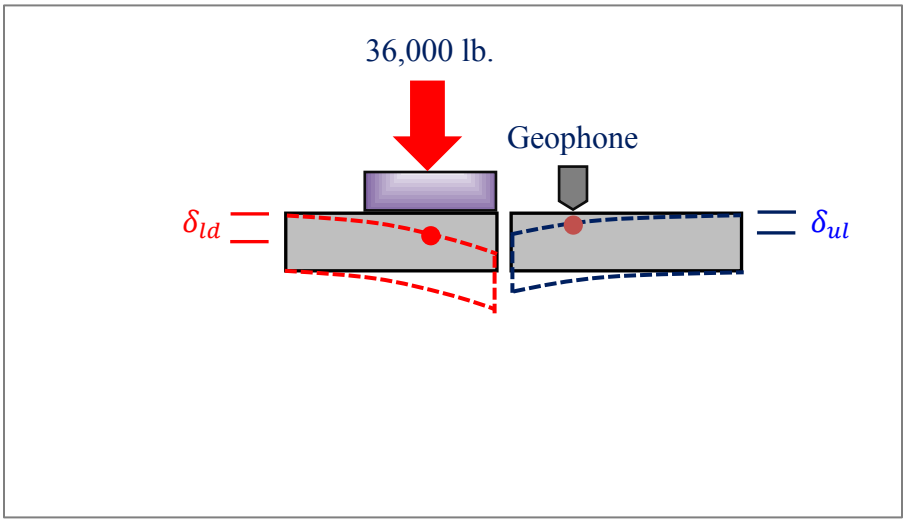

Figure 60. Schematic of a HWD Test to Determine LTE

LTE was then calculated based on the following relationship:

$$LTE_{\delta}(\%) = \frac{\delta_{ul}}{\delta_{ld}} \times 100 \qquad \text{Eq. 2}$$

LTE (%) varies from 0 to 100. HWD test along the selected joints were repeated from October 03, 2017 to February 02, 2018 on a weekly basis

Figure 61(a) and (b) show the trends of LTE degradation over passes along the transverse joints on both the north and south test item. The slab IDs correspond to the transverse joints. For instance, the transverse joint between slabs 9 and 10 is denominated 'O10N/O9N'. On the north test item, except for joints O5N/O4N and O8N/O7N, the initial LTE values along the joints were close to 90% as can be seen in Figure 61(a). Prior to completing 10,000 vehicle passes, the LTE degraded at a relatively slow rate. Beyond this pass number, the LTE started to drop rapidly. Joints O5N/O4N and O8N/O7N exhibited early deterioration of LTE. There was a drop of 18% in LTE along O5N/O4N after 10,000 passes which might be due to the occurrence of more distresses in slab O4N. The terminal LTE along this joint was 20%.

Figure 61(b) shows the LTE variation along transverse joints on the south test item. On this side, trafficking was terminated after 29,370 vehicle passes. In general, the rate of LTE degradation before 10,000 passes was relatively small. Beyond this pass number the rate of LTE degradation showed a sharp increase in most of the transverse joints. Figure 62 shows the correlation between averaged LTE and SCI for both the north and south test item. The LTE gradually decreased with decreasing SCI. In summary, the joint performance in terms of LTE deteriorated over the course of trafficking due to the gradual accumulation of distress on pavement surface. In addition, considering both the north and south test item, an LTE ranging between 55% and 65% was attained when the SCI dropped to about 10.

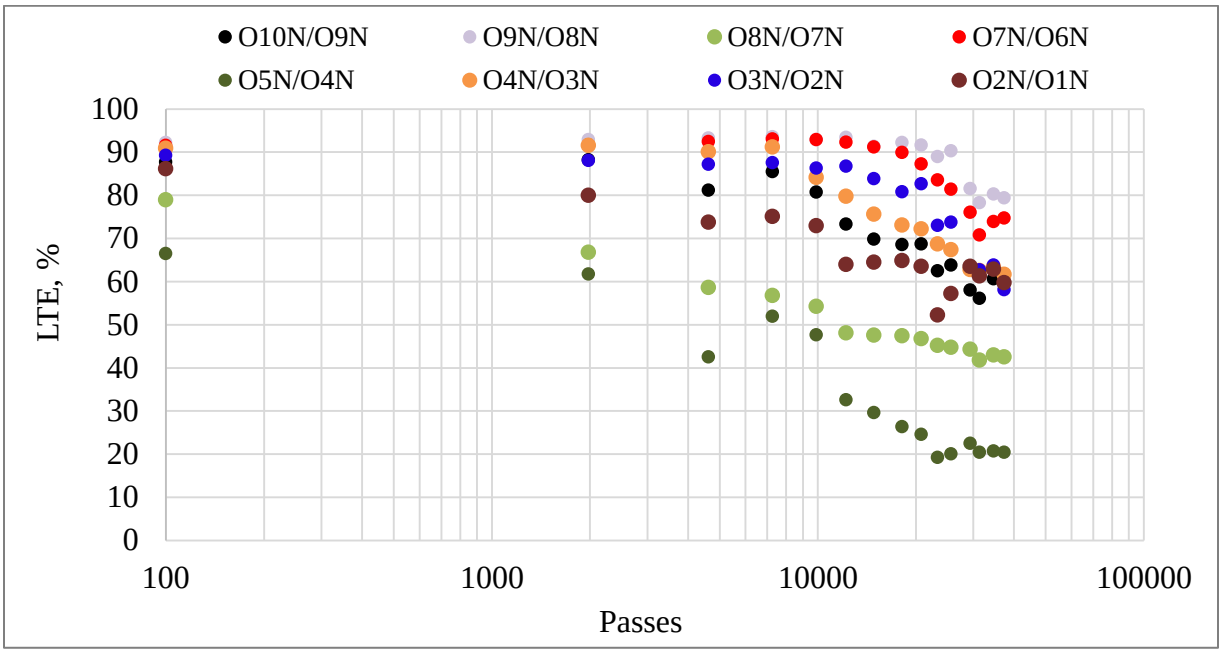

(a)

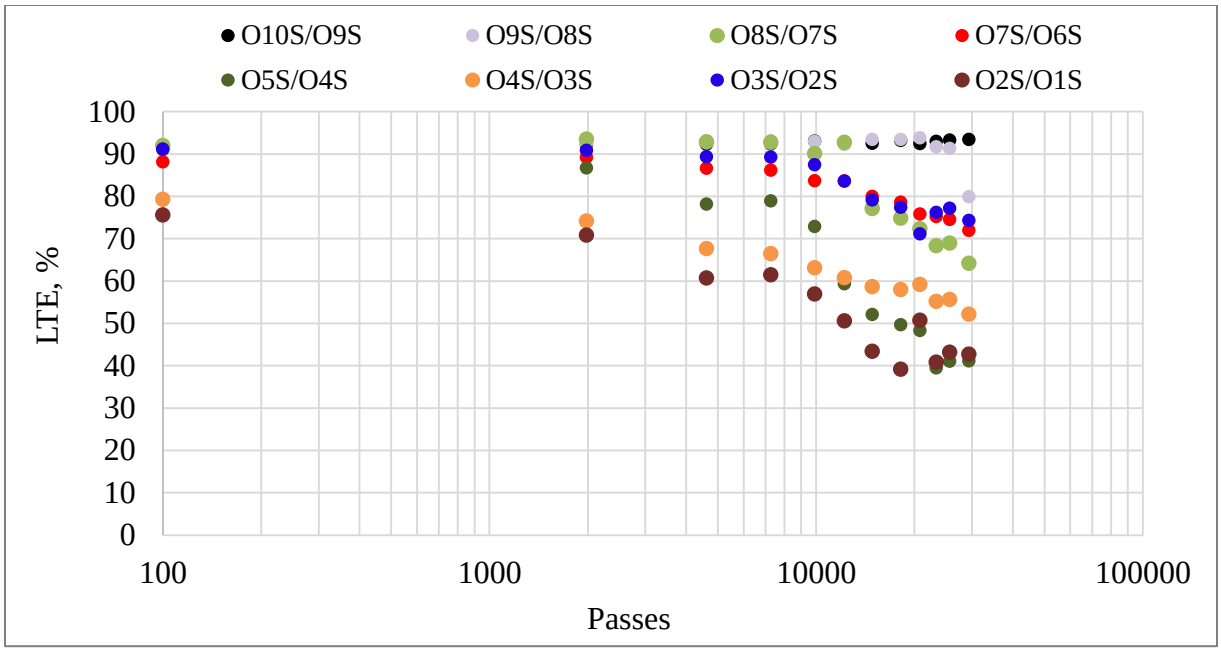

(b)

Figure 61. Change in LTE Over the Course of Traffic: (a) North Test Item, (b) South Test Item

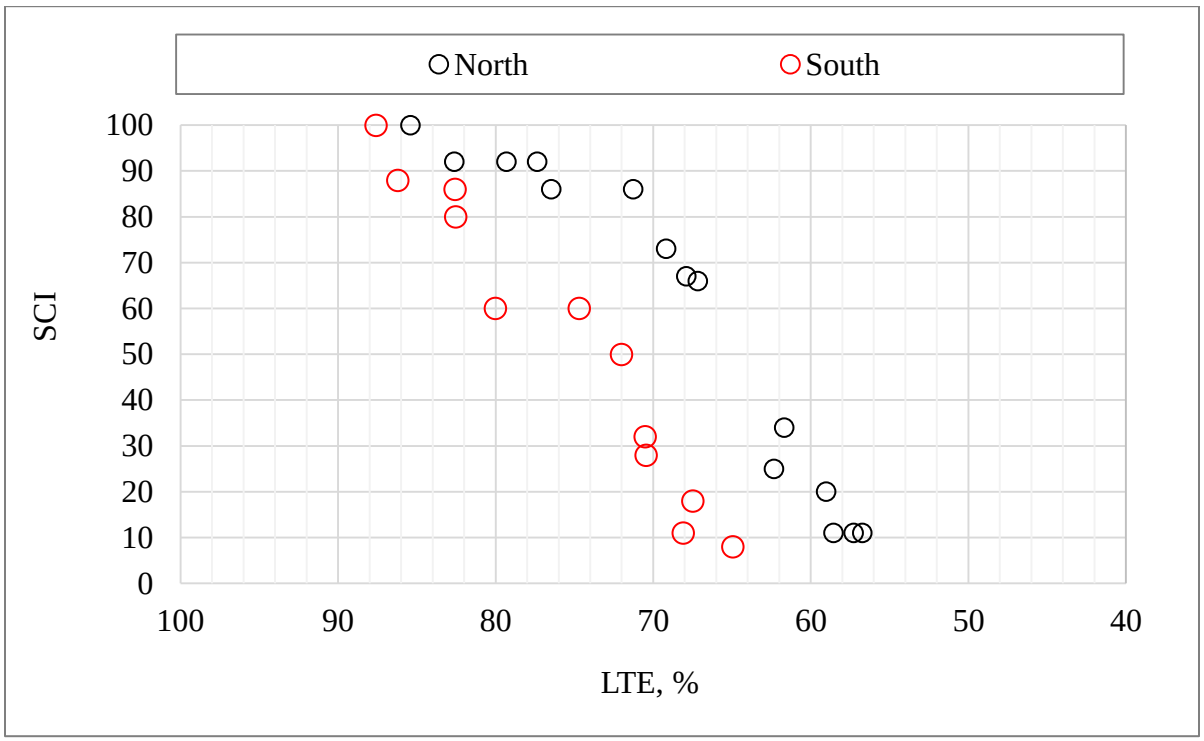

Figure 62. LTE Degradation due to SCI Rating

7.2 PERFORMANCE CURVE

Discrepancies between the FAARFIELD failure prediction and the actual overlay deterioration during the traffic test can be observed in Figure 63. The predicted number of passes to failure were 31 and 103 for the north and south test item, respectively. The overlay actually required 13530 and 5940 passes to achieve a SCI value around 80 in the north and south test item, respectively. In this section, the performance curve is evaluated using the newly generated full-scale test data from the CC8 Phase II Overlay experiment.

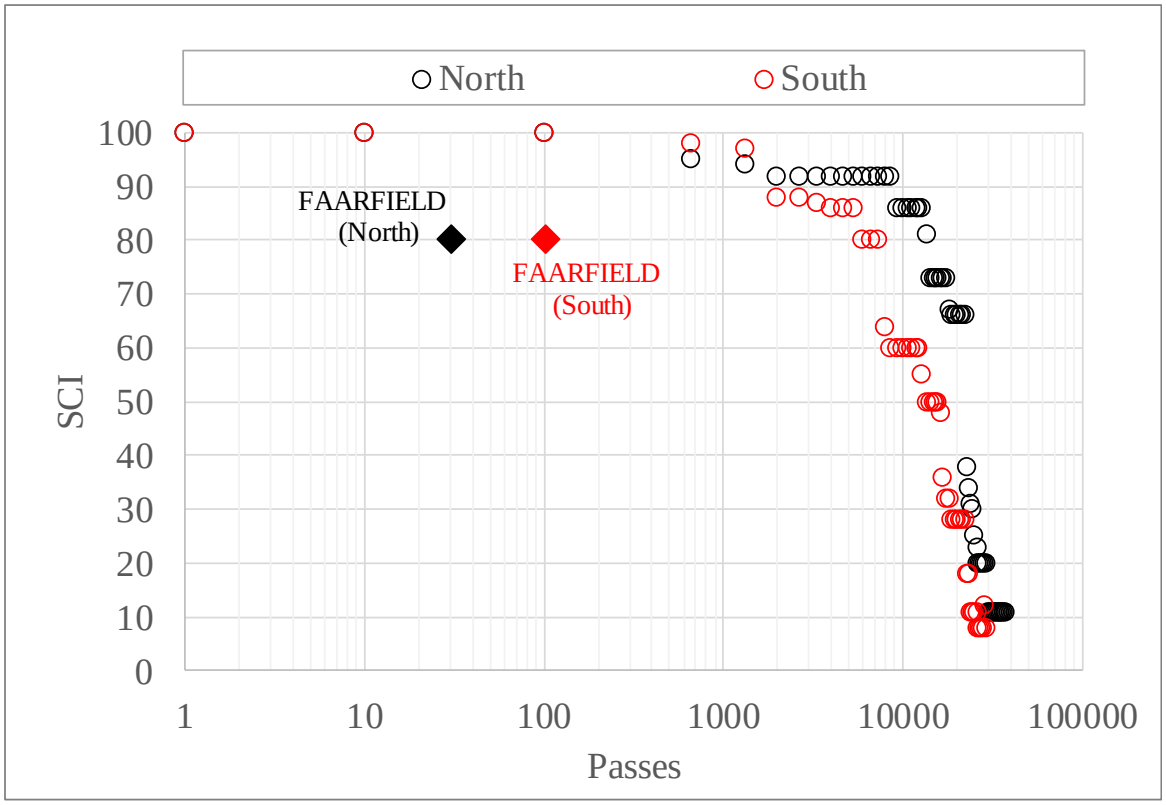

Figure 63. Observed Changes in SCI versus FAARFIELD Failure Prediction

In the late 80s, Rollings proposed a mechanistic-empirical design procedure introducing the Structural Condition Index (SCI) as a modification to the Pavement Condition Index (PCI) (*5*). The SCI parameter only considers those distress types associated to pavement fatigue damage. Since then, the SCI method for describing the pavement performance became a fundamental component in the subsequent development of overlay design procedures. The rigid pavement performance model proposed by Rollings is illustrated in Figure 64 (*5*). In the model, the pavement undergoes no deterioration under traffic until the parameter C_O (Figure 64) is reached. After this, the pavements deterioration is a linear function of the logarithm of coverages. The deterioration continues until the parameter C_F is reached. Rollings stated that provided these parameters can be predicted, the SCI value at any given coverage can also be predicted. Using C_O and C_F to normalize the traffic coverage data, Rollings found a relationship between normalized coverage (C_N) and SCI as shown in Figure 65 (*5*).

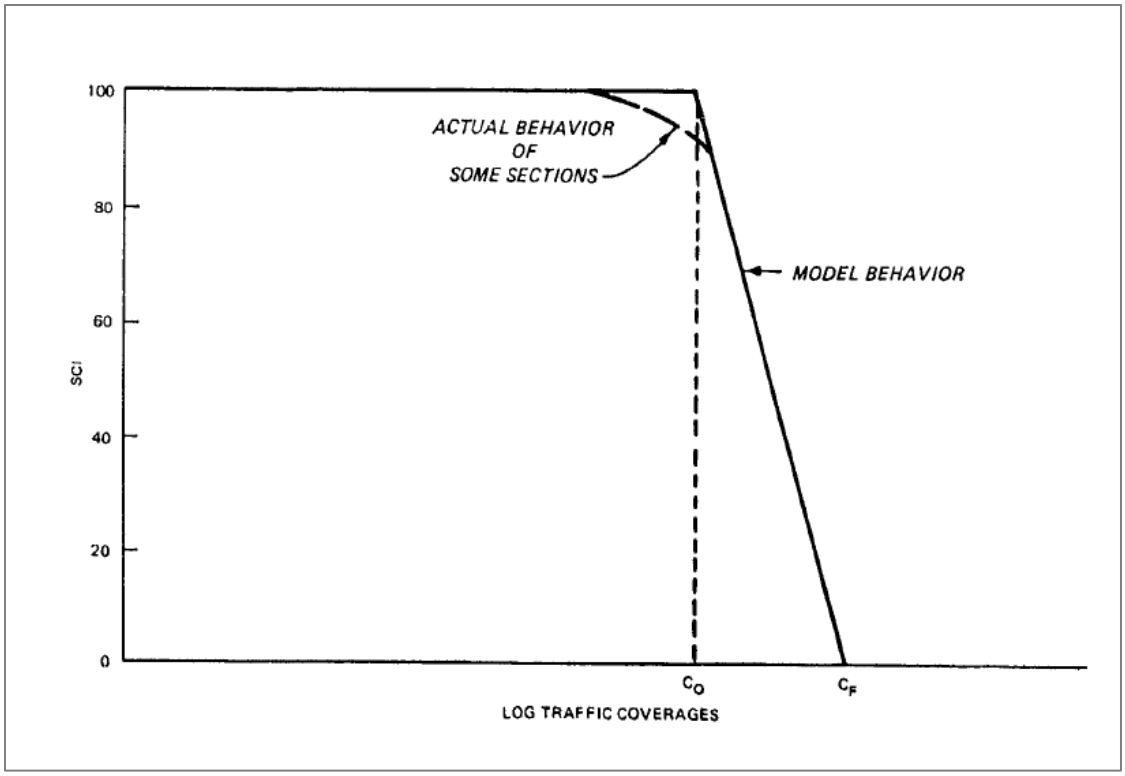

Figure 64. Performance Model Proposed by Rollings (5)

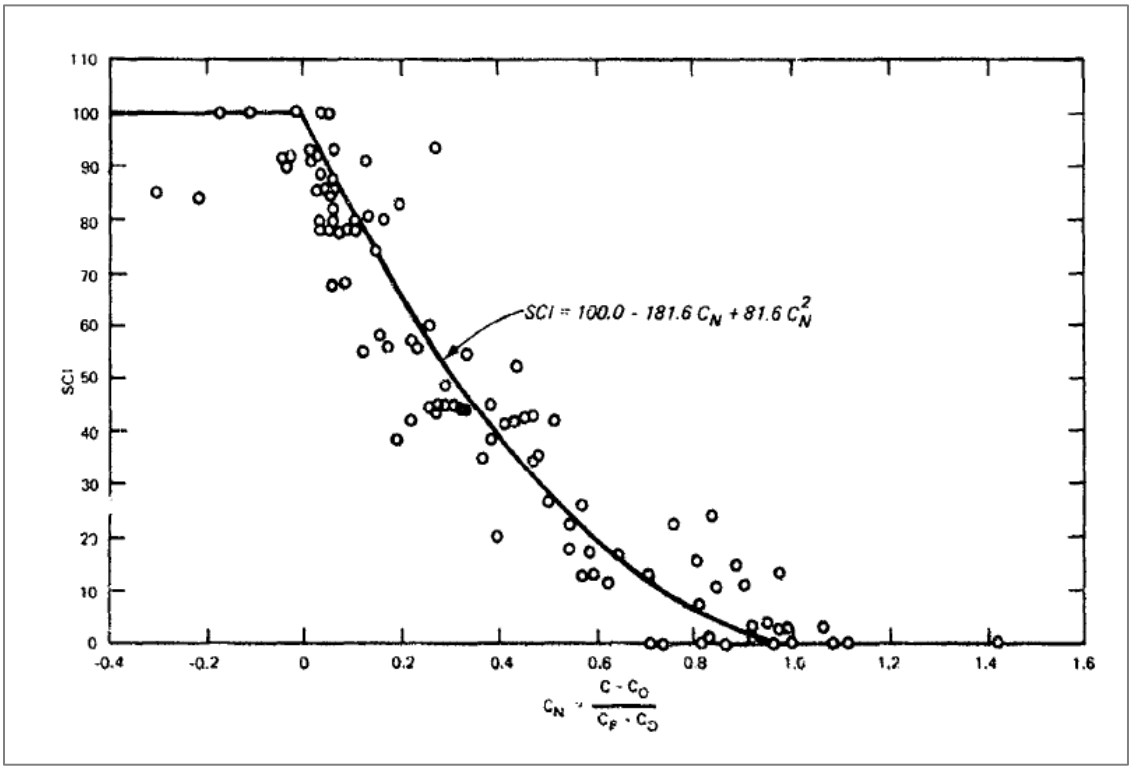

Figure 65. Relationship Between Normalized Coverage and SCI by Rollings (5)

Interpreting the C_N – SCI relationship as a measure of the rate of structural deterioration with traffic, the concave shape of the curve in Figure 78 indicates slowing deterioration rate. In Figure 79, the data generated in the overlay experiments conducted during CC4 show a linear deterioration trend when compared to Rollings model, indicating a relatively constant rate of deterioration (*3*). The newly generated full-scale test data from the CC8 Phase II Overlay experiment verified the linear deterioration trend reported in CC4. In Figure 80, the CC8 linear relationship is compared to Rollings model. Although the north and south test item deteriorated at different rates, when combining both datasets the overall rate of deterioration was found to be relatively constant. Furthermore, when comparing the CC4 to CC8 linear relationship, both show similar slopes.

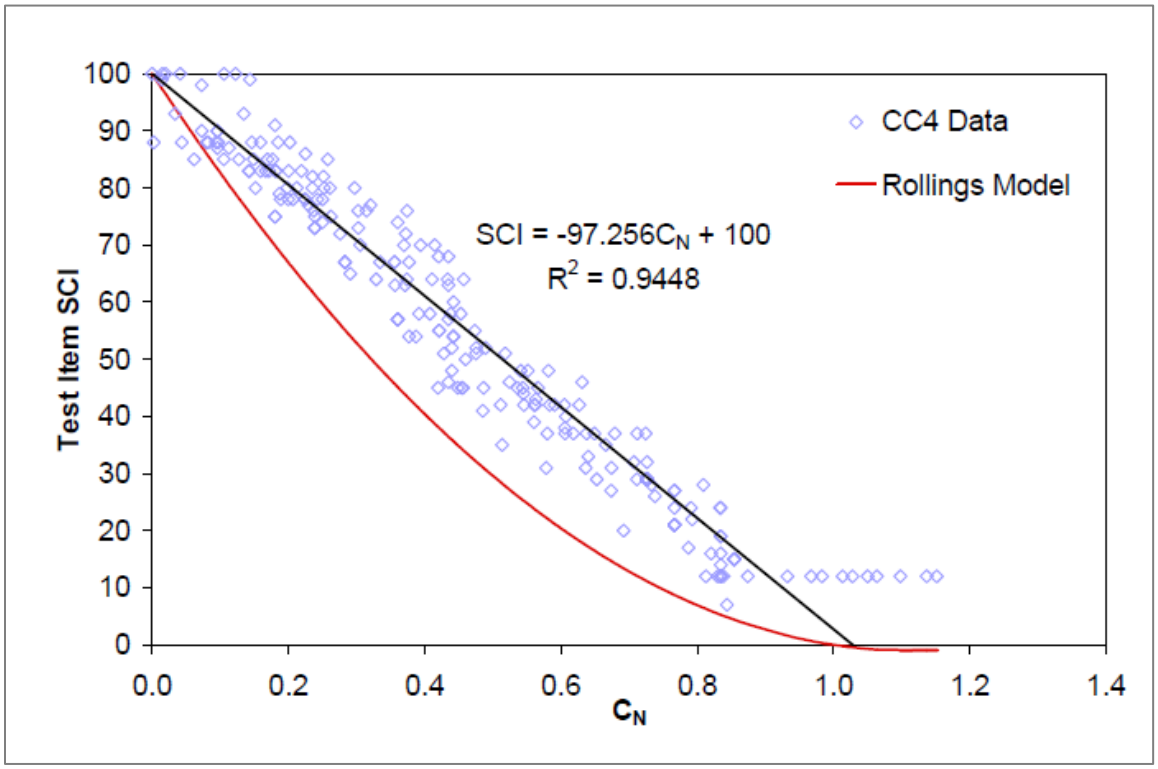

Figure 66. Relationship Between Normalized Coverage and SCI Based on CC4 Test Data

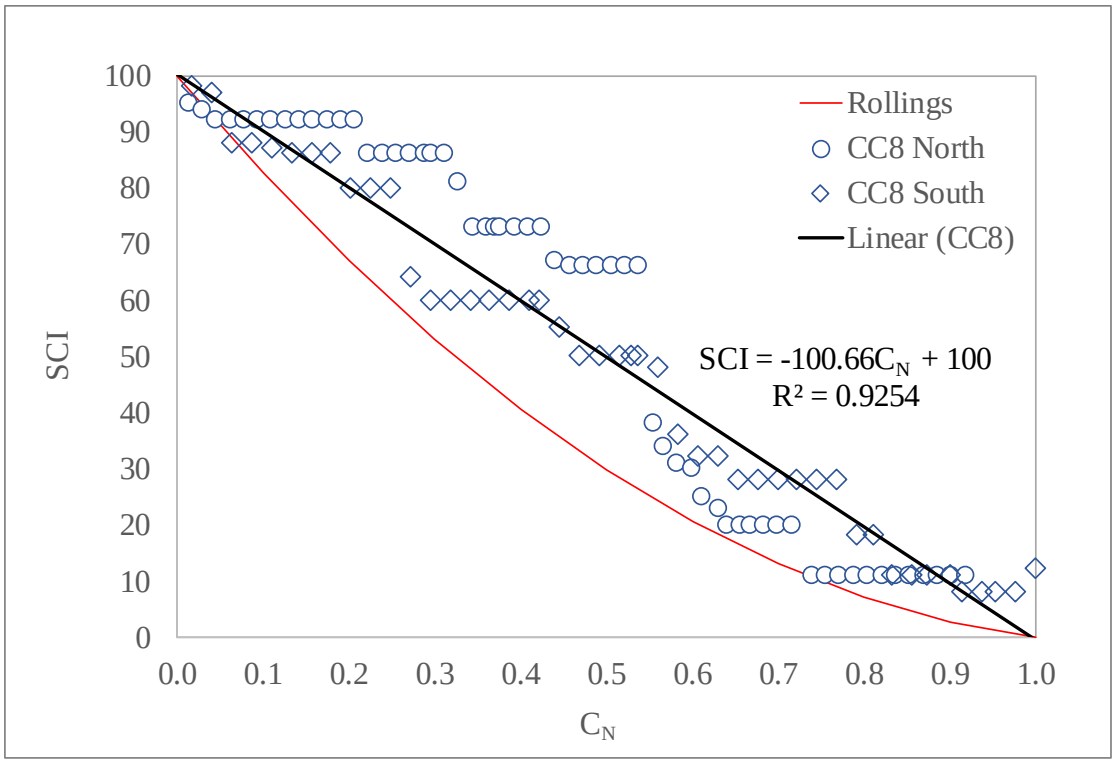

Figure 67. Relationship Between Normalized Coverage and SCI Based on CC8 Overlay Test Data

7.3 JOINT STIFFNESS

Joint stiffness was calculated using the deflection values from HWD testing. Figure 68 shows a schematic of HWD test to measure surface deflections as required for this purpose. The loading plate was placed along the edge of a slab in such a way that the center of the plate and the second geophone, positioned 12 inches from the center of the load plate, were equidistant to the joint opening. The last geophone, positioned 72 inches from the center of the load plate, was 66 inches apart from the joint opening. The deflections at the center of the loading plate measured by the first geophone are designated D_{-6}, whereas the deflections measured by the second and last sensors are designated D_6 and D_{66}, respectively. The difference between the deflections on both sides of a joint opening is known as vertical shear displacement as illustrated in Figure 68.

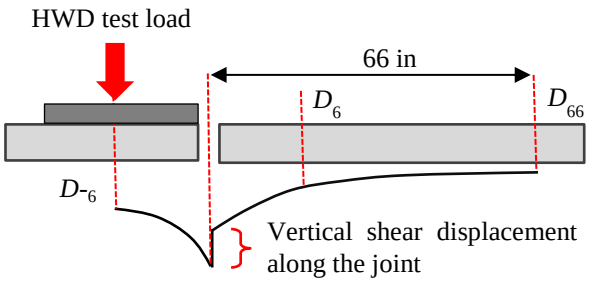

Figure 68. Schematic of HWD Test for Joint Stiffness Calculation

Once the deflections were collected from HWD testing, the joint stiffness (k_J) was determined using the following relationship proposed by Byrum in 2011 (*10*):

$$k_J = P(LTE_\delta)/\left[(1 + LTE_\delta)(D_{-6} - D_6)(1 + i\%)\Omega\left(66 + 60D_{66}/(D_6 - D_{66})\right)\right] \quad \text{Eq. 3}$$

where,

LTE_δ is the deflection based *LTE*, *i*% is the percentage increase factor needed to project the sensor readings out to the joint line, and Ω is an unknown function that converts an assumed simplified linearly approximated shear area into the true shear area. This function value was set equal to 1.0 for this study.

The joint stiffness was also calculated from the LTEs using the following relationships (*11*, *12*):

$$LTE_\delta = \frac{1}{1+log^{-1}\left[\frac{0.214-0.183\left(\frac{\varepsilon}{\ell}\right)-log(f)}{1.18}\right]} \quad \text{Eq. 4}$$

$$log(f) = \left[0.434829\left(\frac{\varepsilon}{\ell}\right) - 1.23556\right] log\left(\frac{1}{LTE_\delta} - 1\right) + 0.295205 \quad \text{Eq. 5}$$

$$LTE_\delta = \frac{100\%}{1+1.2\left(\frac{AGG_{tot}}{k\ell}\right)^{-0.849}} \quad \text{Eq. 6}$$

where,
$f = {q_0}/{k\ell}$,
q_0 is joint stiffness in. lb./in./in.;
ε is wheel load radius in in.;
ℓ is pavement radius of relative stiffness in in.,
k is the modulus of subgrade reaction in pci, and
AGG_{tot} is total joint stiffness in lb./in./in.

Equations 4 and 5 were developed by Ioannides and Hammons in 1996 (*11*). These equations simulate two infinite slabs connected by one infinitely long joint. The first form is known as 'LTE_δ regression for the Skarlatos/Ioannides Solution' and it was developed through a regression analysis based on the following matrix equation:

$$[Measured\ LTE_\delta] = [Skarlatos/Ioannides\ LTE_\delta\ as\ f(best - fit\ k\ell)] + [error] \quad \text{Eq. 7}$$

In this equation, the known variables were wheel load radius, slab thickness, slab modulus, and measured joint stiffness. The unknown variable was modulus of subgrade reaction, which was used as an optimization variable. Later, the second form was developed which was known as '*log(f)* regression for the Skarlatos/Ioannides solution'. During the development of this form through a regression analysis, the following matrix equation was used:

$$\left[log\left\{(FWD\ stiffness)\Big/(best - fit\ k\ell)\right\}\right] = [Skarlatos/Ioannides\ log(f)] + [error] \quad \text{Eq. 8}$$

The joint stiffness, slab thickness, backcalculated slab modulus, and $log(f)$ were used in the optimization step during the regression analysis. Regression based on the second form tends to spread the measured data more evenly into a more uniform distribution.

Equation 6 was proposed by Crovetti in 1994 (*12*) to compute joint stiffness directly from LTE_δ whenever the other parameters such as slab modulus, modulus of subgrade reaction, and so on, are known.

Once the joint stiffness was calculated using the equations shown above, the correlations between *LTE* and joint stiffness were plotted. Considering the stiffness obtained with Equation 3 as the measured value, in Figure 69 the predicted joint stiffness calculated using Equations 4, 5 and 6 are compared to the measured stiffness. In general, both measured and regression model-based joint stiffness (i.e., Eq. 4, 5 and 6) followed similar trends as function of *LTE*.

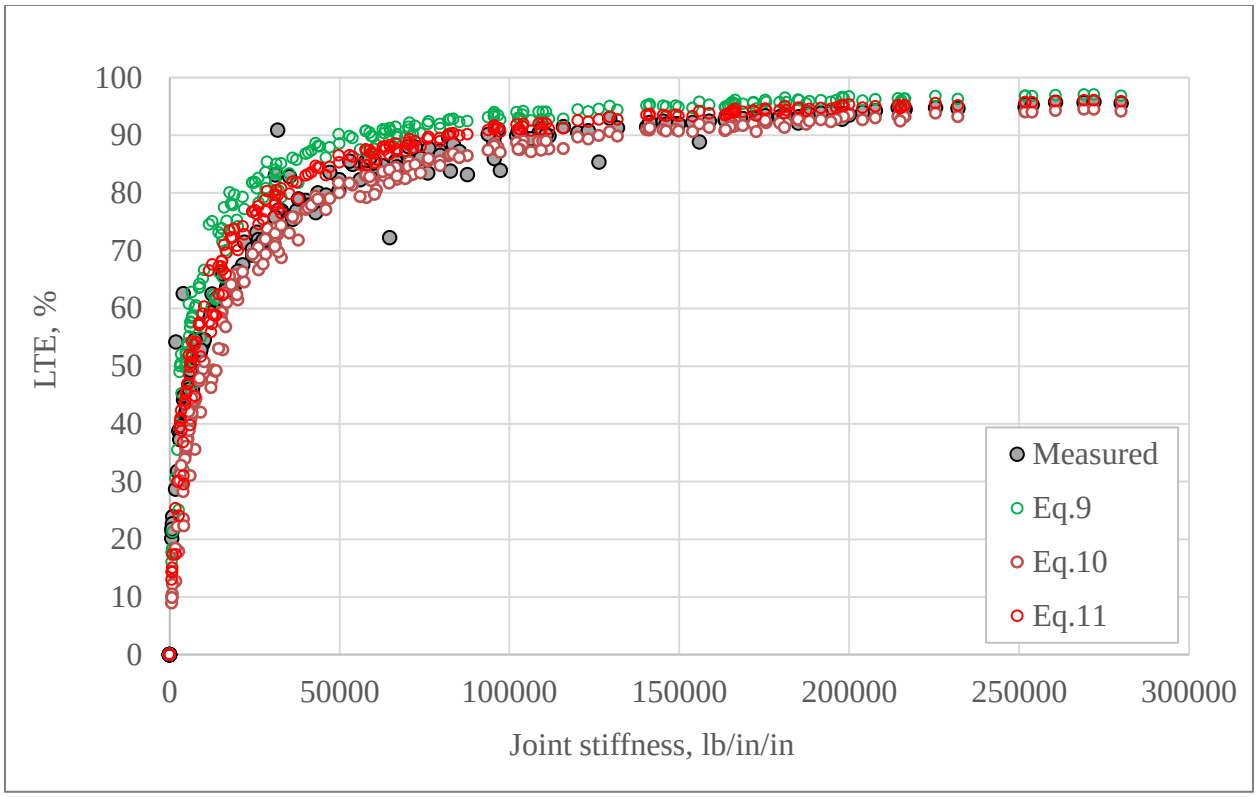

Figure 69. Joint Stiffness as Function of LTE

8. CONCLUSIONS AND RECOMMENDATIONS

An unbonded concrete overlay was built over an existing rigid pavement with intermediate levels of deterioration and target SCI near 80. The CC8 overlay test was intended to fill in significant gaps in data from past unbonded rigid overlay experiments conducted during CC4, which included new (SCI 100) and severely deteriorated (SCI 20-50) underlay slabs. Traffic testing began in October 2017 and ended in February 2018. This report provides details on the execution of the experiment and the analysis of the full-scale test data set. Key findings and recommendations for future research efforts are summarized in this section.

8.1 CONCLUSIONS

- Corner breaks and longitudinal cracks dominated the distress pattern. Premature localized damage in the south test item possibly triggered reflective cracking from CC8 Phase I longitudinal joints. Random, tight, isolated interior surface cracks were also observed in the north test item during the early stage of traffic with delayed initiation of reflective cracking, relative to the south side.

- Underlay damage with higher incidence on the south side, during the overlay traffic test is suspected. The premature deterioration and failure in the south test item may have reflected the underlay deterioration pattern. Assessment of the underlay final condition

during CC8 forensic investigation is expected to provide additional elements to explain the observed distress pattern.

- Similar to the approach followed in CC4, crack density was evaluated as an indicator of overlay deterioration. Good agreement was found between crack density and SCI. The analysis of dynamic instrumentation data provided key elements for the subsequent development of "localized crack density," a parameter that was found to better capture and reflect the effect of local distress.

- The evaluation of the neutral axis position (NAP) using dynamic instrumentation data evidenced the effect of the HMA interlayer on the mechanical response of the concrete overlay.

- An evaluation of slab corner deterioration was conducted. In general, both high corner-to-center deflection ratios and the detection of voids in the south test item was found to be consistent with corner breaks dominating the distress pattern, and with the premature deterioration and failure relative to the north side. This also supports the diagnosis of a deficiency in the underlaying support conditions in the south test item.

- An evaluation of the slab interior deterioration revealed that backcalculated moduli and ISM captured the degradation of the overall stiffness of the pavement. Dissipated energy from the load-deflection hysteresis loop based on HWD test data was introduced in the analysis as an indicator of structural damage. Increasing dissipated energy was observed with increasing crack density, and decreasing overlay modulus and SCI.

- The joint deterioration was evaluated in terms of LTE. A good correlation was observed between LTE and SCI. Considering both the north and south test item, an LTE ranging between 55% and 65% was attained when the SCI dropped to about 10.

- Discrepancies between the FAARFIELD failure prediction and the actual overlay deterioration during the traffic test were observed. The predicted number of passes to failure were 31 and 103 for the north and south test item, respectively. The overlay actually required 13530 and 5940 passes to achieve a SCI value around 80 in the north and south test item, respectively.

- CC8 Phase II Overlay test data verified the linear deterioration trend reported in CC4. Compared to Rolling's performance model, rather than showing a slowing deterioration rate, the CC8 linear relationship shows a relatively constant rate of deterioration. Furthermore, when comparing the CC4 to CC8 linear relationships capturing the overlay deterioration, both show similar slopes.

- The deterioration rate and distress pattern observed in CC8 Phase II Overlay test along with the discrepancy between predicted and observed pavement life suggests conservatism of the FAARFIELD failure model.

- HWD test data was used to evaluate joint stiffness. Good agreement was found between measured and predicted transverse joint stiffness.

8.2 RECOMMENDATIONS

- It is recommended to further investigate the potential of localized crack density, neutral axis position, and dissipated energy as indicators of pavement performance and traffic induced damage.

- It is recommended to consider the LTE as an alternative in the development of pavement failure criteria for future experiments at the NAPTF.

- It is recommended to evaluate the feasibility and develop a methodology to integrate CC4 and CC8 data analysis.

- It is recommended to revisit the findings of this report after examining the condition/damage in the underlay and HMA interlayer during the post-traffic investigation.

9. REFERENCES

1. Khazanovich, L., Improved Concrete Overlay Design Parameters for Airfield Pavements, Report DOT/FAA-01-G-002-2, Innovative Pavement Research Foundation for the Aviation Administration, Washington, D.C., 2001.

2. Stoffels, S., D. Morian, A. Ioannides, S. Wu, S. Sadasivam, L. Yeh and H. Yin, Improved Overlay Design Parameters for Concrete Airfield Pavements, Baseline Experiment Final Report, Innovative Pavement Research Foundation (IPRF) Project FAA-01-G-002-04-02, 2008.

3. Stoffels, S., D. Morian, A. Ioannides, L. Yeh, J. Reiter and S. Wu, Improved Overlay Design Parameters for Concrete Airfield Pavements—SCI Validation Study Research Report, Innovative Pavement Research Foundation (IPRF) Project FAA-01-G-002-06-03, 2010.

4. Harrington, D. and G. Fick. Guide to Concrete Overlays: Sustainable Solutions for Resurfacing and Rehabilitating Existing Pavements, Third Edition. Ames, IA: National Concrete Pavement Technology Center, Iowa State University, 2014.

5. Rollings, R.S., Design of Overlays for Rigid Airport Pavements, Report No. DOT/FAA/PM87/19, Federal Aviation Administration, Washington, D.C., 1988.

6. Federal Aviation Administration. AC 150/5320-6F, Airport Pavement Design and Evaluation, 2016.

7. ASTM. “Standard Test Method for Airport Pavement Condition Index Surveys,” D5340-12, American Standard for Test and Materials, West Conshohocken, PA, 2012.

8. Lin, Y. Modified Mechanistic-Empirical Airfield Unbonded Concrete Overlay Traffic Prediction Model. Dissertation. The Pennsylvania State University, State College, PA, 2011.

9. Yin, H. Simulation of Flexible Pavement Response to FWD Loads: A Mechanistic Approach, International Journal of Pavement Research and Technology, 2012, 5(4), 257-266.

10. Byrum C.R. et al. . Joint Load Transfer in Concrete Airfield Pavements: Final Report. Innovative Pavement Research Foundation (IPRF) Project FAA-01-G-002-05-2, 2011.

11. Ioannides, A. M. and M. I. Hammons. (1996). Westergaard-Type Solution for Edge Load Transfer Problem. Transportation Research Record: Journal of the Transportation
Research Board, 1996. 1525: 28-34.

12. Crovetti, J.A. Design and Evaluation of Jointed Concrete Pavement Systems Incorporating Open-Graded Permeable Bases. Dissertation. University of Illinois at Urbana-Champaign, Champaign, IL, 1994..